GEL SPUN PAN AND PAN/CNT BASED CARBON FIBERS:

FROM VISCOELASTIC SOLUTION TO ELASTIC FIBER

A Dissertation
Presented to
The Academic Faculty

By
Bradley Allen Newcomb

In Partial Fulfillment
Of the requirements for the Degree
Doctor of Philosophy in the
School of Materials Science and Engineering

Georgia Institute of Technology
May 2015

GEL SPUN PAN AND PAN/CNT BASED CARBON FIBERS:

FROM VISCOELASTIC SOLUTION TO ELASTIC FIBER

Dr. Satish Kumar, *Advisor*
School of Materials Science and
Engineering
Georgia Institute of Technology

Dr. Anselm Griffin
School of Materials Science and
Engineering
Georgia Institute of Technology

Dr. Donggang Yao
School of Materials Science and
Engineering
Georgia Institute of Technology

Dr. Meisha Shofner
School of Materials Science and
Engineering
Georgia Institute of Technology

Dr. Chuck Zhang
School of Industrial Systems and
Engineering
Georgia Institute of Technology

ACKNOWLEDGEMENTS

TABLE OF CONTENTS

LIST OF TABLES

LIST OF FIGURES

Chapter 1
INTRODUCTION

1.1 Overview

Carbon fiber composites are employed for use in high performance applications. In order to further the technology in high performance carbon fiber composites, a main focal point of research has been on the production of high performance carbon fibers. As a result, the two main carbon fibers in production today are polyacrylonitrile (PAN) based carbon fibers and pitch based carbon fibers. Other carbon fiber precursors include cellulose, lignin, and polyethylene (PE), which have been proposed as low cost carbon fiber alternatives despite their inferior mechanical properties as compared to commercially available PAN and pitch based carbon fibers. PAN based carbon fibers are desirable due to their high mechanical properties, tensile strength (3-7 GPa) and tensile modulus (230-588 GPa), as well as good thermal ($\sim 10^1$ W/m-K) and electrical ($\sim 10^4$ – 10^5 S/m) conductivity. Pitch based carbon fibers are attractive due their high tensile modulus (up to 960 GPa), thermal conductivity (up to $\sim 10^3$ W/m-K), and electrical conductivity (up to $\sim 10^6$ S/m), despite their lower tensile (< 3.5 GPa) and longitudinal compressive strength (< 1 GPa).

1.2 PAN based Carbon Fiber

Production of PAN based carbon fiber (Figure 1.1[1]) requires the polymerization of PAN or PAN copolymer followed by fiber spinning and drawing before stabilization in air (200-300 ℃) and carbonization in an inert environment (1000-1700 ℃). An additional graphitization step can also be performed, which is conducted by heat-treating the fiber up to 3000 ℃ in an inert environment. During the heat treatment process, the

carbon content within the PAN precursor fiber will increase from 68% in homopolymer PAN to > 90% in the final carbon fiber. As the heat treatment temperature is increased the carbon fiber modulus increases and the carbon content will continue to increase, with standard modulus fibers like Toray T300 containing 93 wt% carbon, intermediate modulus fibers like Toray T800 containing 96 wt% carbon, and high modulus fibers like Toray M60J containing > 99 wt% carbon.

1.2.1 Polymerization of polyacrylonitrile

Solution, emulsion, and suspension polymerization techniques have successfully been applied to the polymerization of PAN homopolymer and copolymers[2]. Solution polymerization is typically used for the production for acrylic fibers due to its ability to be directly spun into fiber after the completion of the polymerization. However, the unreacted monomer must be removed from the solution prior to fiber spinning and solvents such as dimethylacetamide (DMAc) and dimethylformamide (DMF) have high-chain-transfer constants, which do not yield polymer of sufficient molecular weight for textile end use[3]. Typical textile grade acrylic fibers make use of PAN copolymers with a number average molecular weight of 40,000 – 70,000 g/mol, weight average molecular weight of 90,000 – 170,000 g/mol, and a polydisperity between 1.5 and 3.0. Despite the problem of achieving a high molecular weight through solution polymerization, this setback has been overcome through the incorporation of an aliphatic hydrocarbon into the solvent. Addition of the aliphatic carbon results in the polymerization initially proceeding as an emulsion polymerization, followed by further addition of solvent and completing the reaction as a solution polymerization.

```
┌─────────────────────────────────────┐
│         Polymerization              │
└─────────────────────────────────────┘
                  ▼
┌─────────────────────────────────────┐
│         PAN Precursor               │
│ (Typical Fiber Diameter 10 – 15 μm) │
└─────────────────────────────────────┘
                  ▼
┌─────────────────────────────────────┐
│        Stabilization in Air         │
│      Temperature 200 – 300 ºC       │
│       Stabilization Under Tension   │
│       Stabilization Time ~2 hours   │
└─────────────────────────────────────┘
                  ▼
┌─────────────────────────────────────────────┐
│ Carbonization in an Inert Environment (N₂)   │
│          Temperature 1000 – 1700 ºC          │
│           Carbonization Under Tension        │
│          Carbonization Time ~30 minutes      │
│              Typical Properties:             │
│             Modulus: 200 – 300 GPa           │
│          Compressive Strength: ~3 GPa        │
│              Shear Modulus: ~15 GPa          │
│                Diameter: 5-7 μm              │
│       Electrical Conductivity: 50,000 S/m    │
│       Thermal Conductivity: < 10 W/m-K       │
└─────────────────────────────────────────────┘
                  ▼
┌─────────────────────────────────────────────┐
│     Graphitization in Inert Environment      │
│          Temperature 2500 – 3000 ºC          │
│              Typical Properties:             │
│             Modulus: 500 – 600 GPa           │
│           Compressive Strength: 1 GPa        │
│              Shear Modulus: ~10 GPa          │
│                Diameter: 5-7 μm              │
│      Electrical Conductivity: 100,000 S/m    │
│       Thermal Conductivity: < 15 W/m-K       │
└─────────────────────────────────────────────┘
```

Figure 1.1 Flow chart of PAN based carbon fiber production. (Adapted from ref. 1).

Emulsion polymerization provides the advantage of producing high molecular weight PAN homopolymers and copolymers by segregating radicals in monomer micelles without decreasing the polymerization rate. A water-soluble agent such as potassium

persulfate (oxidizer)/sodium bisulfite (reducing agent) initiates the polymerization, with the polymerization proceeding rapidly within the micelle. After the completion of the emulsion polymerization, the polymer must be separated from the aqueous phase prior to fiber manufacture.

The most widely used polymerization technique in the production of polyacrylonitrile is that of suspension polymerization, which uses persulphates, perchlorates, or hydrogen peroxide as a radical initiator. Just as in emulsion polymerization, a common redox system of potassium persulfate and sodium bisulfite is used[4]. Due to the insolubility of PAN in water, and the low monomer concentration, chain growth is limited in the aqueous phase. Following reaction termination, the aqueous stream of polymer particles is mixed with a chain stopper and subsequently filtered. The polymer cake is then washed, dried, and milled prior to dissolution in the preferred solvent.

Radical polymerization techniques have been shown to introduce molecular defects such as chain branching[5, 6], enamine formation[7], and β-ketonitrile defects[8] during the aqueous dispersion polymerization of PAN as shown in Figure 1.2[7]. Chain branching has been suggested to occur when the ratio of polymer to monomer is greater than one through a side chain by monomer addition[6]. Peebles et al. reported a second mechanism for chain branching where the branching occurs through the nitrile group[5], which can also occur as a result of radical transfer by disproportionation or other chain transfer mechanisms that involve abstraction of a hydrogen atom. If the terminal bond is a double bond, long chain branching can occur.
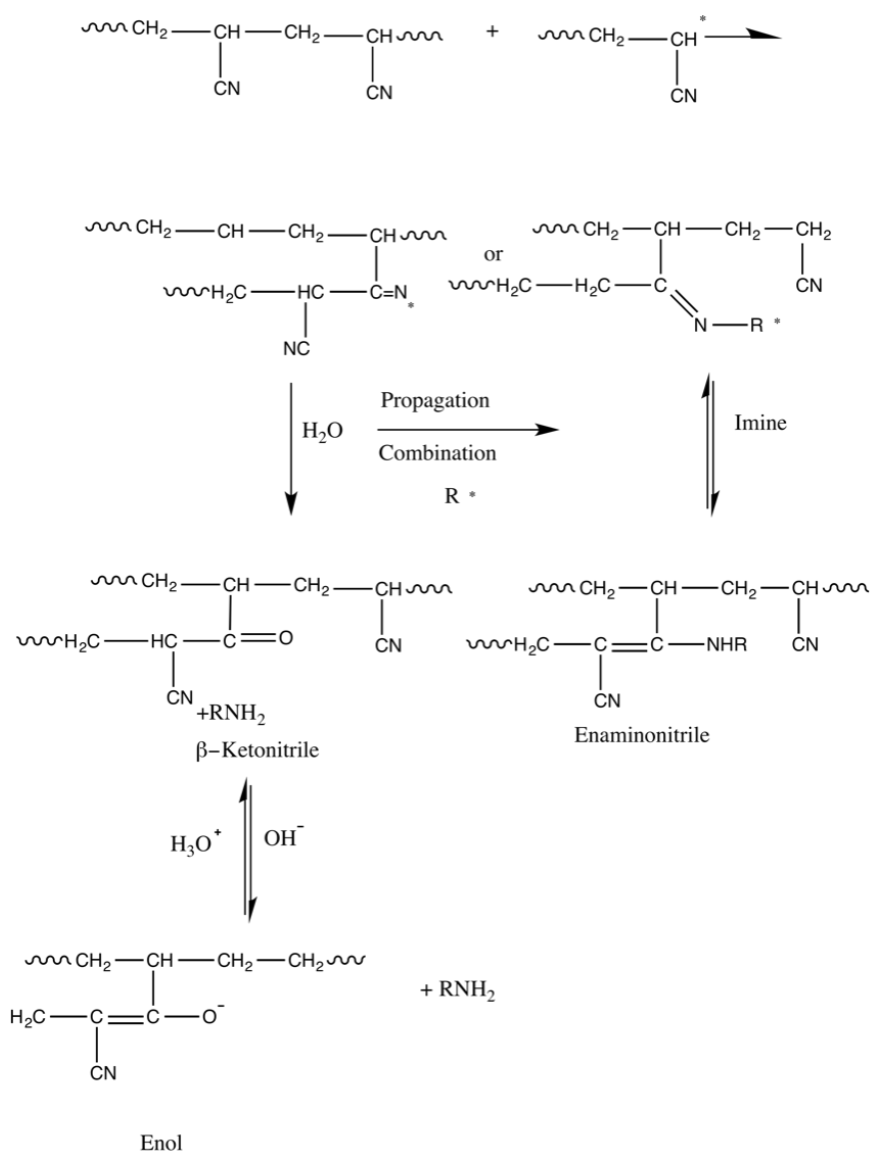
Figure 1.2. Structural defects generated in polyacrylonitrile through branching. (Adapted from ref. 7).

Polymerization of PAN for the production of carbon fiber typically contains one or more comonomers with molecular weight, typically higher than those used in textile grade acrylic fibers[9], of ~10^5 g/mol, polydisperity between 2 and 3, and minimum molecular defects during polymerization. Typical copolymers used are methyl acrylate (MA), methyl methacrylate (MMA), vinyl acetate (VA), methacrylic acid (MAA),

itaconic acid (IA), and acrylamide (AM). Comonomers are added to the polymerization to enhance the solubility of the polymer in the spinning solvent, modify the fiber morphology, while acidic comonomers lower the reaction initiation temperature and broaden the exothermic peak during fiber stabilization. Reduction of the reaction initiation temperature as compared to homopolymer PAN through acidic comonomer addition results in reduced cyclization time and carbon yield. For this reason, the optimum comonomer content is between 0.5-2.0 mol%[9, 10].

Enhanced solubility of high molecular weight PAN through the addition of comonomers is advantageous for suspension polymerization techniques due to the required washing, drying, milling, and dissolution steps required after the completion of the polymerization prior to precursor fiber production. Dissolution of dried PAN homopolymer or copolymer in organic solvents is difficult due to the tendency of the powders to form lumps, which are difficult to dissolve[9]. Typical organic solvents for the production of PAN fiber include DMF, DMAc, dimethylsulfoxide (DMSO), ethylene carbonate, and propylene carbonate. Of these solvents, DMF is preferred due to its superior solubility of PAN as evidenced by the Hansen solubility parameters listed in Table 1.1. Complete dissolution of the PAN powder is required for the production of high quality PAN precursor fiber. As the molecular weight of the polymer is increased, dissolution of the powder becomes increasingly more difficult making the solvent selection and solution preparation methods more important.

Table 1.1. Homopolymer PAN and organic solvent solubility parameters[11].

Solvent/Polymer	δ_d	δ_p	δ_h	$\delta_t (MPa^{1/2})^a$	$|\delta_{pt} - \delta_{st}|^{2b}$
PAN	18.2	16.2	6.8	25.3	
DMF	17.4	13.7	11.3	24.8	0.25
DMAc	16.8	11.5	10.2	22.7	6.8
DMSO	18.4	16.4	10.2	26.6	1.7
Ethylene Carbonate	19.4	21.7	5.1	29.6	18.5
Propylene Carbonate	20.0	18.0	4.1	27.3	4.0

^{a} δ_t is the total solubility parameter $(MPa)^{1/2}$, which is defined as $\delta_t^2 = \delta_d^2 + \delta_p^2 + \delta_h^2$, where δ_d is the dispersive contribution, δ_p is the polar contribution, and δ_h is the hydrogen-bonding contribution.
^{b} $|\delta_p - \delta_s|^2$ is the absolute squared difference in the total solubility of the polymer (δ_{pt}) and the total solubility of the solvent (δ_{st}).

1.2.2 Fiber spinning of polyacrylonitrile

Acrylic fiber formation was first suggested by DuPont in 1941, and commercialized under the trade name Orlon in 1950[2]. PAN fiber has been spun using a variety of techniques including melt spinning, dry spinning, wet spinning, dry-jet wet spinning, and gel spinning. Each technique has its own positive and negative aspects. Melt spinning of PAN is advantageous due to the prospect of fiber production without the use of solvents. However, melt spinning of PAN is a highly specialized technique due to the inherent nature of the polymer, which will degrade before it effectively melts. The melting temperature of homopolymer PAN has been determined to be between 319-342 ºC at a heating rate of 40-160 ºC/min[12], and can be suppressed with the addition of water and/or suitable copolymers[13] allowing for melt spinning to successfully be completed.

Dry spinning requires a suitable solvent, which must have good stability with PAN at the solvent boiling point, low vapor pressure so that the solvent can evaporate in the spinning tower, and good dissolving properties for PAN. Due to these stringent requirements, suitable solvents are limited to those such as DMF[14] and DMAc. A second

type of solution spinning includes the use of a liquid medium in which the extruded polymer is coagulated into fiber. Solution spinning which involves the use of a liquid coagulation medium can be categorized into wet spinning, dry-jet wet spinning, and gel spinning. Wet spinning involves a submerged spinneret where the extruded polymer solution is immediately introduced into the coagulation bath. Dry-jet wet spinning, also known as air gap spinning, involves raising the spinneret ~1-2 cm above the coagulation bath so that the extruded polymer solution is subjected to an air environment before being introduced into the coagulation bath medium. Gel spinning is characterized by the use of a high molecular weight polymer dissolved in a solvent at low concentrations, ~2-15 wt%. During the extrusion of the spinning dope, the fiber takes on a gel state before phase separation occurs, therefore giving this technique the name of gel-spinning. PAN fiber has been produced from the gel-spinning technique from several different sources, using several different methods (Table 1.2)[9], and the final mechanical properties are much higher than those produced using other fiber spinning techniques mentioned above. Mechanical property values recorded in Table 1.2 are some of the highest values ever reported for PAN fibers. Due to the commercial nature of PAN fiber spinning, extensive information about the fiber processing is not always available. However, a series of work on ultrahigh molecular weight-polyacrylonitrile (UHMW-PAN)[15-18] has achieved a tensile modulus for PAN of 35 GPa[17], as well as tensile strengths in the range of 1.8-1.9 GPa for gel-spun UHMW-PAN ($M_v = 2.3 \times 10^6$) fibers[18].

Table 1.2. Mechanical properties of PAN fibers obtained from various gel-spinning processes. Reproduced from ref. 9.

Company	M_w or limiting viscosity η	Solvent for polymer	Polymer Concentration (%)	Cooling Bath	Gelation Temperature	Draw Conditions	Total Draw Ratio	Tenacity (cN/tex)	Initial Modulus (cN/tex)
Allied	1.63×10^5	DMSO	6	DMSO:water (50:50)	Room Temperature	4.07x 135-150 ℃ 2.11x 146-160 ℃	8.6	70	2200
Stamicarbon	1.3×10^6	DMF + ZnCl$_2$	5	CHCl$_2$	Room Temperature	Dry, 180 ℃	28	153	1860
Toyobo	1.4×10^6	DMF	7	Alcohol/dry ice	-40 ℃	135 ℃ and 150 ℃ on hot plate	> 12	Very High	Very High
Japan Exlan	1.35×10^6	5% NaSCN	5	15% NaSCN	5 ℃	2x water 20 ℃ 2x water 85 ℃ 2.5x boiling water 1.8x ethylene glycol 130℃ 1.6x ethylene glycol 160 ℃	28.8	164	2700
	2.28×10^6	50% NaSCN	5	15% NaSCN	5 ℃	2x water 20 ℃ 2x water 85 ℃ 2.5x boiling water 1.8x ethylene glycol 130℃ 1.6x ethylene glycol 160 ℃	28.8	222	-
Toray	$[\eta] = 3.2 - 5.5$	DMSO	5-20	55-60% DSMO	1-20 ℃	Hot water, preheated dry 190-240 ℃	12-15	100-130	1600-2000
Kuraray	1.55×10^6	50% NaSCN aq.	2.9	15% NaSCN aq. ~5% CH$_2$OH	10 ℃	2.5x NaSNC 20℃ 9x 200℃	22.5	196	2490

1.2.2.1 Effect of spinning parameters on cross-sectional shape in solution spun fibers

Early investigations reported in the open literature were primarily focused on the effects of spinning parameters on the fiber formation of wet-spun acrylic fibers by Knudsen[19] and Paul[20-23]. Understanding the diffusion mechanism and which spinning parameters effect the solvent non-solvent counter-diffusion during fiber formation is crucial to determining which conditions will yield the best PAN precursor fiber. As with most solution-spun fibers, the major contributors to the fiber formation are the coagulation bath composition, coagulation bath temperature, and overall spinning rate.

Circular fibers are believed to be crucial for the development of high strength carbon fibers due to the requisite post processing conditions used in oxidative stabilization and subsequent carbonization. In non-circular fibers, the oxygen diffusion during stabilization will not be evenly distributed across the cross-section of the fiber, leading to under-stabilized or over-stabilized regions within the fiber. Although circular fibers are able to alleviate part of this issue, a circular cross-section of small diameter is further desired. Figure 1.3 depicts an irregular, kidney bean, and circular cross-sectional shape. Despite the fact that both irregular and kidney bean shapes are believed to hinder the uniform diffusion during fiber stabilization and carbonization, similar effects can occur in circular cross-sectional shapes. Figure 1.3d is the SEM image of the commercial T-300 carbon fiber with a near circular shape after thinning by focused ion beam (FIB) milling. Despite its near circular shape, the fiber shows distinct contrast differences in the outer region of the fiber (skin) and the inner region (core). Characterization of this skin-core structure has also been observed in the PAN based Amoco T50 fiber by transmission electron microscopy (TEM) and the resulting diffraction patterns. By

plotting the orientation factor of the (002) crystal plane as a function of distance from the fiber center in Figure 1.4[24], it can be seen that the skin has a higher degree of orientation as compared to the core. The orientation measured in Figure 1.4 is the half width at half maximum (HWHM) of the azimuthal (002) peak where the HWHM is inversely related to the crystal orientation.
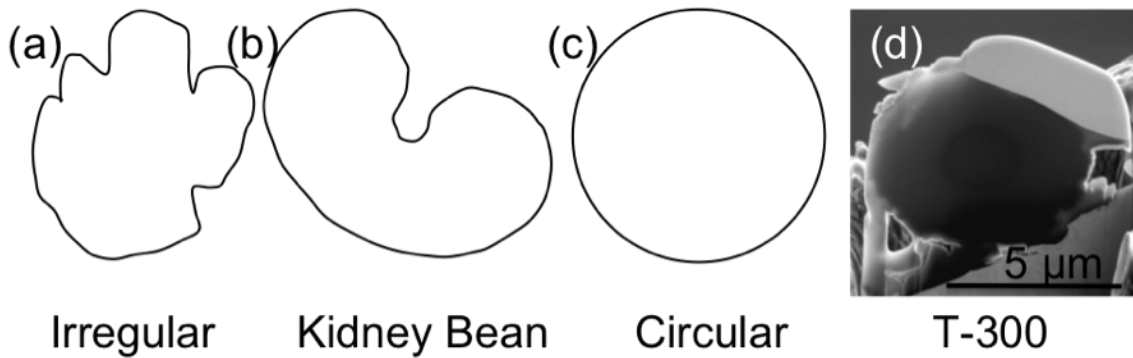
Figure 1.3. (a) Irregular, (b) kidney bean, and (c) circular cross-sectional shapes of PAN based fibers, which can arise through differences in fiber spinning parameters and will retain their shape in the resulting carbon fiber. (d) SEM image of T300 carbon fiber after FIB milling showing a distinct contrast difference, which relates to the skin and core morphologies present in the fiber. The white region on top of the T300 fiber in (d) is a protective platinum layer.
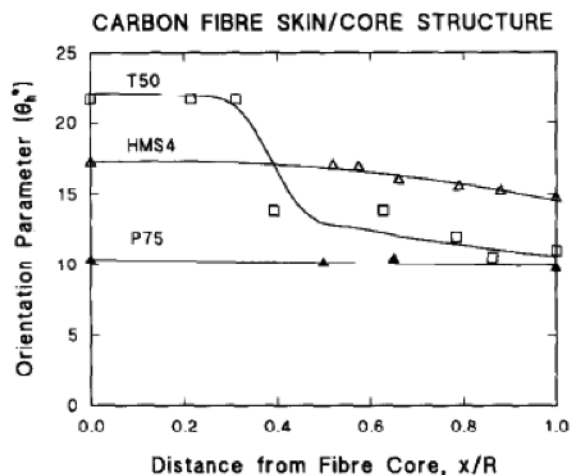
Figure 1.4. Orientation parameter (HWHM) of Amoco T50, Hercules HMS4, and Amoco P75 carbon fibers. The PAN based carbon fibers (T50 and HMS4) exhibit orientation differences between the skin and core. The pitch based P75 fiber does not show the same skin-core morphology. Ref. 24.

1.2.2.2 Coagulation bath composition

Fiber formation during solution spinning is caused by the diffusion of solvent out from the gel-fiber into the coagulation bath, which will consist of a mixture of polymer solvent and non-solvent. Coagulation of the fiber can also occur in a solvent-free bath[25, 26], whereas the opposite (non-solvent free bath) is not viable. Rates of diffusion of the polymer solvent into the coagulation bath will be dependent upon the ratio of solvent and non-solvent in the coagulation bath, the interaction between solvent and non-solvent, polymer/solvent interaction, polymer/non-solvent interaction, and other factors. Previous results indicate that as the amount of solvent in the coagulation bath is increased the cross-sectional shape moves from a kidney bean or oval shape towards a circular shape[27, 28].

The effects of the coagulation bath composition are shown in Figure 1.5, where a constant 60 ℃ coagulation bath was maintained while the solvent to non-solvent ratio

12

was adjusted. Using a 60 °C coagulation bath temperature, the cross-sectional shape in dry-jet wet-spun fibers coagulated in a 0:100 DMF:water bath take an irregular shape (Figure 1.5a) which moves to a kidney bean shape in a 22:78 DMF:water bath (Figure 1.5b). Finally, the cross-sectional shape takes on oval shape at a coagulation bath composition of 51:49 DMF:water (Figure 1.5c)[27]. Mechanical properties are not reported, despite the in depth characterization of the diffusion process during acrylic fiber formation.
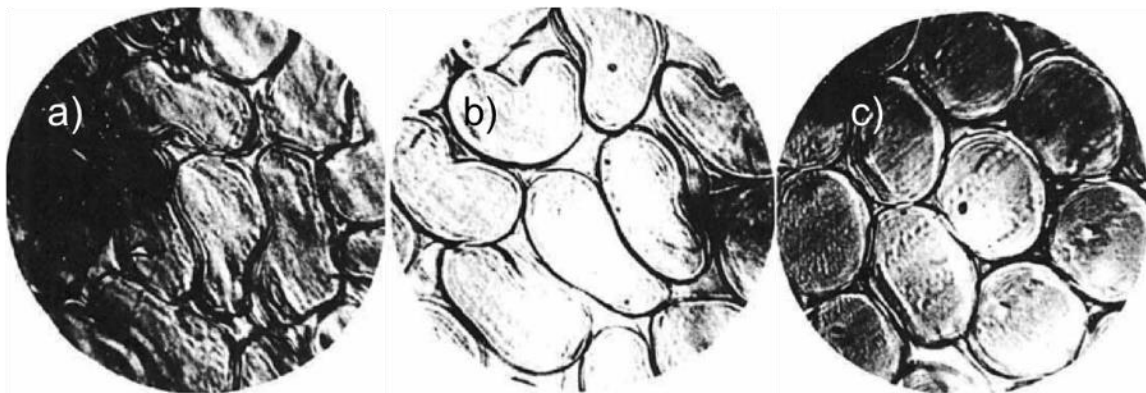
Figure 1.5. Effect of coagulation bath composition on cross-sectional shape of PAN fibers: (a) 100:0, (b) 78:22, and (c) 49:51 water:DMF[27]. As the presence of DMF in the coagulation bath is increased the cross-sectional shape changes from a bean to oval-like.

1.2.2.3 Coagulation bath temperature

During the extrusion process, the polymer solution undergoes a series of temperature profiles, which ultimately leads to the removal of the polymer solvent and solidification of the fiber. Controlling the coagulation bath temperature is essential when attempting to process continuous fiber with the same fiber cross-section across all filaments. Previous studies have shown that as the temperature of the coagulation bath is increased, the fiber cross-sectional shape moves towards a round shape[27, 29, 30]. With this improved cross-sectional shape comes the presence of macrovoids[19, 29] in the fiber cross-

section, which will be detrimental to the final carbon fiber properties. The presence of macrovoids in the fiber cross-section is attributed to the higher coagulation temperature, which increases the non-solvent diffusion into the fiber. Due to the faster diffusion of the non-solvent, it has been suggested that the internal adjustments within the fiber are given less time to occur ultimately resulting in the presence of larger voids[29]. Figure 1.6 depicts the effect of an increased coagulation bath temperature while using a coagulation bath composition of water:DMF (60:40) ranging from 10-40 °C[29]. As the temperature is increased the cross-sectional shape moves toward a circular shape while the increased presence of macrovoids becomes more pronounced.
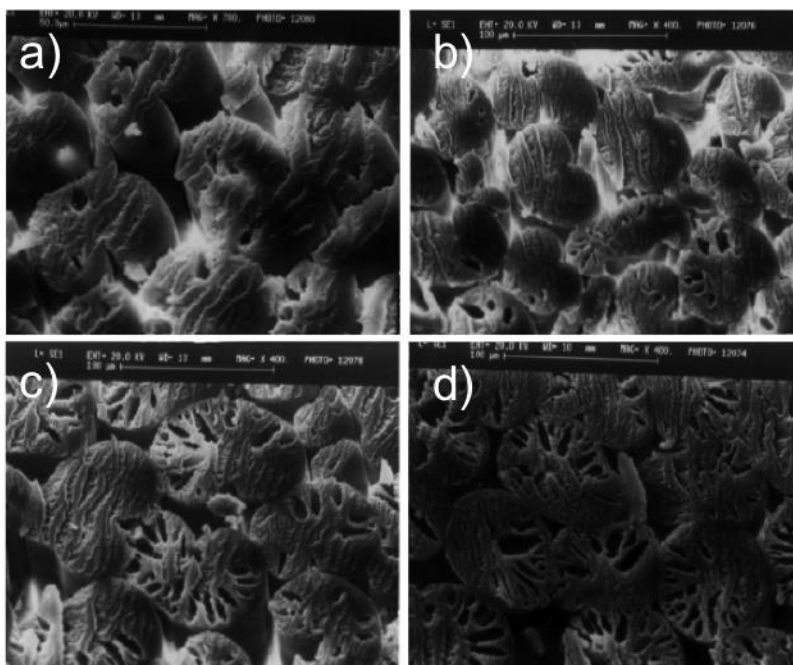
Figure 1.6. Effect of coagulation bath temperature on cross-sectional shape of PAN-co-MAA (98.7/1.3) fibers coagulated in a water:DMF (60:40) bath at: (a) 10, (b) 20, (c) 30, and (d) 40°C. As the coagulation bath temperature is increased, the number of voids increases and the cross-sectional shape changes from bean-shaped to oval-like[29].

1.2.2.4 Spinning rate

Polymer extrusion rate and fiber collection rate influence the overall diffusion rates during fiber formation in the coagulation bath. As the polymer extrusion rate is increased, the shear rate increases resulting in higher polymer orientation particularly on the surface of the fiber. The increased polymer orientation will decrease the solvent diffusion rate out of the fiber, as well as the non-solvent diffusion into the fiber. Increased rates of fiber collection will increase the rate of solvent non-solvent diffusion, due to the higher radial stress caused by the jet-stretch, but will not alter the ratio of solvent to non-solvent diffusion[27]. Increased jet-stretch has been reported to increase tenacity, crystallinity, crystal size, molecular orientation, and result in a more circular cross-sectional shape in the wet-spun as-spun fiber[28, 31]. However, changes in cross-sectional shape are not expected due to a sustained solvent to non-solvent diffusion ratio as the jet-stretch is changed[27], only faster or slower coagulation is expected. Observed changes in the cross-sectional shape due to increased jet-stretch could likely be created by the collapsing of voids within the fiber due to the higher stresses within the fiber caused by the jet-stretch.

1.2.2.5 Other influencing factors

Coagulation bath temperature, composition, and overall spinning rate, play major roles in the fiber formation of solution-spun fibers, but other parameters can also determine the final cross-sectional shape. These parameters alter the diffusion coefficients of the solvent and non-solvent during fiber formation and include the choice of solvent[26] and air gap height[27]. It was reported that during the use of dimethylsulfoxide (DMSO) as a solvent, the fiber cross-sectional shape is more circular in nature as

compared to a similarly processed fiber using DMF as a solvent. Differences were suggested to be caused by the increased solution viscosity of the PAN/DMSO solution as compared to the PAN/DMF solution[26]. Although no viscosity data is presented, the increased viscosity for the PAN/DMSO solution should not necessarily be true. Table 1.1 includes the Hildebrand solubility parameters for homopolymer PAN accompanied by common solvents and non-solvents used in the production of PAN fibers[11], which suggests that DMF is a superior solvent of PAN as compared to DMSO. Due to the increased solubility of PAN in DMF, the polymer chains will have an increased radius of gyration ultimately increasing the solution viscosity[32].

Based upon the solubility parameters in Table 1.1, DMF will act as the best solvent for homopolymer PAN due to the increased interaction potentials. Based upon the calculated interaction parameters between PAN and DMF, the diffusion rate of DMF out of the coagulating fiber will be the slowest if all other interactions are ignored. However, the interaction between the solvent and non-solvent must be considered when determining whether DMF or DMSO will diffuse out of the coagulating fiber faster. In order to offset these slower diffusion rates of DMF as compared to DMSO, other fiber spinning parameters will need to be adjusted to form a circular fiber.

During the fiber formation process in dry-jet wet spinning, the polymer solution first passes through an air gap before entering the coagulation bath, after leaving the spinneret. While the solution is passing through the air gap, solvent is able to evaporate leaving a reduced amount of solvent required to diffuse out during coagulation in the bath. It has been reported that the air gap height does not greatly influence the diffusion coefficients and therefore the cross-sectional shape during dry-jet wet spinning.[27].

1.3.1 Stress transfer from polymer matrix to CNT

PAN/CNT composite fibers have successfully been processed using dry-jet wet spinning[33-35], gel-spinning[25, 36], and electrospinning[37, 38]. Improvements in the tensile properties of the PAN/CNT fibers as compared to the similarly processed PAN fibers provide evidence of stress transfer from the polymer matrix to the CNT[25, 34]. Stress transfer occurs due to shear stresses, which arise at the matrix-fiber interface due to differences in axial elastic displacements while the composite is under strain. Previous methods of calculating the interfacial shear strength of polymer/CNT composites have included molecular dynamics simulations[39-41], fiber pull-out tests[42-47], fragmentation tests[48], and recently Raman spectroscopy[49]. These results report a wide range of polymer-carbon nanotube interfacial shear strengths ranging from 2-500 MPa over a variety of polymers and nanomaterials. The nanomaterial inclusions range from SWNTs, double walled carbon nanotubes (DWNTs), MWNTs, and vapor grown carbon nanofibers (VGCNFs). Frankland et al.[39] studied the effect of covalent bonding from the CNT to the crystalline PE matrix through molecular dynamics and found a nearly 40-fold improvement in the interfacial shear strength due to covalent bonding to the PE matrix (2.8 MPa to 110 MPa). Ozkan et al.[44] found a decrease in interfacial shear strength from 106 to 66 MPa using the fiber pull-out method in as-received and heat treated VGCNFs. Differences in shear strength were attributed to the high temperature heat treatment used to graphitize the surface of the VGCNF, concluding that the heat treatment reduced the surface roughness, and therefore the interfacial shear strength.

The fiber pull-out method requires a significant amount of sample preparation, while typically not determining the interfacial shear strength in the final polymer

nanocomposite as well as yielding a large scatter in the data due to large variations in the pull-out length during testing. Given that the interfacial shear strength between the polymer and the CNT must be monitored in the final material, other methods need to be developed which are able to determine the interfacial shear strength.

1.3.1.1 Raman spectroscopy of CNTs and polymer/CNT nanocomposites

Stress-induced Raman band shifts have been monitored in macroscopic fibers, particularly carbon fiber[24, 50] and poly(paraphenylene terephthalamide) (PPTA) fibers[51], as well as in SWNTs[52-54] and SWNT bundles[55]. SWNTs exhibit Raman active modes, which present themselves in four particular regions of the Raman spectra; the radial breathing mode (RBM), disorder induced mode (*D*), graphitic mode (*G*), and the overtone of the *D* mode (*G'*) (Figure 1.7a). The RBM is characteristic of SWNTs and DWNTs, and is due to the in phase vibration of the carbon atoms in the radial direction (Figure 1.7b) and is observed from ~100 – 400 cm^{-1} in the Raman spectra. The *D*-mode is typically referred to as the disorder induced mode, due to the requirement that the photon momentum is broken by disorder within the crystal lattice, presenting at ~1300 cm^{-1}. The *G*-mode is referred to as the graphitic mode due to its presence in 2D graphite and occurs at ~1582 cm^{-1} (Figure 1.7c). The *G'*-mode is the overtone of the *D*-mode, and is found at ~2600 cm^{-1}. Given that the *D*, *G*, and *G'* modes are related to the C-C bonds in the SWNT, any downshift in their vibrational frequency will be related to a weakening of the C-C bond, and therefore a stretching of the C-C bond[56]. For this reason, the *D*, *G*, and *G'* modes can be used to monitor stress-induced shifts within the Raman spectra of SWNTs.
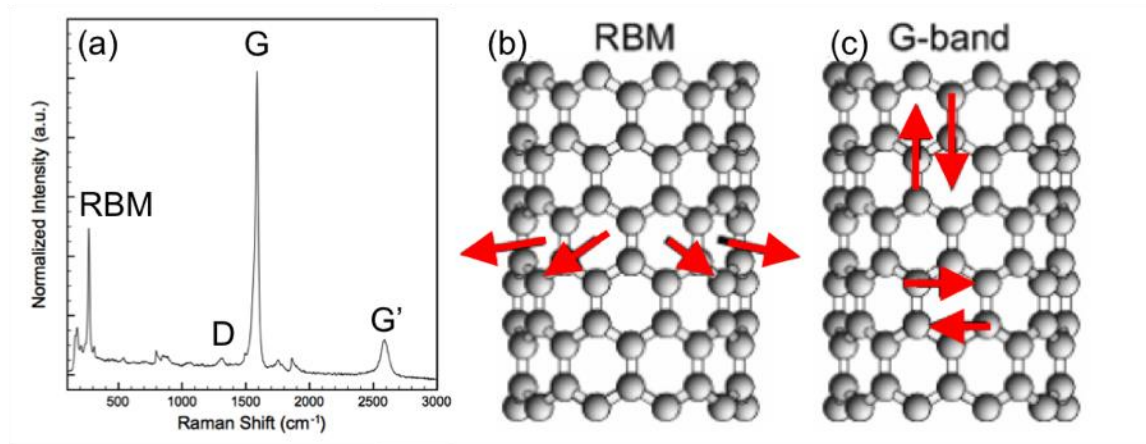
Figure 1.7. (a) Raman spectra of few-walled carbon nanotubes (FWNTs) exhibiting RBM, D, G, and G' modes. (b) In phase vibration of carbon atoms in SWNTs resulting in the RBM. (c) G-band in CNTs with vibrations along the nanotube axis (G+) and in the circumferential direction (G-).

Individual CNTs were strained using an AFM and the stress induced Raman band shifts were monitored through micro-Raman spectroscopy to determine the effect of strain on the structure of the CNT[52, 53]. Raman band shifts in the *G* band of up to -157 cm^{-1} have been monitored in ultra-long SWNTs with strains of 13.7% also measured[54]. Earlier studies reported *G'* Raman band shift of   -40 cm^{-1} for a SWNT at a strain of 1.65 %[52]. It was experimentally observed that the relative shift of the *D*, *G*, and *G'* bands was chirality dependent, and that metallic SWNTs experienced a shift in the radial breathing mode (RBM) intensity[53].

CNT fibers have been successfully produced since 2000[57], and have since been produced using a variety of methods[58]. CNT fibers were spun from vertically aligned CNT arrays and studied through strain-induced Raman spectroscopy. It was observed that the CNT fibers exhibited three distinct stages during deformation by monitoring the stress-induced Raman band shifts during tensile deformation. The first stage provided

evidence for elastic deformation, which was followed by plastic deformation before the fiber breaks in the third stage[59].

Polymer/CNT composites have been subjected to strain and simultaneously investigated with Raman spectroscopy, providing intriguing results. By monitoring the *G* or *G'* Raman band shift, the interaction between polymer and CNT can be monitored. Up shifts in the *G'* Raman band have also been shown by subjecting the epoxy/SWNT by cooling[60], causing compression on the SWNTs.

1.3.1.2 Effect of CNT type

The first studies of stress induced Raman band shift in carbon nanotube composites examined single walled carbon nanotubes (SWNTs) and multi-walled carbon nanotubes (MWNTs)[60-62]. It was concluded that epoxy/MWNT composites exhibited increased load transfer efficiency in compression rather than in tension by monitoring the *G'* Raman band shift. Due to the ability of MWNTs to sheath during tensile loading, it was determined that only the outer layer of the MWNT successfully transfers load. Tensile and compressive modulus was increased by 20 and 24%, respectively, which supports the conclusion that MWNTs were aiding the load transfer efficiency in compression greater than in tension with the addition of 5 wt% MWNT[61]. *G'* Raman band shift studies of epoxy/SWNT composites showed nearly no shift in compression (attributed to buckling, bending, and twisting) and only a slight shift in tension (due to slippage of SWNT ropes)[62].

Similar work was performed on epoxy/CNT composites in an attempt to determine the level of epoxy/CNT interaction by monitoring the *G'* Raman band shift rate. The SWNT/epoxy samples were determined to have a *G'* Raman band shift rate of -

1.3 cm^{-1}/% strain for SWNTs prepared using the arc-discharge method (Figure 1.8a), and

-15 cm^{-1}/% strain for SWNTs prepared using a pulsed laser vaporization process (Figure

1.8b). MWNTs used in the study were determined to have a *G'* Raman band shift rate of

-5.3 cm^{-1}/% strain (Figure 1.8c) and were prepared using the arc-discharge method.

Through the results of the study, no clear distinction could be made as to whether or not

SWNTs or MWNTs provides a better interaction to the epoxy matrix[63].
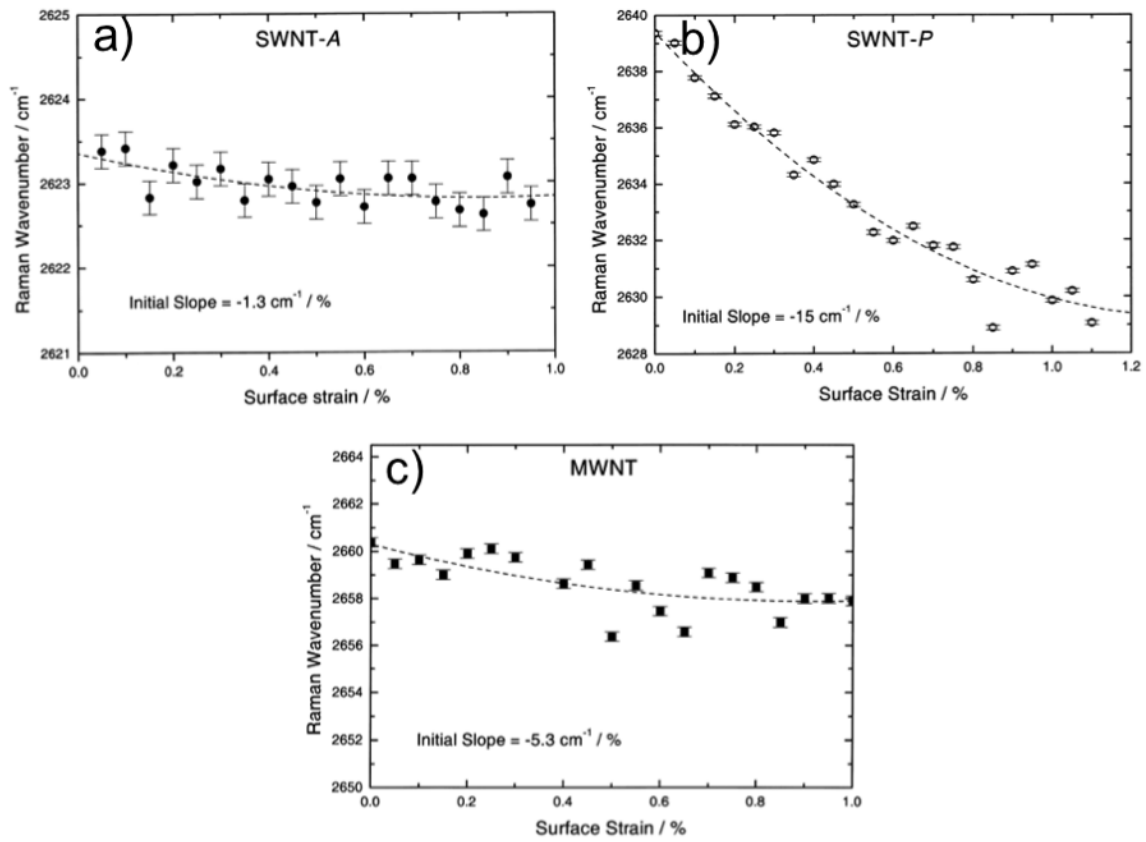
Figure 1.8. Effect of CNT type on the strain induced G' Raman band shift in CNT/epoxy composites using (a) Arc-discharge SWNT-A, (b) pulsed laser vaporization SWNT-P, and (c) arc-discharge MWNT[63]. No clear distinction can be made as to whether SWNT or MWNT provides the greatest interaction within the epoxy.

Based upon mechanical property data in PAN nanocomposites, a 5 wt% addition of MWNTs provided the greatest improvement in tensile strength, attributed to their long length, while a 5 wt% addition of SWNTs increased the tensile modulus most significantly[34]. By utilizing different aspect ratio carbon nanotubes[64], dispersed using various methods, the interaction between polymer and CNT can be maximized. As the aspect ratio of the CNT increased, the efficiency in the stress transfer from polymer to CNT is enhanced, which suggests that fully de-bundled CNTs with long lengths are a requirement for an optimized polymer/CNT composite.

1.3.1.3 Effect of CNT orientation

Due to the orientation dependence of Raman scattering on carbon nanotubes, it is also expected that this would influence the Raman band shift of CNTs during Raman strain measurements[65, 66]. A recent investigation was undertaken[67] to examine the effect of polarization, CNT orientation, and strain direction on the Raman band shift rate of PVA/SWNT composites. PVA/SWNT films exhibited a reduced Raman band shift rate as compared to a PVA/SWNT electrospun fiber, which was attributed to the enhanced orientation of the CNT within the electrospun fiber.

1.3.1.4 CNT fiber and polymer/CNT nanocomposites

With the advancement of CNT fibers[68] and the increased understanding upon the critical factors[69-72] which contribute to their potential high mechanical properties, Raman spectroscopy can provide further insight into the CNT-CNT interaction which occur as the CNT fiber is strained to failure[55, 59]. Similar interaction occurs in CNT bundles within polymer/CNT composites, and can be used to provide further understanding of the interfacial interaction between polymer and CNT, by successfully eliminating the CNT-

CNT interaction due to bundling. CNT pullout tests have been performed using AFM to examine the polyethylene-butene/CNT interface[42], and determined that the force required to separate the CNT from the polymer matrix is greater than that which would cause the polymer matrix to yield. This observation is evidence that the polyethylene-butene in the vicinity of the CNT behaves differently than the bulk polyethylene-butene of the matrix

1.4 Thesis objectives

In this study, the processing, structure, and properties of gel spun PAN and PAN/CNT based carbon fibers will be investigated with the following objectives:

- Study the effective mixing of high molecular weight PAN-co-MAA (M_v = 513,000 g/mol) in DMF to produce PAN-co-MAA/DMF solutions for the production of PAN precursor fibers and carbon fibers.

- Understand the processing, structure, and properties of PAN and PAN/CNT precursor fibers using a variety of fiber spinning parameters in order to alter the fiber cross-sectional shape and its effect on carbon fiber structure and properties.

- Develop a method using Raman spectroscopy to characterize the interfacial interaction in PAN/CNT fibers, which can be used to calculate the interfacial shear strength in polymer/CNT composites.

- Observe the structure of PAN and PAN/CNT based carbon fibers using high resolution transmission electron microscopy and measure the thermal and electrical conductivity of single filament gel spun PAN and PAN/CNT based carbon fibers.

Chapter 2
POLYACRYLONITRILE SOLUTION HOMOGENEITY STUDY BY DYNAMIC SHEAR RHEOLOGY AND THE EFFECT ON THE CARBON FIBER TENSILE STRENGTH

2.1 Introduction

High-performance (high tensile strength and high tensile modulus) fibers such as Spectra™, Dyneema™, Kevlar™, Zylon™, and carbon fibers, etc., are now available in the consumer market. The key parameters to obtain such high tensile properties in these fibers are: (1) to maximize molecular alignment along the fiber axis for high tensile modulus and (2) to minimize defect structures (voids, chain ends, entanglement, and surface defect) for high tensile strength[73]. The progress for achieving high tensile modulus appears to be more advanced than that for the high tensile strength. For example, carbon fiber with a tensile modulus of 965 GPa (>90% of theoretical modulus) is available[74]. Nonetheless, the tensile strength of this fiber is only about 3 GPa that is <5% of theoretical strength of a carbon-carbon bond. High strength carbon fibers (up to about 7 GPa) are also available but it is still far less than the theoretical values and their tensile moduli are in the range of 300 – 325 GPa[74]. It is interesting to note that the common processing step to manufacture all these high-performance fibers is to prepare spinning dope (polymer solution) either by dissolving polymer in solvent or by synthesizing polymer in solution state. Structural inhomogeneity in the resulting fiber may be significantly affected by, but not limited to, the presence of inhomogeneity in polymer solution. Therefore, it is very critical to ensure molecular level homogeneity.

Polyacrylonitrile (PAN) polymer is the predominant precursor for high-performance carbon fiber and PAN precursor fiber is also processed from polymer solution. Polymerization methods of PAN include suspension, solution, or emulsion polymerization, although the latter

has seldom been practiced commercially[2]. A variant of suspension polymerization known as aqueous dispersion polymerization is commonly used for the commercial production of acrylic fibers[2]. Advantage of aqueous dispersion polymerization is fast propagation[75], while it requires post-processing steps such as washing, drying, milling, and dissolving the PAN polymer powder in solvent to obtain solution for fiber spinning. Solution polymerization method does not require the extra-steps of preparing spinning dope, but it is difficult to obtain high molecular weight PAN polymer[9]. For dissolution of the PAN polymer from suspension or emulsion polymerization methods, solvents such as DMF, dimethylacetamide (DMAc), dimethylsulfoxide (DMSO), sodium thiocyanate (NaSCN) aqueous solvent, or ethylene carbonate are used. It is often observed that the polymer powder forms partially soluble gels in the solution, and such a gel structure is known to form from the strong polar interaction between PAN molecules, the presence of very high molecular weight polymer, or the thermally induced cross-linking[2]. Electron microscopy studies of poly(acrylonitrile-co-vinyl acetate) showed that microgels on the order of 50 nm in diameter are present in the solution[76]. This inhomogeneity can lead to the inhomogeneous stabilization and carbonization that are detrimental to obtain high strength carbon fiber. Therefore, homogeneously dissolved PAN polymer is an important step to manufacture high quality precursor and carbon fiber.

Homogeneity of polymer solution or melts has been characterized by dynamic shear rheology, and it can be correlated to the slope of log G' (storage modulus) vs log G'' (loss modulus) plot[77-80]. This behavior has been exploited to study polymer blends[81-84], block copolymers[85, 86], block copolymer nanocomposites[87], polymer nanocomposites[88-92], and thermotropic liquid crystals[93]. In the case of homo-polymers it has been shown that as the level of heterogeneity within the polymer solution or melt increases, the slope of the log G' vs log G''

plot reduces from its theoretical value of 2 for a linear, flexible, homogeneous, entangled, mono-disperse solution or melt[94, 95]. Likewise, this plot can be useful in the determination of the compatibility of polymer blends, order-disorder transition temperature of block copolymers and block copolymer nano-composites, heterogeneity of polymer nano-composite solutions and melts, and differentiation of the isotropic or nematic state in thermo-tropic liquid crystalline polymers. However, the correlation of solution homogeneity to the properties of the resulting bulk materials has not been demonstrated. In this study, the homogeneity of PAN solutions is monitored by dynamic shear rheology and its effect on the resulting carbon fiber tensile strength is discussed.

2.2 Experimental

2.2.1 Materials and processing

PAN-co-MAA polymer with a viscosity average molecular weight of 513,000 g/mol was obtained from Japan Exlan Co. (Osaka, Japan) and the solutions were prepared with a solid concentration range of 9.75 – 10.5 g/dL in distilled DMF (Sigma Aldrich). The detailed procedures of solution preparation are listed in Table 2.1. It is noted that two different mixing apparatus were used within two different reactors (Parr reactor and glass reactor) for dissolving polymer as shown in Figure 2.1. PAN-co-MAA/DMF solutions were prepared in a Class 1000 cleanroom to minimize the presence of external particles during solution preparation. Samples A-F were prepared in a Parr reactor, while samples G-J were prepared in a glass reactor. The maximum stirring speed used during high temperature solution mixing was 150 rpm and 700 rpm for the glass and Parr reactors, respectively. It is also noted from Table 2.1 that some of the trials used a slurry preparation step below room temperature before dissolving polymer at high temperature (> 70 °C). This step was taken to prevent aggregation of polymer powder due to partial dissolution at room temperature.

27

The control solution was prepared in the Parr reactor at a concentration of 10 g/dL. Slurry preparation was performed at 4 °C for 60 min, followed by an increase in solution temperature to 70 °C at a heating rate of 0.5 °C/min. After the solution was heated to 70 °C, the solution was stirred continuously at 500 rpm for 72 hours. All stirring times for the control solution are listed as a function of stirring after the solution temperature was raised to 70 °C.

The prepared solutions were collected and transferred to a multi-filament fiber spinning system (Hills, Inc.) and spun into fibers in a 100 filament tow. The as-spun fibers were collected with a spin draw ratio of 3 using a methanol gelation bath maintained at -50 °C. During the unwinding of the as-spun fibers, Samples G-J were washed through chilled methanol to reduce fiber friction during fiber drawing that was observed in Samples A-E. Sample F was used to prepare two precursor fibers: (Sample F_1) before washing through chilled methanol during fiber unwinding and prior to fiber drawing and (Sample F_2) after washing through chilled methanol during fiber unwinding and prior to fiber drawing. All fibers where then drawn in three stages with a post-spin draw ratio of 8.2. PAN precursor fiber properties are listed in Table 2.1. Subsequently, 100 filament precursor fiber tows were continuously stabilized in the temperature range of 180 – 250 °C, and carbonized up to 1450 °C. Fiber spinning and carbonization was also performed in a Class 1000 cleanroom.

2.2.2 Characterization

PAN-co-MAA/DMF solutions were studied using dynamic frequency sweep parallel plate rheology (ARES, TA Instruments, Co.) using 50 mm plates and a gap of 1 mm at room temperature. Upon sample loading, a thin layer of silicone oil was applied at the exposed surface of solution to prevent solvent evaporation and gelation by moisture absorption. Single filament PAN precursor and carbon fiber tensile testing was performed on a FAVIMAT+ (Measured

Solutions, Inc.) at 1 inch gauge length as described elsewhere[96]. The linear density of each filament tested was measured by inline vibroscope. Scanning electron microscopy (SEM) was performed on a Hitachi S3400 at an operating voltage of 10 keV.
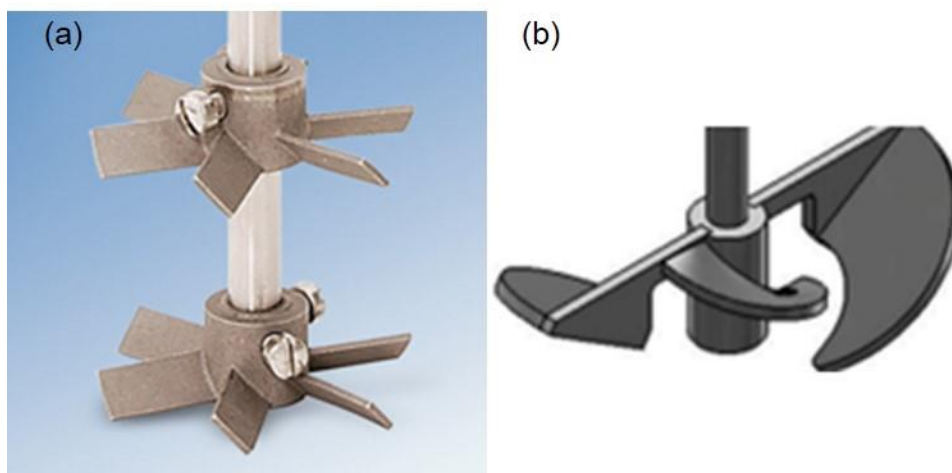
Figure 2.1 Schematic of (a) Parr and (b) glass reactors mixing tools used for PAN-co-MAA/DMF solution preparation.

Table 2.1 PAN-co-MAA/DMF solution preparation conditions and the resulting precursor fiber properties.

Sample	Reactor type	Conc. (g/dL)	Slurry preparation		High temperature solution preparation			Precursor fiber properties		
			Temp. (°C)	Time (min)	Temperature (°C)	Time (h)	rpm	Diameter (μm)	Tensile strength (GPa)	Tensile modulus (GPa)
Control	Parr	10	4	60	70	72	500	No fiber manufactured		
A	Parr	10	4	60	90	2	700	11.7 ± 0.7	0.9 ± 0.1	19.9 ± 0.7
B	Parr	10.5	20	10	90	2	700	11.8 ± 0.7	0.9 ± 0.1	18.6 ± 0.6
C	Parr	10.5	20	10	90	2	700	7.3 ± 0.5	0.8 ± 0.1	17.8 ± 1.4
D	Parr	10.5	20	10	90	2	700	9.3 ± 0.5	1.0 ± 0.1	21.2 ± 0.7
E	Parr	10.5	4	60	90	2	700	10.8 ± 0.7	0.9 ± 0.1	18.7 ± 0.9
F	Parr	10	4	60	90	2	500	11.0 ± 0.8	1.0 ± 0.1	19.7 ± 0.8
G	Glass	10.5	4	60	90	2	150	11.5 ± 0.8	1.0 ± 0.1	19.8 ± 0.8
H	Glass	10	4	300	20 / 45 / 90	17 / 25 / 2	150	11.0 ± 0.8	1.0 ± 0.1	20.2 ± 1.1
I	Glass	10	4	300	20 / 45 / 90	17 / 25 / 2	150	11.0 ± 0.7	1.0 ± 0.1	19.7 ± 0.8
J	Glass	10	4	60	75	2	150	10.9 ± 0.8	1.0 ± 0.1	19.8 ± 0.8

2.3 Results and discussion

2.3.1 Effect of stirring time on the dynamic shear rheology of the PAN-co-MAA/DMF solution

A control PAN-co-MAA/DMF solution was prepared to investigate the effect of dissolution time on the rheological properties of the solution (Table 2.1). The control solution was prepared in two steps: (1) slurry preparation at 4 °C for 60 min and (2) dissolution of polymer by heating to 70 °C at a heating rate of 0.5 °C/min and continuous stirring up to 72 h. Solutions were collected at periodic intervals during continuous stirring at 70 °C.

Figure 2.2a shows the plots of log η^* (complex viscosity) vs log ω (angular frequency). It is noted in Figure 2.2a that the complex viscosity at low shear rate (i.e., at the angular frequency of 0.1 rad/s) decreased with increasing stirring time. The zero-shear viscosity of polymer solutions or melts is strongly dependent on the molecular weight of polymer. Therefore, dilute solution viscometry was conducted by diluting the collected solutions at different stirring times (0, 24, 48, and 72 h) to the solution concentration of 0.5 g/dL. The inherent viscosity (η_{inh}) decreased up to 48 h of stirring and remained constant up to 72 h of stirring(Figure 2.2b), suggesting that a decrease in molecular weight occurred through the high shear dissolution process over an extended stirring time. The complex viscosity at low shear rate is also of interest to investigate because the plateau region (approaching zero-shear) is not well defined for the solutions collected at shorter stirring times. This may be due to the formation of polymer clusters by strong polar inter-molecular interaction. With increasing shear rate, this association breaks up and the continuous decrease in viscosity is observed. In contrast, the solution stirred for 72 h exhibits a well-defined plateau region that can be readily observed in Figure 2.2a. The modified Casson's equation can be used to calculate the critical stress or apparent yield stress of a

31

viscoelastic liquid, which is related to the distinct drop in viscosity and break-up stress of the molecular association or the structural breakdown. In the case of viscoelastic solutions, such as the PAN solutions presented here, the apparent yield stress or critical stress is determined where $G' > G''$, and is not the same as true yield stress as in the case of a viscoelastic solid or gel. Equation 2.1 below is the modified Casson equation[97] used for the determination of the critical stress:

$$\sqrt{G''} = \sqrt{\sigma_0} + \sqrt{\omega} \qquad\qquad (2.1)$$

where, G'' is the loss modulus, σ_0 is the apparent yield stress or critical stress, and ω is the angular frequency.

The modified Casson plot in Figure 2.2c shows that the solutions collected up to 24 h stirring time exhibit a critical stress, whereas those between 36 and 72 h did not possess a critical stress. Critical stress determined from the Casson plot suggests that after 36 h of continuous stirring at 70 °C, there is a clear distinction between the plateau and shear thinning regions of the complex viscosity. As a result of the clear division between the plateau and shear thinning regions, as indicated by absence of critical stress required to induce a structural breakdown of the solution, an enhanced solution homogeneity is apparent due to the lack of inter-molecular association between neighboring polymer molecules, minimizing the critical stress required for molecular dis-association, or structural breakdown.
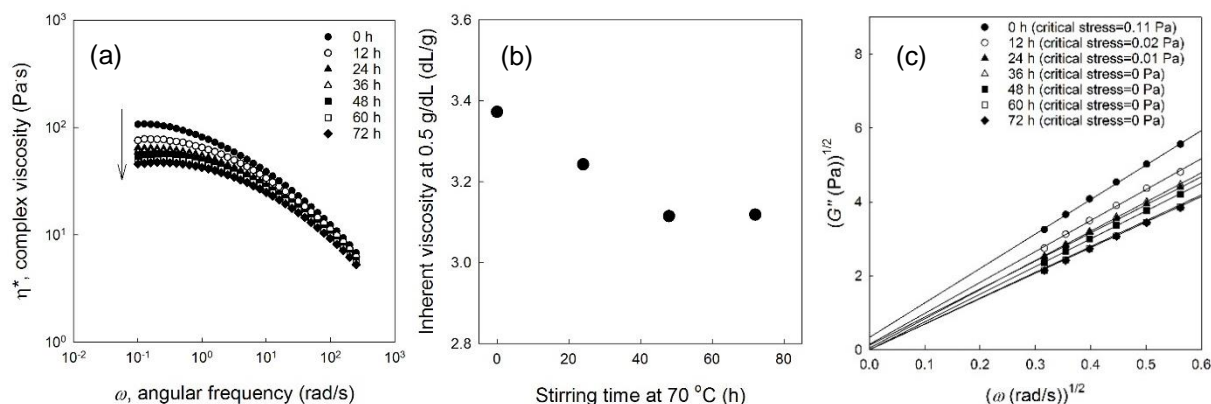
Figure 2.2 (a) Complex viscosity of the control solution as a function of angular frequency at different stirring times, (b) inherent viscosity of the control solution as a function of stirring time, and (c) the modified Casson plot to calculate the critical stress. The arrow shown in Figure 2.2a shows the direction of increasing stirring time.

Figure 2.3a shows the log G' vs log ω plots and Figure 2.3b gives the log G'' vs log ω plots for the collected solutions. The storage modulus at low ω decreased with increasing stirring time, leading to the increase in the slope of the log G' vs log ω plot at low ω towards a value of 2 as the stirring time is increased, indicating an increase in liquid-like behavior. The loss modulus also showed similar behavior with increasing stirring time at 70 °C, and the slope of the log G'' vs log ω plot at low ω increased towards a value of 1. Plots of loss factor (*tan δ*) vs log ω for the collected solutions in Figure 2.3c show a decrease in elastic nature as the stirring time is increased.
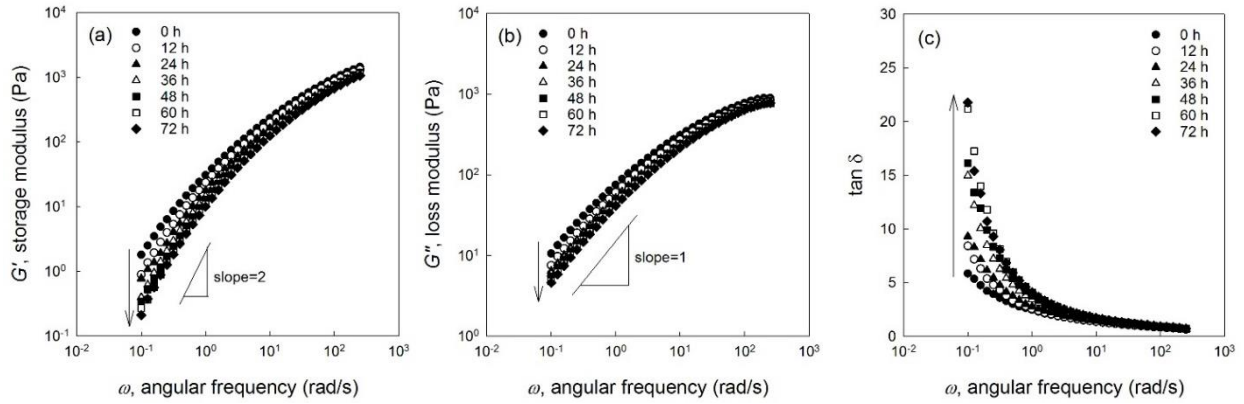
Figure 2.3 Dynamic shear rheological properties of the control solution as a function of angular frequency at different stirring time: (a) storage modulus, (b) loss modulus, and (c) tan δ. The arrows in Figure 2.3a, 2.3b, and 2.3c show the increasing trend of stirring time.

As discussed earlier, the dynamic shear rheological properties can also be used to assess the homogeneity of the polymer solution. Figure 2.4a is the so-called Han plot (log G' vs log G'') of the PAN-co-MAA/DMF solutions collected at stirring times of 0 and 72 h. For homogeneous solutions and melts, the slope of the log G' vs log G'' plot is theoretically equal to a value of 2 in the terminal region ($\omega\tau_d \ll 1$). As can be observed in Figure 2.4b, the slope of the log G' vs log G'' plot increases with increasing stirring time (from 1.45 to 1.72 after 0 h and 72 h of stirring, respectively), suggesting an increase in solution homogeneity by prolonged stirring time.

34
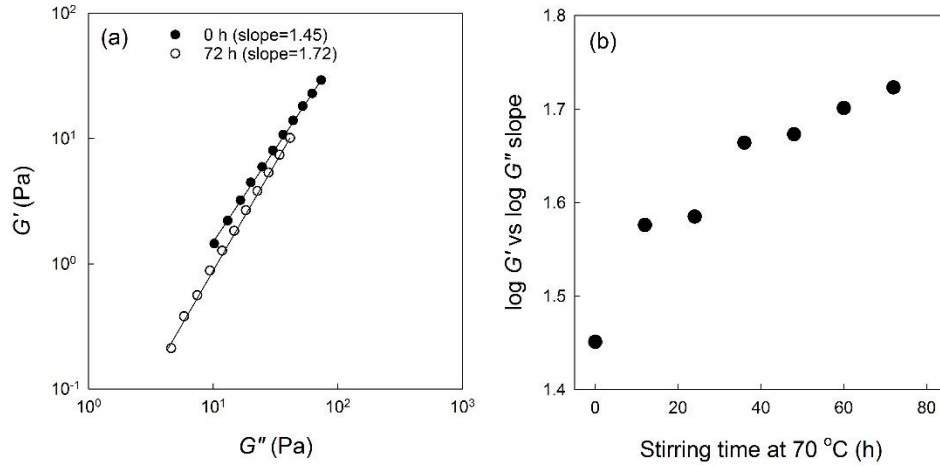
Figure 2.4 (a) log *G'* vs log *G"* of the PAN-co-MAA/DMF solution at the stirring time of 0 h and 72 h, and (b) the slope of log *G'* vs log *G"* plots of the PAN-co-MAA/DMF solutions as a function of stirring time. The slope was determined at the terminal region ($\omega\tau_d \ll 1$). The angular frequency range for the slope determination was from 0.1 to 1 rad/s.

In order to understand the interaction between polymer molecules in the solution, it is important to investigate the relaxation time of the polymer molecules in the solution. For example, the molecules with strong inter-molecular interaction will lead to a longer relaxation time. On the other hand, well dissolved polymer molecules with minimal inter-molecular interaction will exhibit a shorter relaxation time. Therefore, increase solution homogeneity is indicated by a shorter polymer relaxation time as a result of the enhanced penetration of the solvent molecules between polymer chains, which allow for increased chain mobility and the resulting reduction in polymer disentanglement time. Figure 2.5 contains the plot the first relaxation time (τ_l) of the control solution as a function of stirring time obtained by the relaxation spectrum defined below

$$G' = \sum_i^n \frac{\omega^2 \tau_i^2 g_i}{1+\omega^2 \tau_i^2} \tag{2.2}$$

$$G'' = \sum_i^n \frac{\omega \tau_i g_i}{1+\omega^2 \tau_i^2} \tag{2.3}$$

where g_i is relaxation strength and τ_i is the relaxation time. The reptation model predicts that the relaxation spectrum is dominated by a single relaxation time for a nearly mono-disperse melt, $\tau_1 = \tau_d$, where τ_d is the disentanglement time of a polymer molecules. Curve fitting of the linear relaxation spectrums for G' and G'' were performed simultaneously using the parallel plate rheology data and an iterative process to determine τ_i and g_i for each solution, with i = 3. Due to the dominance of the single (longest) relaxation mode (time), only the first order relaxation time ($\tau_1 = \tau_d$) is presented in Figure 2.5. As can be seen in Figure 2.5, τ_1 continues to decrease as the stirring time at 70 ºC is increased. Continued decrease of the PAN disentanglement time can be attributed to either the improved solution homogeneity as observed in Figure 2.4b, or due to a reduction in the polymer molecular weight (M_w) by the extended stirring time. The inherent viscosity results confirm the reduction in molecular weight due to the extended stirring time, while the reduction in disentanglement time as a function of stirring time is due to the combined effect of improved solution homogeneity and the reduction in molecular weight.
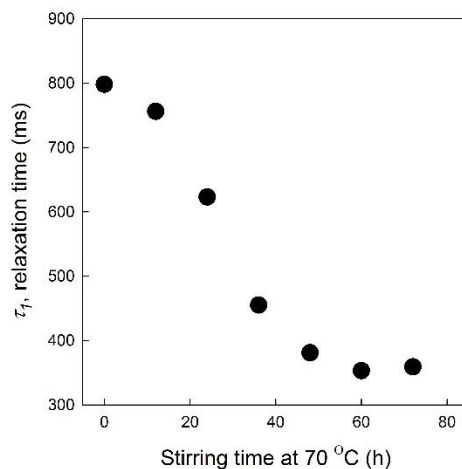
Figure 2.5 τ1 as a function of stirring time at 70 °C.

2.3.2 Dynamic shear rheological properties of various PAN-co-MAA/DMF solutions

Based upon the results discussed above, PAN-co-MAA/DMF solutions were prepared to process PAN-co-MAA precursor and carbon fibers. As listed in Table 2.1, two different dissolution apparatus were used to prepare solutions and here we group the rheological properties of the solutions according to the preparation apparatus. To begin with, the complex viscosity of the solutions prepared using the Parr and glass reactors are plotted in Figure 2.6a and 2.6b, respectively. Critical stress of the PAN-co-MAA/DMF solutions were determined using the modified Casson plot for solutions prepared in the Parr (Figure 2.6c) and glass (Figure 2.6d) reactors using Equation 2.1. Presence of a critical stress in all PAN-co-MAA/DMF solutions suggests that molecular association in the solution persists, with non-zero critical stresses required to induce the distinct drop in solution viscosity (plateau region transition to shear thinning region), despite the rigorous solution preparation conditions pursued in Samples A - J. On average, PAN-co-MAA/DMF solutions prepared in the Parr reactor exhibit a lower critical stress as compared to those prepared in the glass reactor. It should be noted that the dissolution time above 70 °C for all the trials used for fiber spinning is 2 h to minimize the molecular weight reduction that was observed from the prolonged stirring time in the control trial at that temperature (Table 2.1).
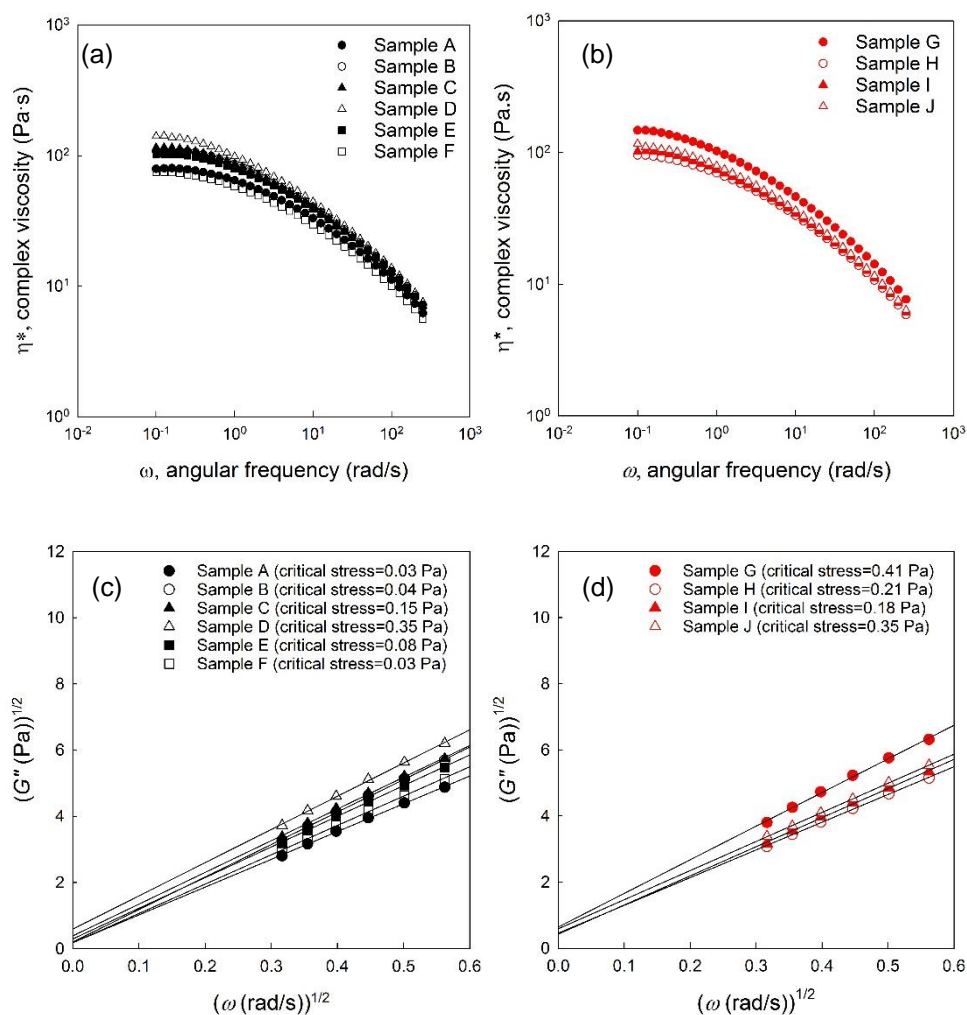
Figure 2.6 Complex viscosity as a function of angular frequency for solutions prepared using the (a) Parr and (b) glass reactors. Modified Casson plots for calculation of the polymer solution critical stress of the solutions prepared using the (c) Parr and (d) glass reactors.

Dynamic shear rheological properties of the PAN-co-MAA/DMF solutions prepared using the Parr reactor are shown in Figure 2.7. Plots of log G' vs log ω (Figure 2.7a) and log G'' vs log ω (Figure 2.7b) can be used to investigate the liquid-like behavior of the PAN-co-MAA/DMF solutions. Sample A exhibits greater liquid-like behavior as compared to other samples prepared using the Parr reactor, as monitored through the slope of the log G' vs log ω (1.414) and log G'' vs log ω (0.887) plots. In contrast, Sample D exhibits the lowest slope of the

log G' vs log ω (1.183) and log G'' vs log ω (0.691) plots. Table 2.2 contains the rheological analysis of the PAN-co-MAA/DMF solutions prepared in both the Parr and glass reactors. The *tan δ* vs log ω behavior of the six PAN-co-MAA/DMF solutions prepared in the Parr reactor is provided in Figure 2.7c. The magnitude of *tan δ* at ω=0.1 rad/s was used to compare the liquid-like nature of the solutions, and ranges from 5.230 (Sample D) to 9.873 (Sample A). Comparison of the *tan δ* values at ω=0.1 rad/s is used in order to quantitatively compare the elastic nature of the solutions. The choice of ω=0.1 rad/s was used in order to observe larger differences in the magnitude of the *tan δ* plot as compared to higher ω values where differences in *tan δ* are on a smaller scale.
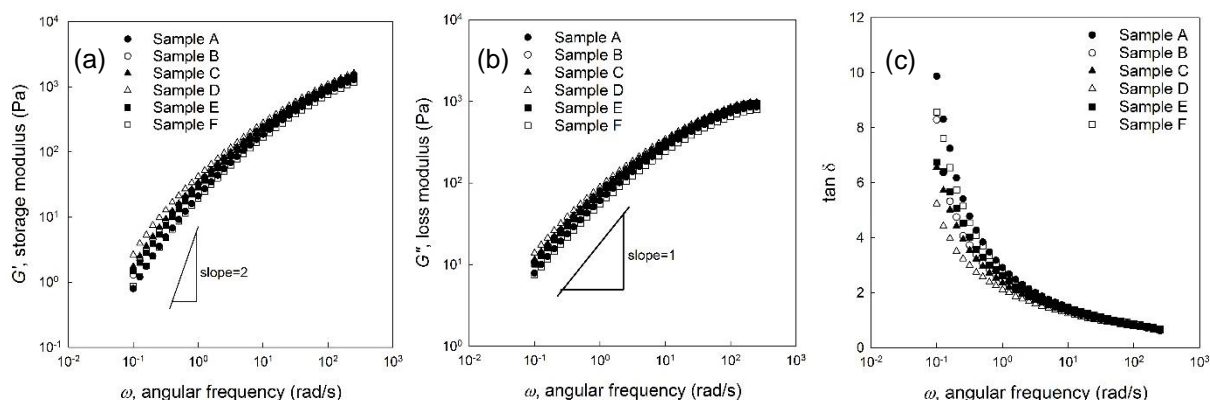
Figure 2.7 Dynamic shear rheological properties of the PAN-co-MAA/DMF solutions prepared in the Parr reactor as a function of angular frequency: (a) storage modulus, (b) loss modulus, and (c) tan δ.

Table 2.2 Rheological parameters of Samples A-J as determined from parallel plate rheology.

	Reactor type	Critical Stress (Pa)	log G' vs log ω slope[#]	log G'' vs log ω slope[#]	log G' vs log G'' slope[#]	*tan δ* at 0.1 rad/s
A	Parr	0.03	1.414	0.887	1.596	9.873
B	Parr	0.04	1.365	0.868	1.576	8.290
C	Parr	0.15	1.284	0.840	1.530	6.549
D	Parr	0.35	1.183	0.691	1.471	5.230
E	Parr	0.08	1.298	0.861	1.508	6.763
F	Parr	0.03	1.352	0.873	1.552	7.655
G	Glass	0.41	1.171	0.807	1.452	5.206
H	Glass	0.21	1.253	0.833	1.505	6.591
I	Glass	0.18	1.200	0.823	1.460	5.408
J	Glass	0.35	1.207	0.801	1.492	6.005

[#]The angular frequency range for the slope determination was from 0.1 to 1 rad/s.

The dynamic shear rheological properties of the PAN-co-MAA/DMF solutions prepared using the glass reactor are shown in Figure 2.8. Sample H exhibits greater liquid-like behavior as compared to other samples prepared using the glass reactor, as monitored through the slope of the log G' vs log ω (1.253) and log G'' vs log ω (0.833) plots. In contrast, Samples G and J exhibit the lowest slope of the log G' vs log ω (1.171) and log G'' vs log ω (0.801) plots, respectively. Figure 2.8c contains the plot of the *tan δ* vs log ω behavior of the PAN-co-MAA/DMF solutions prepared in the glass reactor. The magnitude of *tan δ* at ω=0.1 rad/s also represents the liquid-like nature of the solutions, and ranges from 5.206 (Sample G) to 6.591 (Sample H).
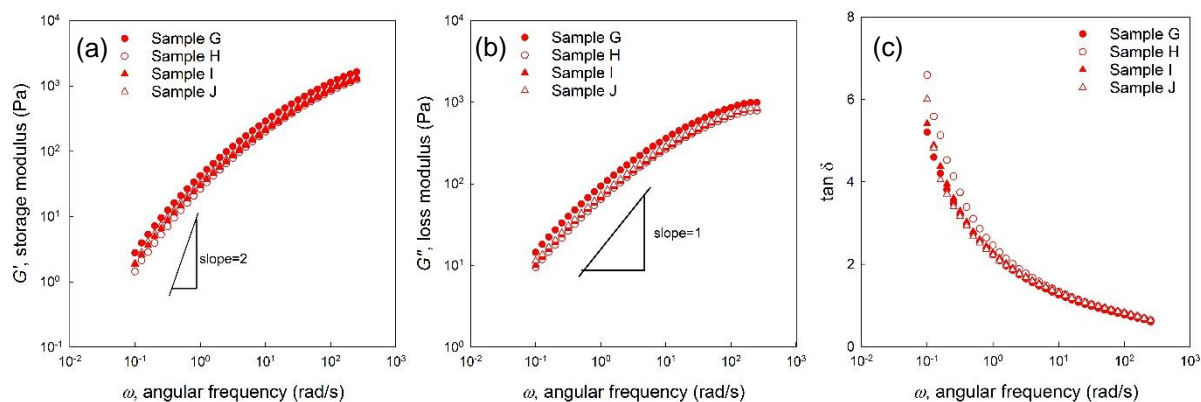
Figure 2.8 Dynamic shear rheological properties of the PAN-co-MAA/DMF solutions prepared in the glass reactor as a function of angular frequency: (a) storage modulus, (b) loss modulus, and (c) tan δ.

Figure 2.9a and 2.9b provide the plots of the log G' vs log G'' behavior for the PAN-co-MAA/DMF solutions prepared using the Parr and glass reactors, respectively. The lowest slope in the terminal region of solutions prepared using the Parr reactor is determined to be from Sample D (1.471) while the highest slope is from Sample A (1.596). Of the solutions prepared in the glass reactor, Sample G exhibits the lowest slope (1.452) and Sample H (1.505) has the highest slope of the log G' vs log G'' plot. From the slope (see Table 2.2) of the log G' vs log ω, log G'' vs log ω, and log G' vs log G'' plot, it can therefore be concluded that Sample A is the most homogeneous PAN-co-MAA/DMF solution while Sample D is the least homogeneous solution prepared in the Parr reactor. Similarly, Samples H and G are the most and least homogeneous solutions prepared using the glass reactor as determined from the slope of the log G' vs log G'' plot, respectively.

The plot in Figure 2.9c provides the magnitude of loss factor (*tan δ*) at ω=0.1 rad/s as a function of the slope of the log G' vs log G'' plot. Overlap of the rheological behavior of the PAN-co-MAA/DMF solutions in Figure 2.9c confirms that the dynamic shear rheological

behavior is independent of the reactor used to prepare the polymer solutions. This suggests that both reactors can be used for the dissolution of the PAN-co-MAA polymer in DMF at equal levels of molecular disassociation. However, distinctly different solution preparation methods are required to obtain similar viscoelastic behavior of the polymer solutions prepared in different reactor vessels (and mixing elements), as indicated by the solution preparation procedures used in Samples E and H (Table 2.1). Samples E (Parr) and H (Glass) both exhibit a similar *tan δ* magnitude at ω=0.1 rad/s and slope of the log *G'* vs log *G''* plot (Table 2.2). Sample E was prepared using a 60 min slurry preparation at 4 °C followed by heating to 90 °C and continuous stirring for 2 h. Sample H was prepared using a 300 min slurry preparation at 4 °C followed by stirring at 20 °C for 17 h. The solution temperature was then raised to 45 °C for 25 h followed by an increase in solution temperature to 90 °C for 2 h, all during continuous stirring. As a result, Sample E was prepared in ~10 hours as compared to the ~55 hours required for the final solution preparation of Sample H.
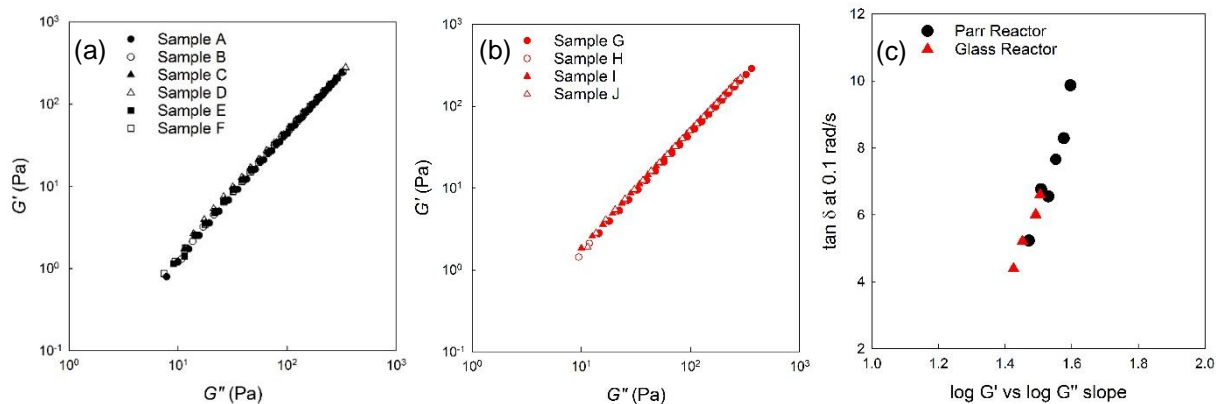
Figure 2.9 log G' vs log G'' plots of the PAN-co-MAA/DMF solutions prepared using the (a) Parr and (b) glass reactors.

2.3.3 Correlation of solution homogeneity and fiber surface damage on the resulting carbon fiber tensile strength

In Figure 2.10, as the slope of the log G' vs log G'' plot increases, the carbon fiber tensile strength is observed to increase. For similar slopes of the log G' vs log G'' plot, the fibers that underwent fiber washing yield higher tensile strength carbon fibers indicating that reducing the inter-filament fiber friction during fiber drawing plays an important role in the production of high tensile strength carbon fiber. Figure 2.10 provides evidence that understanding the PAN-co-MAA/DMF viscoelastic solution behavior is important to produce homogenous solutions (slope of log G' vs log G'' slope) for the manufacture of high tensile strength PAN based carbon fibers. Similarly, the plot also provides the justification for an additional fiber washing step prior to the first stage of fiber drawing as evidenced by the 28% improvement (4.3 ± 0.9 GPa (F_1, Figure 2.10) increased to 5.5 ± 1.1 GPa (F_2, Figure 2.10)) in average carbon fiber tensile strength in fibers prepared from Sample F due to the additional fiber washing step. The arrow in Figure 2.10 indicates the improvement in carbon fiber tensile strength when the as-spun fiber is washed through chilled methanol when the same PAN-co-MAA/DMF solution is used for precursor and carbon fiber production. Irrespective of the fiber washing conditions during fiber drawing, it can be clearly observed that the rheological behavior of the polymer solution has a distinct correlation with the ultimate carbon fiber properties.
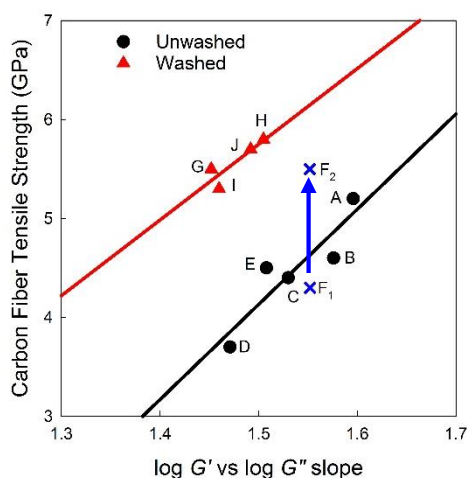
Figure 2.10 Correlation between PAN based carbon fiber tensile strength and log G' vs log ω slope. The best-fit lines in black use data from the solutions prepared in the Parr reactor that did not use a fiber washing step during fiber drawing (Sample A-E). The best-fit lines in red use data from the solutions prepared in the glass reactor that used an extra fiber washing step during fiber drawing (Sample G-J). Sample F consists of two data points (F1 and F2) , with the arrow indicating the increase in carbon fiber tensile strength that results from the additional fiber washing step in chilled methanol during the drawing of the precursor fiber.

The effect of fiber washing on the precursor fiber surface is observed in the SEM images provided in Figure 2.11. Figure 2.11a presents the SEM surface image of the precursor fiber manufactured from the Sample F solution after washing through chilled methanol prior to the first stage of fiber drawing. Smooth fiber surfaces are observed in the SEM image. In contrast, Figure 2.11b provides the SEM image of the precursor fiber surface after fiber drawing of the precursor fiber when the fiber is not washed through chilled methanol prior to the first stage of fiber drawing. Regions of fiber fibrillation can be observed in the SEM image where inter-filament fiber friction has damaged the fiber surface. Carbon fiber tensile strength improved 28% by adding in the additional fiber washing step prior to the first stage of precursor fiber drawing. Inter-filament fiber friction is presumed to be the result of the presence of additional solvent trapped in the fiber after the fiber spinning process. Residual solvent at the fiber surface will result in inter-filament fiber friction during fiber drawing as neighboring fibers attempt to slide

past each other during the drawing process. Minimizing the fiber friction during fiber drawing through the addition of a fiber washing step prior to fiber drawing results in an increase in carbon fiber tensile strength from 4.3 to 5.5 GPa.
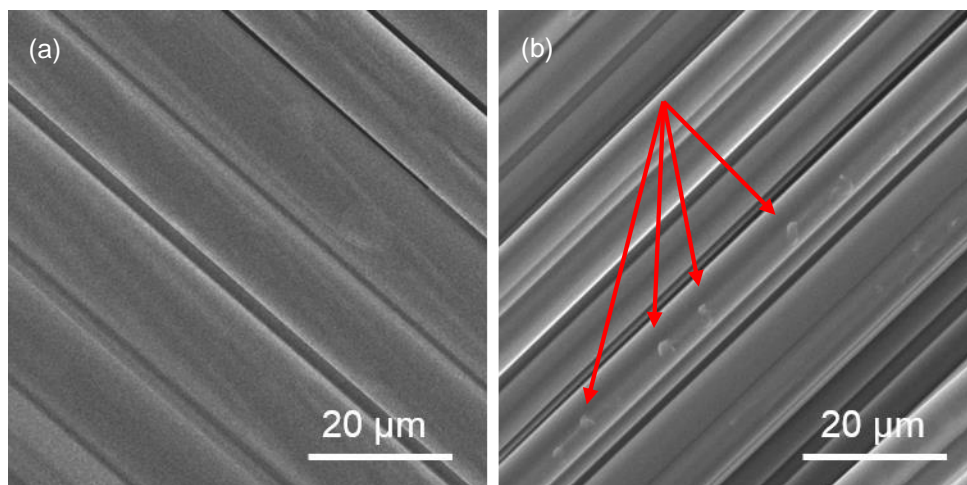
Figure 2.11 Precursor fiber SEM surface images of fibers manufactured from solution Sample F (a) with fiber washing through chilled methanol after unwinding prior to the first stage of fiber drawing and (b) no fiber washing prior to fiber drawing. The arrows in (b) point to the regions of fiber fibrillation due to fiber friction during fiber drawing.

2.4 Conclusions

PAN-co-MAA/DMF solutions were prepared under continuous stirring at 70 ºC and showed continually increased molecular level solution homogeneity as determined from the slope of the log G' vs log G'' plot, as well as increasing liquid-like behavior as evidenced by the increasing slopes of the log G' vs log ω and log G'' vs log ω plots as a function of stirring time. Continuous stirring of the PAN-co-MAA/DMF solution resulted in a decreasing critical stress as determined by the Casson plot, indicative of reduced molecular association. After 48 h of continuous stirring, the PAN-co-MAA/DMF solution did not exhibit a critical stress, indicative of a thixotropic solution that exhibits a plateau in the zero-shear viscosity. Solutions also exhibited decreasing elastic behavior and complex viscosity at low ω as the stirring time

increased. A decrease in molecular weight was confirmed through dilute solution viscometry measurements, where the η_{inh} also decreased by 8% after 72 hours of stirring at 70 °C.

PAN-co-MAA/DMF solutions were prepared using two different solution reactors, and were used for the production of PAN precursor fibers and PAN based carbon fibers. Based upon the rheological analysis of the PAN-co-MAA/DMF solutions and characterization of their resulting PAN-based carbon fibers, it is evident that carbon fiber tensile strength is dependent upon two observed factors: (1) molecular homogeneity as measured by the viscoelastic behavior of the polymer solution, monitored by the dynamic shear rheological properties, and (2) processing conditions during fiber drawing to reduce inter-filament fiber friction. Inter-filament fiber friction was observed through SEM imaging of the drawn precursor fibers. The addition of a fiber washing step by passing the fiber tow through chilled methanol prior to the first stage of fiber drawing resulted in a 28% improvement in carbon fiber tensile strength (4.3 GPa to 5.5 GPa). Improved molecular homogeneity in the PAN-co-MAA/DMF solution and the additional fiber washing step during fiber drawing resulted in carbon fibers with an average tensile strength of 5.8 GPa.

Chapter 3
PROCESSING, STRUCTURE, AND PROPERTIES OF GEL SPUN PAN AND PAN/CNT FIBERS AND GEL SPUN PAN BASED CARBON FIBERS

3.1 Introduction

Gel spinning has been used for the production of polyethylene[98], poly(vinyl alcohol)[99], and PAN[18] fibers, as well as their nanocomposite counterparts[25, 100-102]. Advantages associated with gel spinning include the ability to produce highly oriented fibers, yielding high strength and high modulus. Currently, PAN serves as the predominant precursor fiber for the production of high strength carbon fiber[74]. Commercially available high performance PAN based carbon fibers possess excellent tensile strength ($3 - 7$ GPa) and modulus ($230 - 588$ GPa), as well as good electrical ($\sim 10^4 - 10^5$ S/m) and thermal ($\sim 10^1$ W/m-K) conductivity[74], while having a circular or nearly circular cross-sectional shape. Recently, PAN and polyacrylonitrile/carbon nanotube PAN/CNT gel spun precursor fibers have been carbonized, resulting in fibers possessing high tensile strength and modulus, without a particular focus on the cross-sectional shape of the fiber[103-105].

Efforts have been made since the 1960's to understand the coagulation process of wet-spun acrylic fibers[20-22], and more recently for dry-jet wet-spun acrylic fibers[27, 29, 106]. Cross-sectional shapes of the acrylic fibers are diffusion controlled, and are dependent upon the fiber spinning parameters such as solution temperature at spinneret, coagulation bath temperature, coagulation bath composition, solvent, non-solvent, and polymer composition. Controlling the outward diffusion of the solvent and the inward diffusion of the non-solvent is not always a straightforward task due to the dynamic nature of the fiber formation process. Fiber formation is controlled by the thermodynamics of the system, while the kinetics dictate the rate at which the

final fiber reaches a state of equilibrium. Thermodynamically, fiber formation in wet spinning or dry-jet wet spinning occurs through the process of solidifying the polymer solution extrudate through the outward diffusion of the solvent and the inward diffusion of the non-solvent. However, the kinetics of fiber formation can alter the final fiber cross-section due to evidence that non-uniform circumferential stresses arise that can collapse the fiber structure, therefore altering the cross-sectional shape of the fiber. Such a collapse is the result of a dense, thin, outer skin forming at the surface of the extruded solution prior to complete solidification of the fiber. As the fiber continues to solidify, the thin outer skin of the fiber collapses, creating a non-circular cross-section. While the cross-sectional shape of the fiber is controlled by the kinetics of the fiber formation, the presence of internal voids within the fiber is controlled by the thermodynamics. For this reason, production of PAN fibers is typically performed at relatively low coagulation bath temperatures (~10-15 ℃) in the presence of a solvent/non-solvent coagulation bath[107]. Lower coagulation temperatures and the presence of solvent in the coagulation bath reduces the number of voids in the fiber[27].

Work by Paul[20] has focused on the diffusion processes associated with acrylic fiber formation where dimethylacetamide (DMAc) was used as the polymer solvent, a PAN copolymer consisting of polyacrylonitrile-co-vinyl acetate (PAN-co-VA) at a 92.3/7.7 composition by weight, and water was used as the non-solvent. To obtain diffusion coefficients of the solvent and non-solvent, gelled PAN-co-VA rods were prepared in DMAc at a polymer concentration of 26 wt% overnight in test tubes of a predetermined geometry. Rods were then coagulated in a water/DMAc bath of varying concentrations at either 30 or 50 ℃. By monitoring the refractive index of the coagulation medium as a function of time, the outward diffusion rate of the DMAc solvent and inward diffusion rate of the water non-solvent could be determined. It

was concluded that when the coagulation bath temperature is increased from 30 ℃ to 50 ℃, the outward diffusion rate of the solvent and inward diffusion rate of the non-solvent are increased. Likewise, as the DMAc content in the coagulation bath was increased, the outward diffusion rate of the solvent and the inward diffusion rate of the non-solvent decreased. Finally, it was also reported that the ratio of the DMAc/water diffusion rate increased as the DMAc content in the coagulation bath increased, confirming that the outward mass diffusion of DMAc is faster than the inward mass diffusion of water.

In a comparison of the coagulation during the wet-spinning and dry-jet wet-spinning of acrylic fibers, Baojun et al.[27] monitored the diffusion rates of the solvent dimethylformamide (DMF) and non-solvent (water) with coagulation bath temperatures ranging from 10 to 70 ℃ and coagulation bath compositions containing up to 51 wt% solvent. It was found that the outward diffusion rate of the solvent and inward diffusion rate of the non-solvent increase as the coagulation bath temperature is increased for both wet spinning and dry-jet wet spinning of the acrylic fibers. Similarly, as the polymer concentration is increased, the diffusion rates of the solvent and non-solvent decrease. Diffusion rate ratios of the solvent to non-solvent were also determined for dry-jet wet spun acrylic fibers. As the coagulation bath temperature was increased, the ratio of the solvent and non-solvent diffusion rates decreased. Using a coagulation bath of 45-49% solvent and coagulation bath temperatures ranging from 10 ℃ to 70 ℃, the fiber cross-sectional shape is best described as non-uniform or unsymmetrical at coagulation bath temperatures of 10 ℃, oval at 45 ℃, and nearly circular at 70 ℃. It can then be summarized that as the coagulation bath temperature is increased, the ratio of the solvent to non-solvent diffusion rate approaches a value of 1, and the cross-sectional shape becomes more symmetric and circular in shape.

Zeng et al.[108] prepared acrylic fibers using dimethylsulfoxide (DMSO) as a solvent, water as a non-solvent, and a polyacrylonitrile terpolymer (polyacrylonitrile-co-methylacrylate-co-itaconic acid, 96/2.5/1.5) using both wet spinning and dry-jet wet spinning techniques. The diffusion rate of both the solvent and non-solvent increased as the extrusion velocity, bath coagulation temperature, and solvent concentration in the coagulation bath increased, for both wet spinning and dry-jet wet spinning. As the solvent and non-solvent diffusion rates increased, the ratio of the solvent diffusion rate to the non-solvent diffusion rate approaches a value of 1. Similar conclusions were drawn that as the ratio of the solvent diffusion rate to the non-solvent diffusion rate approached a value of 1, the fiber cross-sectional shape tends towards a circular shape.

Bajaj et al.[29] studied the structure and property development of three dry-jet wet spun fibers; polyacrylonitrile-co-methyl acrylate (PAN-co-MA), polyacrylonitrile-co-methacrylic acid (PAN-co-MAA), and polyacrylonitrile-co-itaconic acid (PAN-co-IA). PAN-co-MAA fibers were spun into a water/DMF coagulation bath (60/40 v/v) maintained at 10 – 40 ºC, followed by a second water/DMF coagulation bath (90/10 v/v) maintained at 40 ºC, and a third water/DMF (100/0 v/v) coagulation bath maintained at 100 ºC. Fibers were then drawn across a heater plate at 130 ºC. Density of the PAN-co-MAA fibers collected prior to entering the second coagulation bath increased from 1.169 g/cm^3 to 1.177 g/cm^3, as the temperature of the first coagulation bath was reduced from 40 ºC to 10 ºC. The same fiber exhibited a reduction in crystal size from 3.65 nm to 2.29 nm as the temperature of the first coagulation bath was reduced from 40 ºC to 10 ºC. However, the tenacity of the PAN-co-MAA drawn fibers (draw ratio = 6) remained nearly unchanged regardless of the temperature of the first coagulation bath, with tenacity values ranging from 2.23 g/den (10 ºC bath) to 2.30 g/den (40 ºC bath). It can therefore be concluded,

that the internal structure and density of PAN-co-MAA fibers is dependent upon the initial fiber spinning conditions (i.e. coagulation bath temperature), despite similar tensile properties of the fully drawn fibers. The structure of the drawn PAN-co-MAA fibers exhibited differences in % crystallinity and crystal size, with the 10 ℃ spun fibers exhibiting a crystallinity of 61 % and a crystal size of 4.34 nm, and the 40 ℃ spun fibers exhibiting a crystallinity of 55 % and a crystal size of 5.01 nm, both after being drawn to a draw ratio of 6.

In this study, structure-property relationships of dry-jet wet spun and gel spun PAN and PAN/CNT based precursor fibers are investigated. Specifically, the effect of CNT content, polymer solvent, coagulation bath temperature, coagulation bath composition, and polymer molecular weight are explored. Metrics used include the calculated as-spun fiber circularity, fiber surface roughness using scanning electron microscopy (SEM), structure of as-spun and drawn fibers by wide angle x-ray diffraction (WAXD), and tensile properties of drawn precursor fibers. High resolution transmission electron microscopy (HR-TEM) and WAXD were used to observe the carbon fiber structure and single filament tensile testing provided mechanical property measurements of the PAN based carbon fibers. Finally, the relationship between as-spun and drawn PAN fiber structure and properties to that of the carbon fiber are discussed.

3.2 Experimental

3.2.1 Solution preparation

Polyacrylonitrile-co-methacrylic acid (PAN, 96/4 mol%) polymers with a viscosity average molecular weight (M_v) of 247,000 g/mol, 453,000 g/mol, and 513,000 g/mol were obtained from Japan Exlan Co. Ltd. and dried in vacuum at 90 ℃ for 2 days. Few-walled carbon nanotubes (FWNT) were obtained from CCNI (Lot # XOC231U) with 1.1 wt% impurity as determined by thermogravimetric analysis (TGA). *N-N*-dimethylformamide (DMF) and *N-N*-

dimethylacetamide (DMAc) were purchased from Sigma Aldrich and were distilled for further purification. Polymer solutions were prepared by dissolving PAN in the solvent at a concentration of 10.5 g/dL for PAN polymers with M_v = 453k and 513k g/mol, 15 g/dL for PAN polymer with M_v = 247k g/mol. FWNTs were dispersed in distilled DMF or DMAc using 10 – 30 minutes of homogenization, followed by either probe sonication for 30 minutes or 5 cycles in a microfluidizer (Microfluidics Corp.), and 24 hour bath sonication. The concentration of the CNT dispersion was 5 mg/L and the dispersions could be stabilized through the addition of dilute PAN solutions. CNT dispersions were then added to the polymer solution where the excess solvent was removed by vacuum distillation to obtain the desired solution concentration. CNT concentrations with respect to the polymer weight were between 0.1 and 1.0 wt%.

3.2.2 Fiber spinning and drawing

Multi-filament gel spinning was conducted on a spinning system manufactured by Hills Inc. (Melbourne, FL). Various processing conditions were used and are reported at appropriate locations in this article. A 40 or 100-hole spinneret with diameter = 200 μm was used for fiber spinning. A one or two-step gelation condition was used with a solvent/non-solvent mixture in both gelation baths. Coagulation bath temperatures were controlled between – 50 ℃ and 25 ℃. Table 3.1 provides the fiber gelation conditions of the as-spun fibers, which were collected directly after coagulation on a fiber spool using a spin draw ratio (SDR) between 2.0 and 3.2. As-spun fibers were kept immersed in a methanol container maintained at -40 ℃ prior to fiber drawing. Fiber drawing of the 40 or 100 filament tow was conducted in multiple stages, beginning with drawing at room temperature, followed by a two-step hot drawing process on heated godet rollers maintained at 110 ℃ and 185 ℃, respectively. Post spin draw ratios (PSDR) of the precursor fibers is defined by these three draw ratios. The total draw ratio (TDR) is

defined as the SDR multiplied by the PSDR. Fiber samples collected immediately after fiber spinning and prior to fiber drawing will be designated as 'As Spun Sample A', 'As Spun Sample B', etc. Drawn fiber samples collected after post-spin fiber drawing will be designated as 'Precursor A', 'Precursor B', etc. Table 3.2 provides the SDR and total draw ratio of the precursor fibers. Each as spun fiber was drawn to its maximum extent under the condition such that no breakages in the 40 or 100 filament tow were observed throughout the drawing process.

3.2.3 Stabilization and carbonization

Multifilament precursor fiber tows were converted into carbon fiber using small-scale continuous stabilization/carbonization equipment manufactured by Harper International. Stabilization of the precursor fiber using multiple oxidation ovens precedes carbonization using low-temperature (LT) and high-temperature (HT) furnaces. Carbonized fiber samples collected will be designated as 'Carbon Fiber A', 'Carbon Fiber B', etc. As an example, 'As-Spun Sample A' will be drawn into 'Precursor A' and carbonized into 'Carbon Fiber A.' Stabilization temperatures as high as 290 °C were used for Carbon Fibers A and E. All other fibers (Carbon Fibers A_1, A_2, H, I, K, L, and M) were stabilized at temperatures up to 250 °C. Carbonization of all fibers was performed at 1450 °C. Carbon Fibers A_1 and A_2 were manufactured from precursor fibers prepared using the same fiber spinning and drawing protocols as Carbon Fiber A.

3.2.4 Characterization

As-spun fiber cross-sections were imaged using a Leica DM 2500 optical microscope by mounting the as-spun fibers in epoxy (Epofix), and preparing 10 μm thick sections using a Leica DM 2550 microtome. Image analysis was performed using ImageJ (NIH) to determine the as-spun fiber equivalent diameter, circularity index, and roundedness. Circularity index as determined by ImageJ, was calculated using the following equation

$$Circularity = \frac{4\pi A}{(Perimeter)^2}$$

Where *A* is the cross-sectional area and *P* is the perimeter of the filament. Using this circularity index, a perfectly circular filament will have a value of 1, and less circular filaments will have values less than 1.

Roundness as determined by Image J was calculated using the following equation

$$Roundness = \frac{4A}{\pi * MajorAxis^2} = \frac{d_{equiv}^2}{\pi^2 MajorAxis^2}$$

Where *A* is the cross-sectional area, *MajorAxis* is the length of the major axis of the ellipse used to approximate the cross-sectional fiber shape, and d_{equiv} is the equivalent diameter of a circular fiber with the same cross-sectional area.

SEM was performed on a Zeiss Ultra 60 FE-SEM at a working distance of 4 mm and an accelerating voltage of 2 keV. As-spun fiber surfaces were gold sputtered prior to imaging in a Hummer 6 gold/palladium sputtering system. Single filament tensile testing was performed on a Favimat + tensile testing instrument equipped with a vibroscope for *in-situ* linear density measurements. Precursor and carbon fibers were tested using methods previously reported[109], at a gauge length of 25.4 mm, at a strain rate of 1 %/sec and 0.1 %/sec, respectively. WAXD was conducted on 100 filament as-spun fiber bundles, 200 filament precursor fiber bundles, and 200 filament carbon fiber bundles. HR-TEM was performed on a Tecnai F30 (FEI) at an accelerating voltage of 80 keV. TEM samples were prepared through focused ion-beam (FIB) milling (FEI, Nova Nanolab 200 FIB/SEM) of individual fibers mounted on 3-post copper grids (Electron

Microscopy Sciences, Omniprobe lift-out grid) using Gatan G-2 Epoxy. TEM samples were thinned using 30 keV ion-beam voltage prior to final thinning at 5 keV.

3.3 Results and discussion

3.3.1 Effect of CNT loading on cross-sectional shape and precursor fiber structure and properties

Figure 3.1 provides the optical microscopy cross-sections of all As Spun Samples. As Spun Samples A, B, and C are provided in Figure 3.1a, 3.1b, and 3.1c, respectively. As a result of the methanol gelation temperature of -50 °C, the cross-sectional shape of As Spun Samples A, B, and C is irregular. Circularity indices of As Spun Samples A, B, and C (Table 3.1) were calculated to be 0.65, 0.66, and 0.72, respectively.

Table 3.3 contains the structural data obtained from WAXD of the as-spun fibers. As Spun Samples A, B, and C all exhibit similar levels of crystallinity despite distinctly different crystal sizes. There appears to be no correlation between crystal size and CNT content in As Spun Samples A, B, and C.

Drawing of As Spun Samples A, B, and C resulted in total draw ratios of 24.6, 25.8, and 27.2, respectively. The tensile strength of Precursors A, B, and C were measured to be greater than 1 GPa, while the tensile modulus ranged from $20 - 22$ GPa. The structural parameters of Precursor A, B, and C are listed in Table 3.4. Fiber crystallinity and crystal size are independent of CNT loading in Precursors A, B, and C. CNT containing fibers (Precursors B and C) both exhibit higher f_{PAN} as compared to Precursor A as well as a lower 2θ-meridional peak position. The lower 2θ-meridional peak position in Precursors B and C suggests that the addition of CNT contributes to conformational changes of the PAN chains, with a higher propensity for extended chain PAN as compared to a helical conformation.

Table 3.1 Fiber Spinning conditions and image analysis of as spun fiber cross-sections.

Trial	Polymer (M_v, g/mol) / Solvent	CNT Content (wt%)	Coagulation Conditions			Equivalent Diameter (μm)	Circularity Index	Roundedness	Cross sectional shape
			Bath 1 Temperature (°C)	Bath 1 Composition	Bath 2 Temperature (°C)				
As Spun Sample A	513k / DMF	-	N/A		-50	32.0 ± 2.5	0.65 ± 0.09	0.66 ± 0.07	Irregular
As Spun Sample B	513k / DMF	0.1			-50	30.7 ± 2.8	0.66 ± 0.08	0.66 ± 0.09	Irregular
As Spun Sample C	513k / DMF	1.0			-50	31.7 ± 2.1	0.72 ± 0.08	0.66 ± 0.07	Irregular
As Spun Sample D	453k / DMF	0.5			25	33.4 ± 2.1	0.65 ± 0.03	0.64 ± 0.14	Kidney Bean
As Spun Sample E	247k / DMF	-			-50	34.8 ± 2.0	0.61 ± 0.07	0.62 ± 0.06	Irregular/Kidney Bean
As Spun Sample F	247k / DMF	-	25	100:0	-50	34.9 ± 2.2	0.67 ± 0.05	0.71 ± 0.12	Kidney Bean/Dog bone
As Spun Sample G	513k / DMF	-	25	80 : 20	-50	31.7 ± 2.0	0.88 ± 0.05	0.69 ± 0.09	Kidney Bean/Dog bone
As Spun Sample H	513k / DMF	-	25	70 : 30	-50	32.7 ± 2.5	0.93 ± 0.03	0.77 ± 0.08	Dog bone/oval
As Spun Sample I	513k / DMF	-	25	70 : 30	-50	38.9 ± 2.9	0.91 ± 0.04	0.73 ± 0.09	Dog bone/oval
As Spun Sample J	513k / DMAc	0.25	N/A		-50	31.0 ± 2.0	0.85 ± 0.03	0.87 ± 0.05	Irregular/Kidney Bean
As Spun Sample K	513k / DMAc	-			25	31.4 ± 2.6	0.90 ± 0.04	0.69 ± 0.09	Oval
As Spun Sample L	513k / DMAc	-	25	90 : 10	25	31.8 ± 2.4	0.96 ± 0.02	0.86 ± 0.06	Oval/Circular
As Spun Sample M	513k / DMAc	-	25	70 : 30	-50	31.7 ± 2.5	0.96 ± 0.02	0.87 ± 0.06	Oval/Circular

Table 3.2 Draw ratios and mechanical properties of precursor fibers.

Trial	SDR[#]/TDR[*]	Diameter (μm)	Tensile Strength (GPa)	Tensile Modulus (GPa)	Elongation at Break (%)
Precursor A	3.0/24.6	11.2 ± 0.8	1.05 ± 0.13	20.4 ± 0.7	12.1 ± 1.8
Precursor B	3.0/25.8	11.5 ± 0.9	1.00 ± 0.11	20.2 ± 0.8	10.3 ± 0.8
Precursor C	3.2/27.2	11.1 ± 0.8	1.06 ± 0.11	22.1 ± 0.7	11.4 ± 1.2
Precursor D	3.0/39	9.5 ± 0.5	1.16 ± 0.15	20.4 ± 0.6	10.0 ± 1.2
Precursor E	3.0/33.3	12.4 ± 0.6	0.95 ± 0.15	18.4 ± 0.6	12.8 ± 2.1
Precursor F	3.0/33.3	12.3 ± 0.6	0.82 ± 0.11	18.0 ± 0.6	10.8 ± 2.0
Precursor G	3.1/26.4	11.3 ± 0.8	0.84 ± 0.09	18.1 ± 0.8	11.7 ± 1.5
Precursor H	3.2/26.6	11.4 ± 0.7	0.81 ± 0.12	18.4 ± 0.6	10.5 ± 1.7
Precursor I	2.0/24.8	11.4 ± 0.7	1.03 ± 0.09	18.7 ± 0.7	12.8 ± 1.7
Precursor J	3.0/24.9	11.1 ± 0.7	0.94 ± 0.12	18.3 ± 0.7	13.8 ± 2.0
Precursor K	2.5/19.2	12.7 ± 0.9	0.76 ± 0.10	18.3 ± 0.9	12.4 ± 3.2
Precursor L	3.0/24.6	12.2 ± 0.9	0.86 ± 0.11	18.9 ± 0.8	11.8 ± 2.2
Precursor M	3.0/24.6	11.1 ± 0.9	0.81 ± 0.10	19.1 ± 0.8	10.1 ± 1.0

[#] SDR is the spin draw ratio of the fiber (ratio of the take-up speed of the fiber to the extruded velocity of the fiber).

[*] TDR is the total draw ratio of the fiber (SDR multiplied by the draw ratio at each stage of fiber drawing)

Table 3.3 WAXD structural analysis of as-spun fibers.

Trial	Crystallinity (%)	Crystal size (nm)	f_{PAN}	2θ-meridional peak position	$d_{2\theta\sim17°}$
As Spun Sample A	47	3.4	0.15	40.2	0.532
As Spun Sample B	49	5.3	0.28	40.0	0.530
As Spun Sample C	46	2.7	0.13	40.7	0.528
As Spun Sample D	-	-	-	-	-
As Spun Sample E	57	5.6	0.28	40.0	0.526
As Spun Sample F	57	2.4	0.06	40.8	0.534
As Spun Sample G	54	3.1	0.10	40.1	0.526
As Spun Sample H	54	3.2	0.10	40.1	0.525
As Spun Sample I	52	3.1	0.07	40.2	0.525
As Spun Sample J	49	5.3	0.25	40.4	0.525
As Spun Sample K	50	3.4	0.15	40.0	0.527
As Spun Sample L	54	3.2	0.13	40.2	0.527
As Spun Sample M	52	3.6	0.11	39.9	0.525

Table 3.4 WAXD structural analysis of drawn precursor fibers.

Trial	Crystallinity (%)	Crystal size (nm)	f_{PAN}	2θ-meridional peak position	$d_{2\theta\sim17°}$
Precursor A	60	15.2	0.88	39.4	0.527
Precursor B	61	16.4	0.90	39.1	0.525
Precursor C	60	15.4	0.90	39.1	0.526
Precursor D	61	15.7	0.89	39.2	0.524
Precursor E	59	16.0	0.90	39.3	0.529
Precursor F	59	16.2	0.89	39.6	0.527
Precursor G	58	15.2	0.87	39.4	0.527
Precursor H	59	14.1	0.88	39.4	0.527
Precursor I	57	14.3	0.88	39.4	0.531
Precursor J	62	16.3	0.91	39.2	0.525
Precursor K	58	16.3	0.92	39.3	0.526
Precursor L	62	16.0	0.90	39.3	0.526
Precursor M	55	15.4	0.90	39.3	0.525
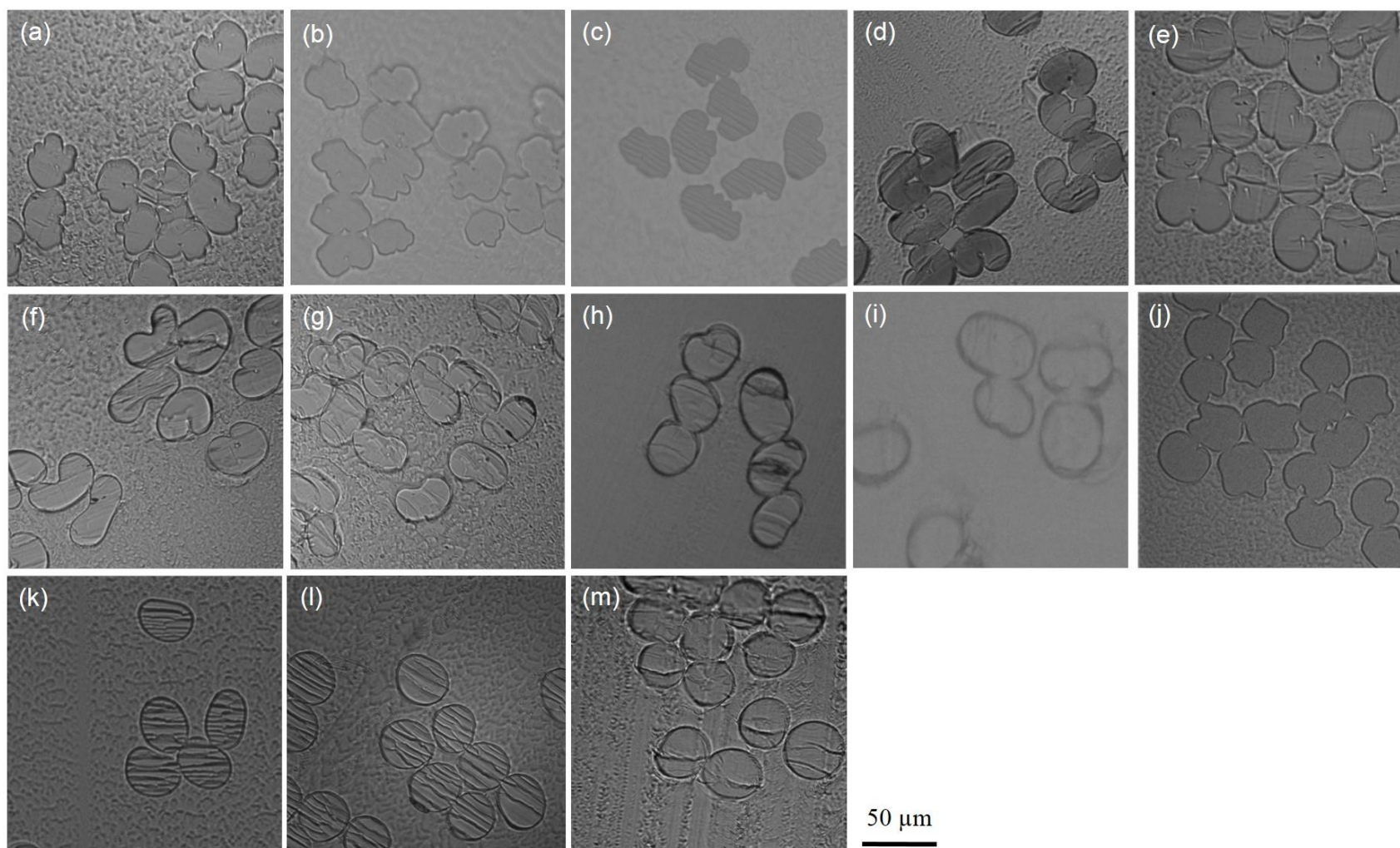
Figure 3.1 Optical microscopy cross-sections of As Spun Sample (a) A, (b) B, (c) C, (d) D, (e) E, (f) F, (g) G, (h) H, (i) I, (j) J, (k) K, (l) L, and (m) M.

As compared to the corresponding As Spun Samples, all three Precursor fibers exhibit higher crystallinity, larger crystal size, higher f_{PAN}, and a lowering of the *2θ*-meridional peak position. The ~10-12 % increase in crystallinity is quite low as compared to the large increase in crystal size during fiber drawing, suggesting that neighboring crystals merge together to form larger crystals with only a 10 − 12 % increase in overall fiber crystallinity during fiber drawing. As the fiber is drawn, the PAN crystallites achieve a higher orientation and the lowering of the *2θ*-meridional peak position.

3.3.2 Effect of gelation bath temperature on cross-sectional shape and precursor fiber structure and properties

The effect of gelation bath temperature on the fiber structure and cross-sectional shape was investigated in PAN and PAN/CNT As Spun Samples. To do so, fibers were gelated in a methanol bath maintained at either -50 ℃ or at room temperature. Optical microscopy cross-sections of As Spun Sample D (25 ℃ methanol coagulation) in Figure 3.1d exhibit a kidney bean shape. Increasing the methanol gelation bath temperature from -50 °C in As Spun Samples A, B, and C, to 25 °C in As Spun Sample D, creates the change in cross-sectional shape from irregular to kidney bean. It is interesting to note that the circularity index of As Spun Sample D does not reflect the observed change in cross-sectional shape in Figure 3.1.

As-Spun Sample D (Precursor D, TDR = 39) resulted in the highest tensile strength amongst all precursor fibers studied, with a measured tensile strength of 1.16 GPa, a crystallinity of 61% and f_{PAN} of 0.89 were determined using WAXD.

Figure 3.1e and 3.1f provide the optical microscopy images of As Spun Samples E and F, respectively. As Spun Sample E (-50 °C methanol gelation) exhibits an irregular cross-sectional shape, similar to that of As Spun Sample A, while As Spun Sample F (25 °C methanol

coagulation) exhibits a kidney bean cross-sectional shape, similar to that of As Spun Sample D. Comparison of Figure 3.1a and 3.1e and Figure 3.1d and 3.1f, indicate that the higher solid content in As Spun Samples E and F have a slight influence on the fiber cross-sectional shape.

Figure 3.2a and 3.2b provide the photographs of the As Spun Sample E and As Spun Sample F wound spools collected immediately after fiber spinning, respectively. It can be observed that the appearance of the two as spun fiber spools is distinctly different, with As Spun Sample E being transparent and yellowish in color, while As Spun Sample F is opaque and whitish in color. Differences in appearances of fibers as a function of coagulation conditions have been attributed to the internal void structure in acrylic fibers[107]. As the size/amount of internal voids is decreased, fibers became more transparent. The higher luster of As Spun Sample E as compared to As Spun Sample F, indicates As Spun Sample E possesses fewer internal voids. However, it has been observed that after fiber drawing the internal voids within the as spun fiber collapse and do not have a significant effect on the drawn precursor fiber appearance and tensile properties[107].

Surface morphology of as-spun fibers observed by SEM is shown in Figure 3.2. Figure 3.2c and 3.2d show the fiber surface of As Spun Sample E and As Spun Sample F, respectively. Differences in the fiber surface are evident between the two fibers, with As Spun Sample F exhibiting larger diameter striations as compared to As Spun Sample E.
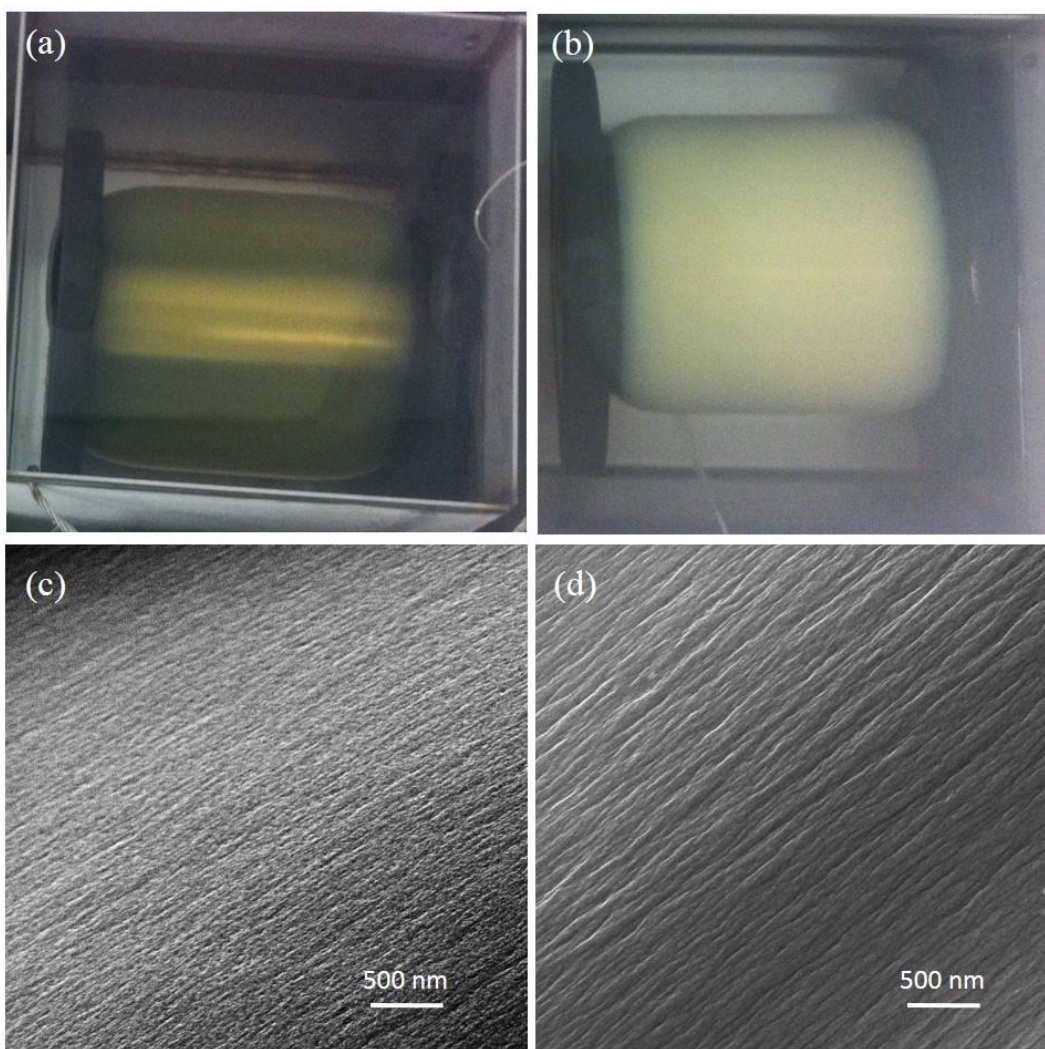
Figure 3.2 Photographs of the as spun fiber spools after fiber winding from the gelation bath for (a) As Spun Sample E and (b) As Spun Sample F. SEM surface images of (c) As Spun Sample E and (d) As Spun Sample F.

Table 3.3 provides the structural analysis of As Spun Samples E and F as determined by WAXD, and these two samples exhibit distinctly different crystal sizes. Despite both fibers possessing 57% crystallinity, As Spun Sample E possesses a 233% larger crystal size as compared to As Spun Sample F, as well as a higher f_{PAN} and a smaller $d_{2\theta\sim17^\circ}$ spacing of the (200,110) crystallographic plane. As Spun Sample E also exhibits a downshift in the meridional-2θ peak position as compared to As Spun Sample F.

Figure 3.3 presents the 2-D WAXD patterns of the as spun fiber, drawn precursor fiber, and the carbon fiber, as well as their corresponding integrated, equatorial, and azimuthal intensity profiles. The crystal structure of PAN can be either hexagonal or orthorhombic. Based upon the shape of *2θ~17°* peak in the as spun fiber integrated intensity profile (Figure 3.3d), as well as the equatorial *d-spacing* of the *2θ~17°* and *2θ~30°* peak positions, the as spun fiber crystal structure is hexagonal or pseudo-hexagonal. Figure 3.4a provides the hexagonal packing structure of PAN. Using the assumption of a perfect hexagonal packing structure and the same crystal length, the differences in crystal structure of As Spun Sample E and As Spun Sample F are depicted in Figure 3.4b and 3.4c, respectively. Considering the crystal size of As Spun Sample E (5.6 nm) and As Spun Sample F (2.4 nm) and their equal levels of crystallinity, the distribution of crystals throughout the fiber is strikingly different. As can be seen in Figure 3.4b and 3.4c, the size of the PAN crystals in As Spun Sample E are larger than in As Spun Sample F, but the estimated total crystallinity of the two schematics is the same, due to the total volume occupied by the crystals. The total number of crystals in As Spun Sample F are ~5.4 times greater than the number of crystals in As Spun Sample E. With the knowledge that As Spun Samples E and F were prepared from the same PAN/DMF solution and the only differences were the gelation bath temperature of the two fibers, the lower gelation bath temperature in As Spun Sample E results in distinctly different PAN crystal sizes as determined by WAXD (Table 3.4, Figure 3.4), as well as fiber surface morphology and fiber luster.
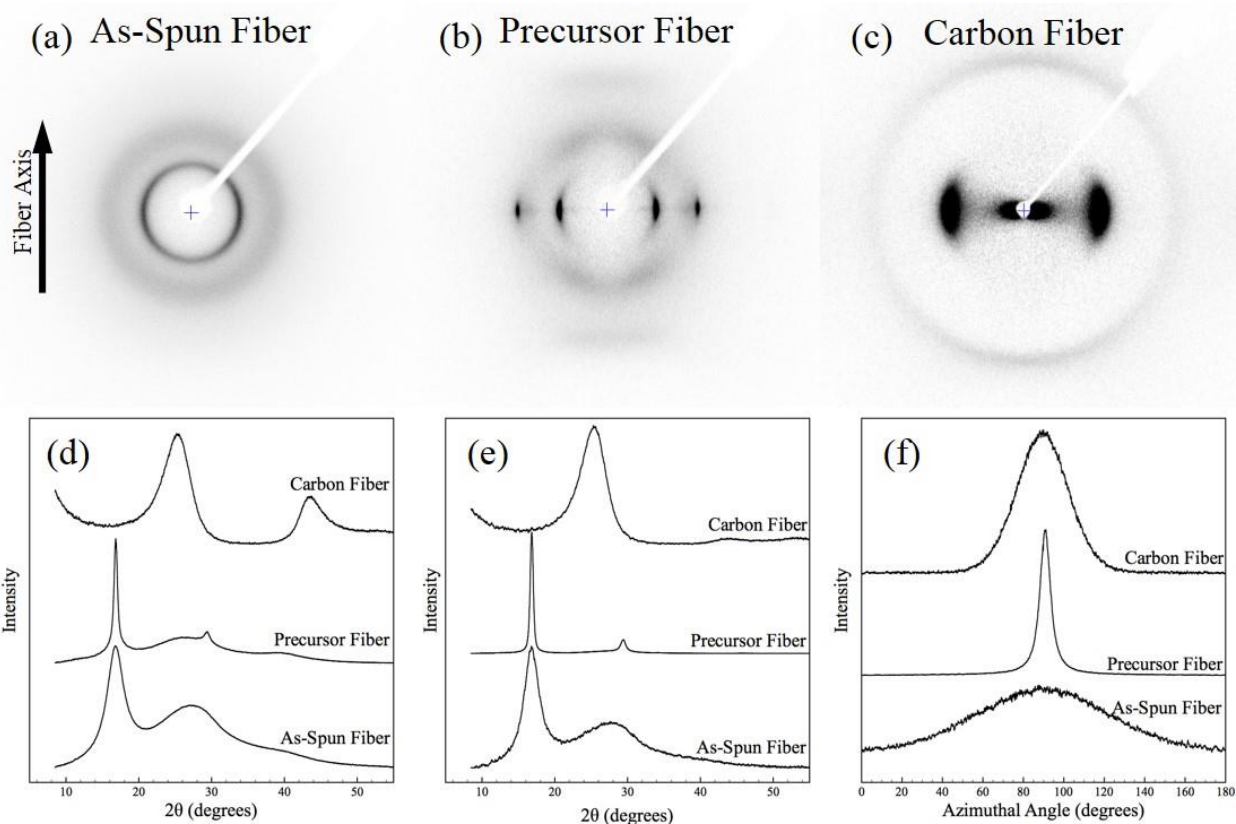
Figure 3.3 2-D WAXD patterns of the gel spun (a) As Spun Sample A, (b) Precursor A, and (c) Carbon Fiber A. WAXD intensity profiles of the (d) integrated, (e) equatorial, and (f) azimuthal scans of the typical as spun fiber, precursor fiber, and carbon fiber.
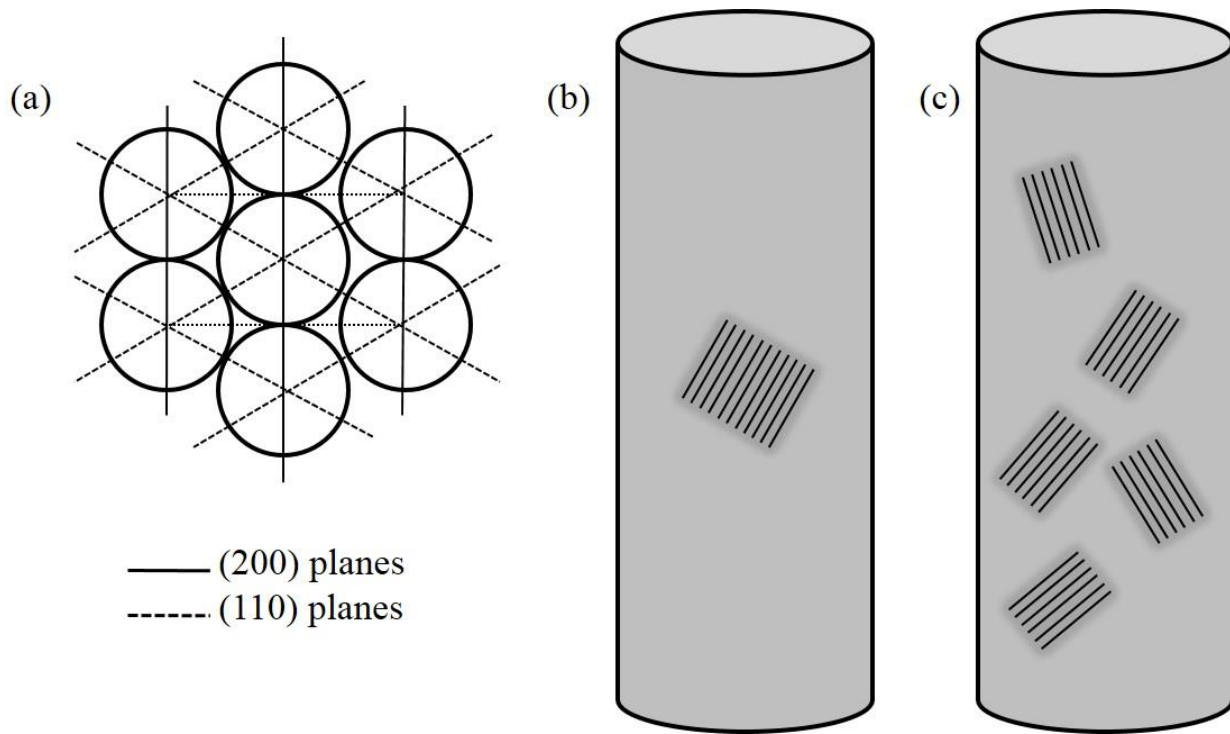
Figure 3.4 (a) Hexagonal crystal structure of PAN and as spun fiber crystal schematics of (b) As Spun Sample E, and (c) As Spun Sample F, depicting the effect of crystal size differences while fiber crystallinity remains constant.

Figure 3.5 presents the DMA data for As Spun Samples E and F, which also shows interesting behavior. Figure 3.5a plots the storage (E') and loss (E'') modulus of the two as spun fibers, and Figure 3.5b plots the *tan δ* behavior of the as spun fibers at a frequency of 10 Hz. E' of As Spun Sample F is higher than the E' of As Spun Sample E from room temperature to ~130 ℃, at which point E' of As Spun Sample E begins to have a higher E' than As Spun Sample F. Differences in the *tan δ* behavior are clearly noticeable, with As Spun Sample E possessing a sharp *tan δ* peak at ~85 ℃, while As Spun Sample F shows an increased *tan δ* peak temperature of ~104 ℃, as well as a reduced *tan δ* peak maximum and a broadening of the *tan δ* peak. Therefore, not only are the crystalline regions of the two as spun fibers different as determined from WAXD, the amorphous regions of the two fibers are also markedly different. As Spun

66

Sample F *tan δ* behavior suggests greater elastic behavior below the glass transition temperature (T_g) and a broader T_g as compared to As Spun Sample E.

Post spin fiber drawing of Precursors E and F resulted in moderately higher fiber crystallinity, as well as increases in crystal size. Both Precursors E and F had an average tensile strength values above 0.8 GPa. The average tensile modulus was 18.4 and 18.0 GPa for Precursors E and F, respectively. However, Precursor E (12.8%) exhibited a higher elongation at break as compared to Precursor F (10.8%).
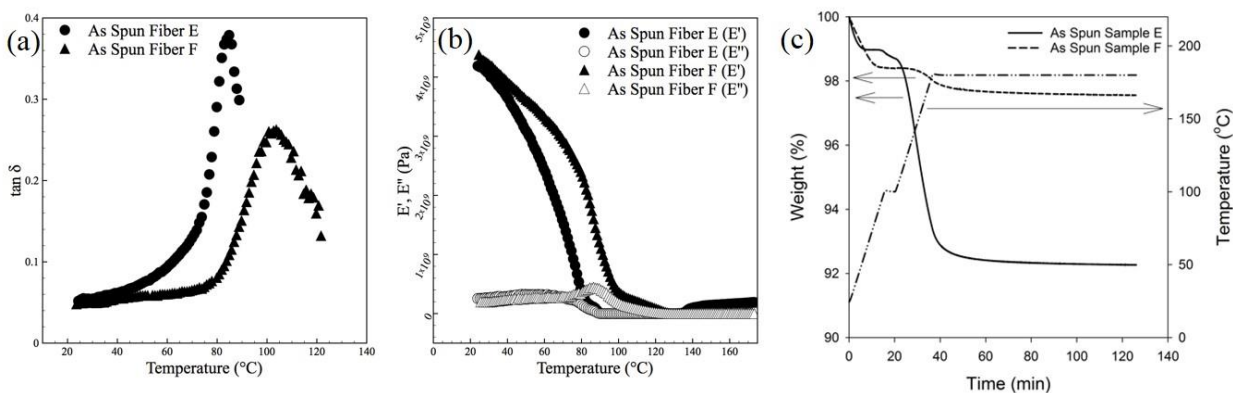
Figure 3.5 (a) Storage and loss modulus and (b) tan δ behavior of As Spun Fibers E and F as determined by DMA at 10 Hz. (c) TGA of As Spun Sample E and F fibers.

3.3.3 Effect of gelation bath composition on cross-sectional shape and precursor fiber structure and properties

From the results presented above on As Spun Samples A-F, the as spun fiber cross-sectional shape, crystal structure, and fiber luster are greatly influenced by the gelation bath temperature. Addition of solvent to the gelation bath while maintaining an elevated bath temperature (room temperature or higher) has been shown to alter the fiber cross-sectional shape as compared to fibers which are coagulated in a coagulation bath with a lower volume fraction of solvent or in a solvent free coagulation bath[27]. In the solvent free bath, the fiber cross-sectional

shape was kidney bean, and as the solvent content increased in the coagulation bath the fiber cross-sectional shape could be described as oval or circular[27]. Figure 3.1 provides the optical microscopy cross-sectional images of As Spun Fibers D, G, H, and I, all of which were gelated in a mixture of MeOH and DMF at room temperature (Table 3.1). Comparison of Figure 3.1d and 3.1g provide visual evidence of a change in the as spun fiber cross-sectional shape as the gelation bath composition is changed from a 100:0 to 80:20 MeOH:DMF bath composition in As Spun Sample D and As Spun Sample G, respectively. The circularity index increases from 0.65 to 0.88 as the DMF content in the gelation bath is raised from 0 vol% to 20 vol% in As Spun Samples D and G. Further increases in the DMF content to 30 vol% in As Spun Sample H (Figure 3.1h) improves the cross-sectional shape, resulting in the circularity index of 0.93.

Figure 3.6a, 3.6b, and 3.6c provide the SEM surface images of As Spun Samples D, G, and H, respectively. From the images, it is possible to see differences in striations along the surface of the fiber, with smaller striations presenting as the DMF content in the gelation bath is increased. Based upon the results in Figure 3.1 and 3.6, as the circularity index of the as spun fibers is increased, the surface morphology exhibits an increased surface roughness along with smaller striations on the fiber surface.
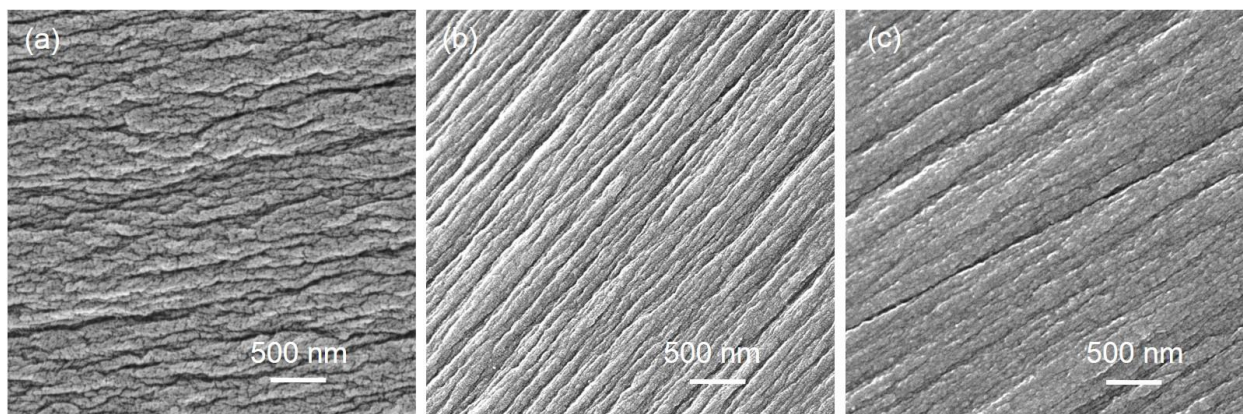
Figure 3.6 SEM surface images of (a) As Spun Sample D, (b) As Spun Sample G, and (c) As Spun Sample H.

Post spin fiber drawing of Precursors G and H increased PAN crystallinity and crystal size, as compared to their corresponding As Spun Samples. The meridional 2θ peak position decreased from $2\theta = 40.1°$ to $2\theta = 39.4°$ after fiber drawing, indicative of a propensity for planar zigzag conformation of the PAN molecules and reduced proclivity of a helical conformation. Correspondingly, the tensile properties of Precursors G and H resulted in tensile strengths of 0.84 GPa and 0.81 GPa, and tensile modulus values of 18.1 and 18.4 GPa, respectively.

In contrast to As Spun Sample H, As Spun Sample I (Figure 3.1i) was manufactured under the same gelation conditions, with a spin draw ratio 2.0, as compared to the typical spin draw ratio applied in this study of $3.0 - 3.2$. As a result of the lower spin draw ratio in As Spun Sample I, the PAN crystallinity, crystal size, and f_{PAN} were all decreased and the 2θ meridional peak position was increased as compared to As Spun Sample H. Due to the lower spin draw ratio, As Spun Sample I could be drawn to a higher post spin draw ratio as compared to As Spun Sample H. As a result of the higher PSDR applied to As Spun Sample I, the tensile strength of Precursor I increased to 1.03 GPa with a measured tensile modulus of 18.7 GPa. In comparison

with Precursor H, Precursor I exhibits a 27% increase in tensile strength and 22% increase in elongation at break.

3.3.4 Effect of organic solvent on cross-sectional shape and precursor fiber structure and properties

Polar aprotic solvents such as DMF, DMAc, and dimethylsulfoxide (DMSO) are typical spinning solvents for the production of PAN fibers. Due to the ternary nature of the phase diagram, which characterizes the thermodynamic relationship between polymer, solvent, and non-solvent, the choice of organic solvent will alter the fiber formation during the solidification process. By altering the choice of solvent from DMF to DMAc or DMSO used for fiber spinning, the interaction parameters between the solvent and polymer and the solvent and non-solvent are modified. Changes in the interaction parameters will result in a modification of the cross-sectional shape of the fiber. Figure 3.1 contains the optical microscopy cross sections of As Spun Samples J-M, which utilized DMAc as the solvent. Comparison of Figure 3.1a and 3.1j depict the difference in cross-sectional shape when using DMF and DMAc as solvent and using a methanol gelation bath maintained at -50 ℃. The circularity index of As Spun Sample J is improved to 0.85, as compared to As Spun Sample A, which has a circularity index of 0.65. Changes in the as spun fiber cross-sectional shape when a room temperature methanol bath is used can be observed by comparing As Spun Sample D (Figure 3.1d) with As Spun Sample K (Figure 3.1k). An improvement in circularity index from 0.65 (As Spun Sample D) to 0.90 (As Spun Sample K) occurs when DMAc is used as the polymer solvent as opposed to DMF. Alteration of the gelation bath composition from 100:0 MeOH:DMAc to 90:10 MeOH:DMAc (Figure 3.1l) results in an increased circularity index from 0.90 to 0.96. Increasing the DMAc concentration in the gelation bath to 70:30 MeOH:DMAc with a bath temperature of 25 ℃

(Figure 3.1m) results in a circularity index of 0.96. This suggests that the optimal processing conditions to produce a circular cross-sectional shape is the use of a room temperature 90:10 MeOH:DMAc gelation bath for the PAN used in this study.

Post spin drawing of As Spun Samples J-M, resulted in Precursors J-M with tensile strengths ranging from 0.76 – 0.94 GPa and tensile modulus values ranging from 18.3 – 19.1 GPa. Precursor J, with 0.25 wt% FWNT loading and – 50 °C gelation bath temperature, exhibits the highest tensile strength (0.94 GPa), while Precursor K exhibits the lowest tensile strength, 0.76 GPa, from fibers prepared with DMAc as the solvent. Precursor K could not be drawn to the same PSDR as the other fibers, which provides an explanation for the lower tensile strength values as compared to Precursors J (0.94 GPa), L (0.86 GPa), and M (0.81 GPa). WAXD structural analysis of Precursor M results in a fiber crystallinity of 55%, and crystal size of 15.4 nm. Such results suggest that as the gelation bath composition contains a larger volume fraction of solvent at an increased gelation bath temperature, fiber circularity improves while the drawn fiber tensile properties and crystallinity are reduced.

3.3.5 Carbonization of gel-spun PAN based carbon fibers

Table 3.5 provides the tensile properties of the PAN based carbon fibers. Carbon fiber tensile strength and modulus values range from 2.6 – 5.2 GPa and 264 – 322 GPa, respectively. Table 3.6 provides the carbon fiber structural parameters as determined by WAXD, while Figure 3.7 provides the cross-sectional and surface SEM images of the PAN based carbon fibers. Carbon Fibers A and E underwent similar stabilization temperatures, as noted in Experimental Section, while the remaining carbon fibers underwent stabilization at lower temperatures that resulted in improved tensile properties. This improvement is shown in the comparison of Carbon

Fiber A and Carbon Fiber A_1, where an 18% improvement in tensile strength is observed for Carbon Fiber A_1.

Figure 3.7a1 provides the SEM cross-sectional fracture surface of Carbon Fiber A, which maintains the irregular shape observed in As Spun Sample A (Figure 3.1a). In comparison to the irregular cross-sectional shape observed in Carbon Fiber A, Carbon Fiber H possesses the highest circularity index from fibers manufactured with DMF as the solvent. Carbon Fiber H (Figure 3.7c1), manufactured using a room temperature gelation bath with 30 vol% DMF, possesses a tensile strength of 3.9 GPa and a tensile modulus of 315 GPa. Differences in the carbon fiber surface morphology also exist in Carbon Fibers A and H. Carbon Fiber A (Figure 3.7a3 and 3.7a4) and Carbon Fiber H (Figure 3.7h3 and 3.7h4) retain similar fiber surface features that were observed in the corresponding As Spun Samples. Carbon Fiber A exhibits a smooth carbon fiber surface whereas Carbon Fiber H shows striations along the fiber axis. HR-TEM images of Carbon Fiber A center in Figure 3.8a1 and edge in Figure 3.8a2 exhibit a distinct turbostratic crystallite structure in both the carbon fiber center and edge. In contrast, the turbostratic crystallite structure in Carbon Fiber H center (Figure 3.8b1) and edge (Figure 3.8b2) is not as readily distinguishable as in Carbon Fiber A, indicative of a reduced sheath-core effect in the carbon fiber structure.

Table 3.5 Mechanical properties of gel spun PAN based carbon fibers at a gauge length of 25.4 mm.

Trial	Diameter (μm)	Tensile Strength (GPa)	Tensile Modulus[#] (GPa)	Strain to Failure (%)
Carbon Fiber A[*]	5.1 ± 0.4	4.4 ± 1.1	316	1.49 ± 0.31
Carbon Fiber A$_1$[^]	5.2 ± 0.3	5.8 ± 1.4	357	1.70 ± 0.39
Carbon Fiber A$_2$[^]	5.0 ± 0.3	5.6 ± 1.3	375	1.64 ± 0.34
Carbon Fiber E[*]	6.7 ± 0.5	2.6 ± 0.7	282	1.00 ± 0.23
Carbon Fiber H[^]	5.4 ± 0.3	3.9 ± 1.1	337	1.25 ± 0.33
Carbon Fiber I[^]	5.9 ± 0.3	3.6 ± 1.2	345	1.15 ± 0.35
Carbon Fiber K[^]	6.9 ± 0.4	4.0 ± 0.9	332	1.31 ± 0.26
Carbon Fiber L[^]	5.3 ± 0.5	4.0 ± 1.3	304	1.49 ± 0.53
Carbon Fiber M[^]	5.8 ± 0.3	3.6 ± 1.4	342	1.13 ± 0.42

[*] Carbon Fibers A and E underwent similar stabilization temperatures, ranging from 200 – 290 °C.

[^] Carbon Fibers A$_1$, A$_2$, H, I, K, L, and M underwent similar stabilization temperatures, ranging from 180 – 250 °C.

[#] Compliance corrected tensile modulus.

Table 3.6 WAXD structural analysis of PAN and PAN/CNT based carbon fibers.

Trial	d_{002} (nm)	L_{002} (nm)	d_{10} (nm)	L_{10} (nm)	f_{002}	$FWHM_{002}$
Carbon Fiber A[*]	0.347	1.64	0.210	2.46	0.86	28.1
Carbon Fiber A$_1$[^]	0.345	1.86	0.210	2.30	0.87	25.1
Carbon Fiber A$_2$[^]	0.344	1.82	0.210	2.49	0.87	25.7
Carbon Fiber E[*]	0.346	1.72	0.210	2.16	0.84	29.9
Carbon Fiber H[^]	0.345	1.84	0.210	2.35	0.88	26.3
Carbon Fiber I[^]	0.346	1.84	0.210	2.27	0.88	25.8
Carbon Fiber K[^]	0.346	1.91	0.210	2.37	0.85	28.7
Carbon Fiber L[^]	0.346	1.90	0.210	2.54	0.86	27.1
Carbon Fiber M[^]	0.345	1.80	0.210	2.23	0.87	25.6

[*] Carbon Fibers A and E underwent similar stabilization temperatures, ranging from 200 – 290 °C.
[^] Carbon Fibers A$_1$, H, I, K, L, and M underwent similar stabilization temperatures, ranging from 180 – 250 °C.
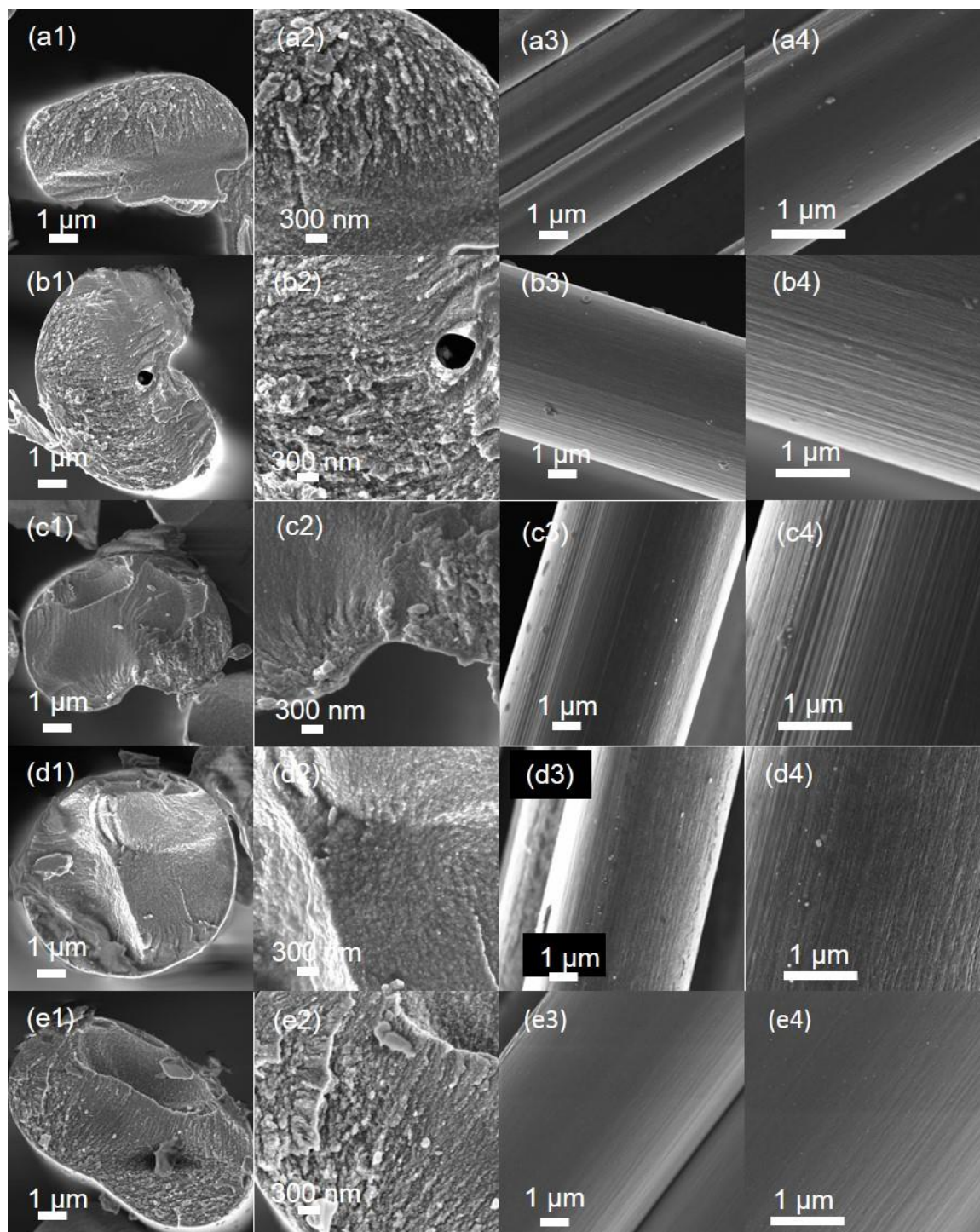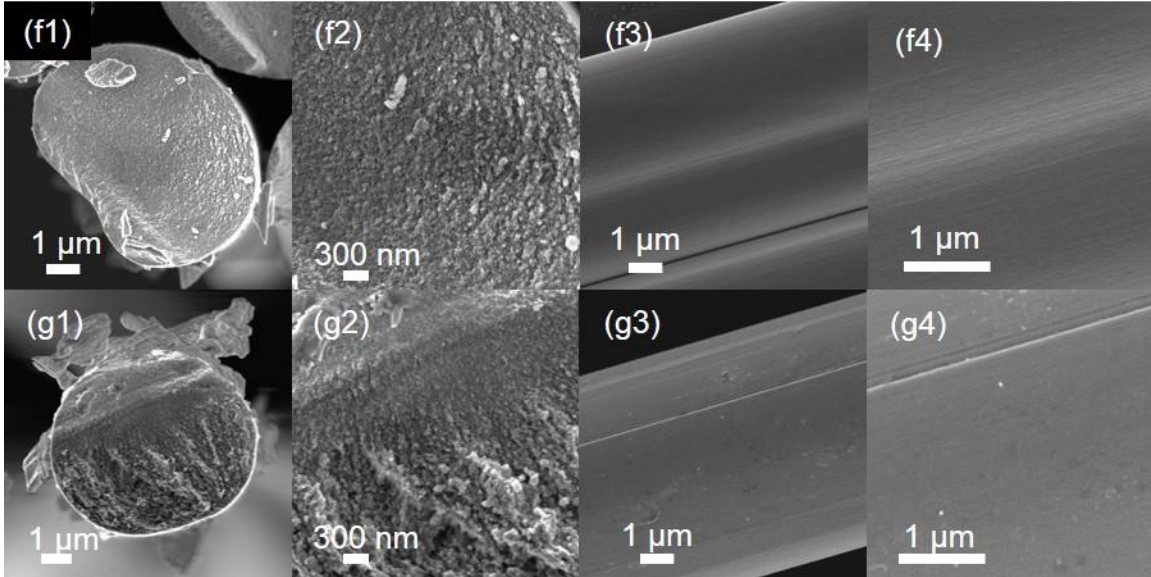
Figure 3.7 Low magnification SEM cross-sectional images of Carbon Fiber (a1) A, (b1) E, (c1) H, (d1) I, (e1) K, (f1) L, and (g1) M. High magnification SEM cross-sectional images of Carbon Fiber (a2) A, (b2) E, (c2) H, (d2) I, (e2) K, (f2) L, and (g2) M. Low magnification SEM surface images of Carbon Fiber (a3) A, (b3) E, (c3) H, (d3) I, (e3) K, (f3) L, and (g3) M. High magnification SEM surface images of Carbon Fiber (a4) A, (b4) E, (c4) H, (d4) I, (e4) K, (f4) L, and (g4) M.

Carbon Fiber E has the lowest tensile strength (2.6 GPa) and tensile modulus (264 GPa) of the carbon fibers manufactured from the gel spinning process. It is interesting to note that Precursor E has an ~11% lower tensile strength and tensile modulus as compared to Precursor A, while Carbon Fiber E has an ~69% and 12% lower tensile strength and tensile modulus as compared to Carbon Fiber A, respectively. The significantly lower tensile strength of Carbon Fiber E can partially be attributed to the lower molecular weight PAN utilized in the manufacture of Precursor E as compared to Carbon Fiber A. During the thermal conversion of the precursor fiber in carbon fiber, the higher likelihood of PAN chain ends in Precursor E will act as defect sites in Carbon Fiber E, and as a result is expected to produce a carbon fiber of lower tensile strength as compared to Carbon Fiber A[73].

Figure 3.7e1, 3.7f1, and 3.7g1 provide the cross-sectional SEM images of Carbon Fibers K-M, manufactured with DMAc as the solvent. Carbon Fibers K and L both possess a tensile strength of 4.0 GPa, while Carbon Fiber M has a tensile strength of 3.6 GPa. It is interesting to note that despite the improved circularity of Carbon Fibers K-M, as compared to Carbon Fiber A, the tensile strength of the more circular fibers is lower than that of the irregularly shaped Carbon Fiber A. Unlike Carbon Fibers A and H which were manufactured from DMF and show differences in fiber surface roughness, Carbon Fibers K-M do not show striations along the fiber surface. The HR-TEM transverse cross-sectional images of Carbon Fibers K and M are provided in Figure 3.8c1 and 3.8c2 and Figure 3.8d1 and 3.8d2, respectively. Carbon Fiber K shows the similar random orientation of turbostratic crystallites throughout the cross-section that are observed in Carbon Fibers A and H. Alternatively, Carbon Fiber M exhibits preferentially oriented turbostratic crystallites in the transverse HR-TEM cross-section. The oriented turbostratic crystallites observed in the transverse cross-section of Carbon Fiber M is distinct from the turbostratic structure in Carbon Fibers A, H, and K.
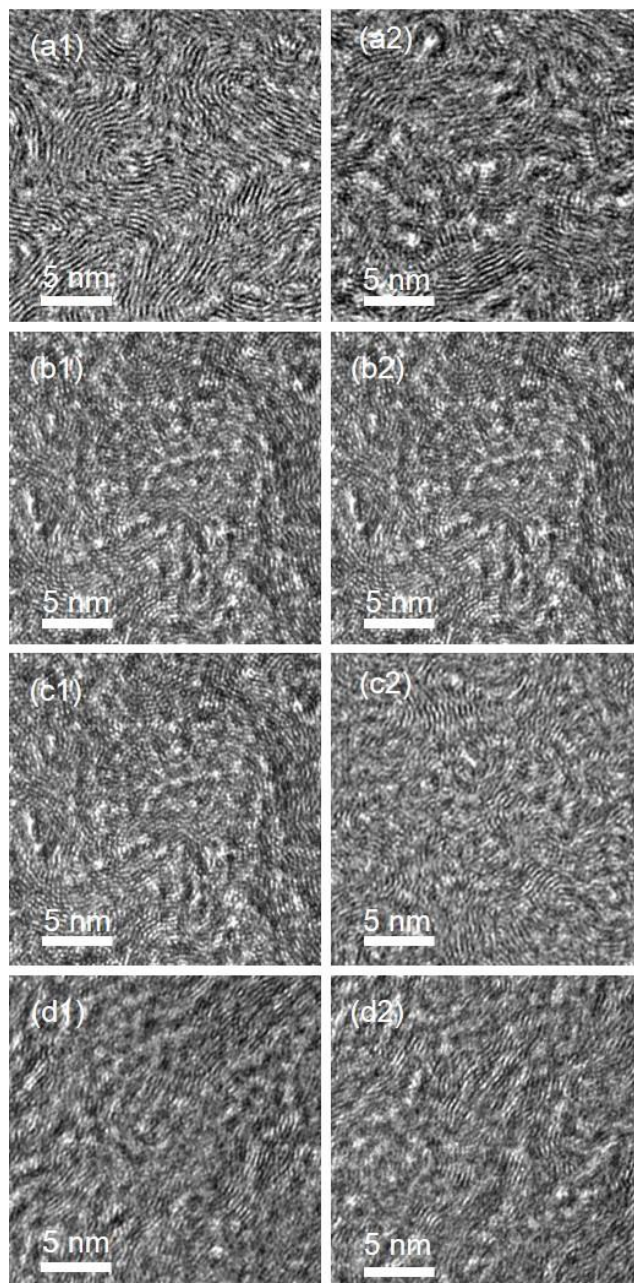
Figure 3.8 HR-TEM transverse cross-section images of Carbon Fiber (a1) A center, (a2) A edge, (b1) H center, (b2) H edge, (c1) K center, (c2) K edge, (d1) M center, and (d2) M edge.

3.4 Conclusions

PAN and PAN/CNT fibers were manufactured using a gel spinning technique using DMF or DMAc as a solvent and a solvent-free or solvent/non-solvent gelation bath maintained at -50 °C to 25 °C. As spun PAN and PAN/CNT fibers exhibited similar

irregular cross-sectional shapes when gelated at -50 °C in methanol, with increasing as spun fiber circularity as the gelation bath temperature and solvent concentration was increased. Increased gelation bath temperature and solvent content in the gelation bath resulted in smaller striations on the as spun fiber surface, indicative of higher surface roughness. As spun fibers manufactured with DMAc as the solvent resulted in higher circularity fibers as compared to similarly manufactured fibers where DMF was used as the solvent. Despite the differences in gelation bath conditions, drawn precursor fibers exhibited tensile strengths and tensile modulus values from 0.76 – 1.16 GPa and 18.0 – 22.1 GPa, respectively. Carbonization of the PAN precursor fibers resulted in fibers with tensile strengths as high as 5.8 GPa and tensile modulus as high as 375 GPa. Reduction of the molecular weight of the PAN copolymer during precursor fiber manufacture resulted in a carbon fiber tensile strength and modulus of 2.6 GPa and 282 GPa, respectively. These results are a point of reference for the mechanical properties of gel spun PAN based carbon fibers manufactured from a PAN precursor fiber prepared from the PAN copolymer with M_v = 247,000 g/mol. Further process optimization is required for an adequate comparison with the gel spun PAN based carbon fibers manufactured from the PAN copolymer with M_v = 513,000 g/mol. The cross-sectional shape of the PAN based carbon fibers could be altered from irregular to circular cross-section, through the use of different spinning solvents, increased coagulation bath temperatures, and increased solvent concentration in the coagulation bath. Adjustment of the fiber spinning parameters listed, not only impacts the cross-sectional shape of the resulting carbon fiber, but the internal structure development. It will be essential to manufacture PAN based

carbon fibers with the internal structure present in the high strength and high modulus gel

spun PAN based carbon fibers that possess a circular cross-sectional shape.

Chapter 4
STRESS TRANSFER IN POLYACRYLONITRILE/CARBON NANOTUBE FIBERS

4.1 Introduction

PAN/CNT composite fibers have successfully been processed using dry-jet wet spinning[33-35], gel-spinning[25, 36], and electrospinning[37, 38]. Improvements in the tensile properties of the PAN/CNT fibers as compared to the similarly processed PAN fibers provide evidence of stress transfer from the polymer matrix to the CNT[25, 34]. CNTs exhibit well-defined Raman spectra as well as stress-induced Raman band shifts which have been investigated in individual single walled carbon nanotubes (SWNTs)[52, 53] as well as in epoxy/CNT[63] and polymer/CNT composites[110, 111]. Downshifts (lowering vibrational frequency) in CNT D (~1300 cm^{-1}), G (~1590 cm^{-1}) and G' (~2580 cm^{-1}) Raman band peak positions are attributed to the stretching and weakening of the carbon-carbon bond[56]. It was shown that the G' band shift is the most sensitive to the induced strain[52], and is therefore typically monitored for stress or strain transfer in polymer/CNT composites[112].

In the current study, gel-spun PAN and PAN/CNT fibers containing up to 1 wt% few-walled carbon nanotubes (FWNTs) were processed using techniques described elsewhere[25]. CNT quality, extent of CNT dispersion, and the effect of fiber drawing are examined by monitoring the stress induced G' Raman band shift to characterize the stress transfer in the gel-spun PAN/CNT composite fibers. These results are expected to impact the processing and properties of the PAN/CNT composite fibers and the resulting carbon fibers[36, 104, 113].

4.2 Experimental

4.2.1 Materials and fiber processing

CNTs were obtained from Continental Carbon Nanotechnologies, Inc. (CCNI, Lot # XOC231U) and Unidym, Inc. (Lot # XO122UA). TEM images of the two types of CNT, XOC231U (CNT-A)(Figure 4.1a) and XO122UA (CNT-B)(Figure 4.1b) used in this study are provided, as well as their corresponding Raman spectra (Figure 4.2), which were obtained using a 785 nm laser on a Kaiser Raman Microscope System. Raman spectra show a higher G/D band ratio for CNT-A as compared to CNT-B, indicating a more perfect structure for CNT-A. Table 4.1 provides the summary of the material characteristics for CNT-A and CNT-B as determined by TGA (% impurity)[114], extensional rheology (aspect ratio), Raman spectroscopy (*G/D* band ratio), and TEM (average diameter and number of walls). Extensional viscosity was measured with a Trimaster Capillary Thinning Rheometer[115] for solutions of 0.05 wt. % CNT-A and CNT-B dissolved in chlorosulfonic acid. The theory of Shaqfeh and Fredrickson for semidilute rigid rod solutions[116] was then used to determine the CNT aspect ratios from the extensional viscosity of the CNT solutions[117]. The average CNT diameter and average number of walls were determined by analyzing TEM images of both CNT-A and CNT-B. CNT density was calculated based on the average CNT diameter and the average number of walls determined by TEM. Approximately 10% of CNT-A and 4% of CNT-B were determined to be SWNTs. Details of the density calculations are provided elsewhere[118-120]. CNT-A and CNT-B were dispersed using 24 hour bath sonication at a concentration of 2 mg/L in dimethylformamide (DMF) before placing on a transmission electron

microscopy (TEM) grid (C-Flat 200 mesh, Electron Microscopy Sciences) and by drying

at 40 ℃ for two days prior to TEM observation.
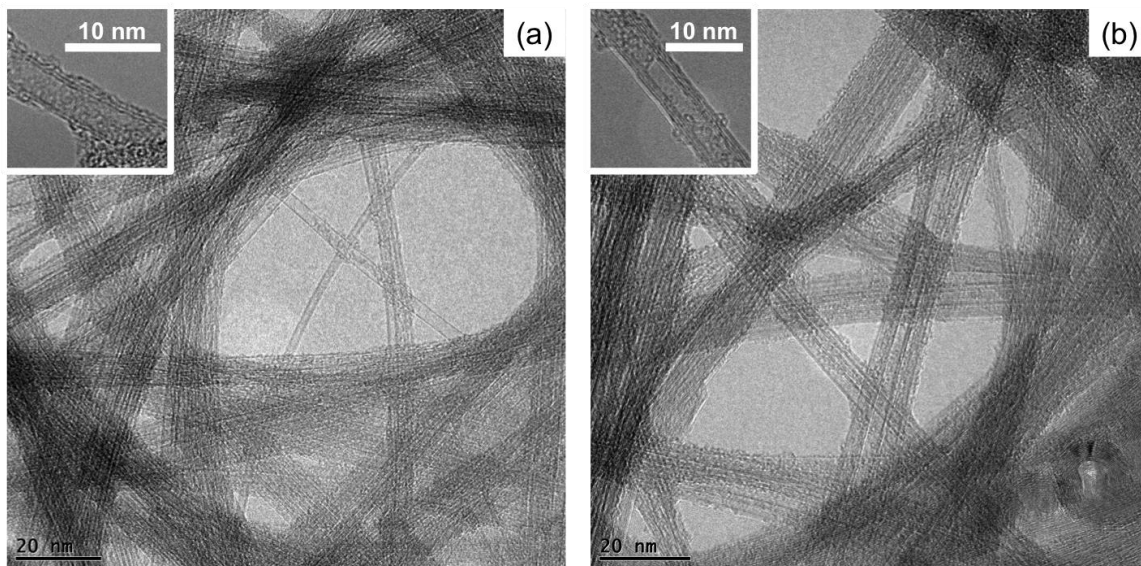
Figure 4.1. TEM images of the two kinds of CNTs used in this study (a) CNT-A and (b) CNT-B. CNT-A has a smaller diameter, lower impurity content, and larger aspect ratio as compared to CNT-B.
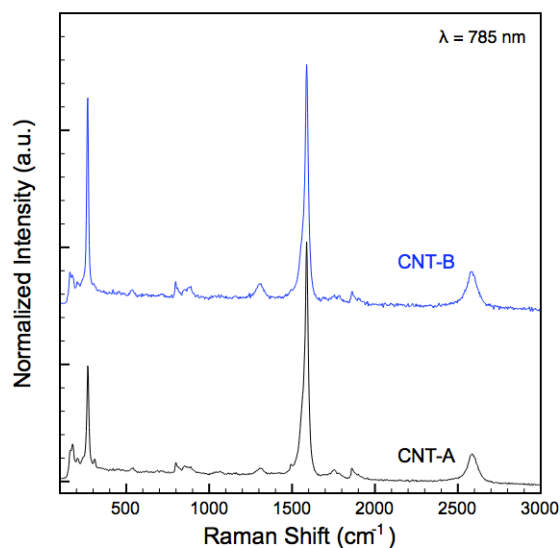
Figure 4.2. Raman spectra of CNT-A and CNT-B CNTs. CNT-A has a G/D band ratio of ~42 and CNT-B has a G/D band ratio of ~17.

Table 4.1. Material properties of CNT-A and CNT-B as determined by TGA, Raman spectroscopy, extensional rheology, and TEM. 30 CNTs were averaged for diameter and number of wall measurements.

	% Impurity* (wt%)	Raman G/D Ratio	Aspect Ratio (L/D)**	Average Diameter (nm)	Average Number of Walls	Calculated Density (g/cm^3)
CNT-A	1.1	42	2820 ± 200	2.7	2.6	1.66
CNT-B	3.3	17	1050 ± 50	3.0	2.6	1.60

PAN and PAN/CNT solutions were prepared at a solid concentration of 10.5 g/dL using a polyacrylonitrile-co-methacrylic acid copolymer, (PAN-co-MAA) (96/4 by weight) with a viscosity average molecular weight of 513,000 g/mol (Japan Exlan, Osaka, Japan). CNTs were dispersed in distilled DMF (Sigma Aldrich). CNT-A was used for two fiber spinning trials, where CNT concentration was 1.0 and 0.1 wt% with respect to the weight of the polymer. These samples are referred to as CNT-A and CNT-A(0.1), respectively. CNT-A was dispersed at a concentration of 7 mg/L using 24 hour bath

84

sonication (Branson 8510-MT), and CNT-A(0.1) was dispersed using a dispersion concentration of 10 mg/L using 30 minutes of homogenization (IKA T18) prior to 30 minutes of horn sonication (QSonica, Q700 Series) in an attempt to further disperse the CNTs during solution processing due to the higher sonication power of the horn sonicator. CNT-B was dispersed at a concentration of 25 mg/L using 60 minutes of homogenization prior to 24-hour bath sonication. CNT-B concentration in the fiber was 1 wt% with respect to the weight of the fiber. It has been observed by dynamic light scattering and the preparative ultracentrifuge method that the bundle diameter of CNT-A when dispersed at a concentration of 10 mg/L using 24 hours bath sonication resulted in a CNT bundle diameter of 22.9 ± 2.6 nm. CNT-B was dispersed at a concentration of 30 mg/L under 24 hours of bath sonication and yielded a bundle diameter of 12.8 ± 1.4 nm[121]. These results indicate that CNT-A is more difficult to disperse than CNT-B due to its longer length, and therefore the dispersion concentrations for CNT-A and CNT-B should be different. A spinning system supplied by Hills Inc was used for all fiber spinning trials. Fibers were gel-spun using a 100-hole spinneret (diameter, D=200 μm, length to diameter (L/D) ratio of 5) maintained at 85°C with a solution flow rate of 0.5 cc/min/hole. Fibers were extruded through an air gap of 19 mm into a methanol bath maintained at -50 °C, and were collected at a spin draw ratio of 3. These fibers were subsequently kept immersed in methanol at -40 °C for two days prior to drawing. Post spinning fiber drawing was done in three stages using godet rolls maintained at room temperature (CDR), 110 °C (HDR1), and 185 °C (HDR2). Various fiber processing conditions, tensile properties and structural parameters are listed in Table 4.2.

Table 4.2. Material processing information, G' Raman band shift rate, maximum G' Raman band shift, mechanical properties, and structural information of the PAN and PAN/CNT fibers.

	As-Spun PAN (25S2)	Drawn PAN (25S2D2)	As-Spun PAN/CNT-A (36S1)	Drawn PAN/CNT-A (36S1D2)	Drawn PAN/CNT-A(0.1) (26S1D5)	Drawn PAN/CNT-B (29S1D2)
CNT Concentration (wt%)	-	-	1.0	1.0	0.1	1.0
CNT Dispersion Concentration (mg/L)	-	-	7	7	5	25
Spin Draw Ratio	3	3	3	3	3	3
Post Spin Draw Ratio (CDR x HDR1 x HDR2)*	-	1.1 x 2.27 x 3.2	-	1.1 x 2.27 x 3.32	1.1 x 2.27 x 3.36	1.1 x 2.18 x 3.46
Raman Shift Rate, S_r (cm^{-1}/%)	-	-	-6.2	-28.4	-48.8	-10.5
Maximum G' Shift (cm^{-1})	-	-	-3.1	-7.3	-12.8	-3.5
Effective Diameter (μm)	31.7 ± 0.01	11.2 ± 0.8	32.0 ± 0.0	11.1 ± 0.8	11.5 ± 0.9	11.1 ± 0.9
Tensile Strength (GPa)	0.12 ± 0.01	1.05 ± 0.13	0.11 ± 0.00	1.06 ± 0.11	1.01 ± 0.11	1.03 ± 0.11
Tensile Modulus# (GPa)	5.7 ± 0.4	21.1 ± 0.7	6.4 ± 0.4	24.5 ± 0.8	21.7 ± 0.9	21.5 ± 0.9
Elongation at Break (%)	118 ± 32	12.1 ± 1.8	111 ± 42	11.5 ± 1.3	10.3 ± 0.8	10.5 ± 1.0
Interfacial Shear Strength (MPa)			13.1	30.9	44.3	14.6
Measured Density (g/cc)	-	1.1956 ± 0.0005	-	1.2014 ± 0.0003	1.1996 ± 0.0006	1.1974 ± 0.0008
Calculated Density (g/cc)	-	-	-	1.1989	1.1959	1.1986
Crystallinity (%)	47	60	49	60	61	61
X_c (nm)	3.4	15.2	3.4	15.4	16.1	17.9
2θ-meridional Peak (degree)	40.2	39.4	40.2	39.1	39.1	39.1
$d_{(\sim17°)}$	5.32	5.27	5.27	5.26	5.25	5.25
$d_{(\sim30°)}$	3.02	3.04	3.04	3.04	3.03	3.04
$d_{(\sim17°)}/d_{(\sim30°)}$	1.759	1.733	1.734	1.732	1.730	1.729
f_{PAN}	0.15	0.88	0.16	0.90	0.90	0.90
f_{CNT}	-	-	0.712	0.932	0.943	0.925

* Cold Draw Ratio (CDR, Room Temperature), Hot Draw Ratio 1 (HDR1, 110 ℃), Hot Draw Ratio 2 (HDR2, 185 ℃)

Compliance corrected modulus

4.2.2 Characterization

Single filament tensile testing was performed using FAVIMAT tensile testing instrument at 25.4 mm gauge length, at a strain rate of 1 %/s. Fiber linear density was measured on each filament using the inline vibroscope on the FAVIMAT. Compliance correction was done by testing the fibers at gauge lengths of 50.8, 25.4, 12.7, and 6 mm at a strain rate of 1 %/s. Density measurements were conducted at room temperature using a Micromeritics pycnometer with a 1 cm^3 volume cell and ~275 mg of fiber. 25 measurement cycles were conducted to determine the fiber density. Wide-angle x-ray diffraction (WAXD) was conducted on 200 filament bundles using previously described methods[25]. Raman spectra were collected on 100 filament bundles to determine CNT orientation using a Holoprobe Research 785 Raman Microscope made by Kaiser Optical System (λ = 785 nm) using parallel (VV) and crossed (VH) polarizers, with the fiber axis rotated in 10º increments from 0 – 90º. Equation 4.1 was used to determine CNT orientation f_{CNT} [122] in the PAN/CNT fibers (Table 4.2), and this equation was simultaneously solved for three variables (r, $<P_{200}>$, and $<P_{400}>$). Due to the evidence that Raman tensor ratio (r) has been shown to vary when molecules are under stress[123], Equation 4.1 is considered to be more accurate determination of CNT orientation than other methods[124]

$$R(\theta) = \frac{I_\perp(\theta)}{I_\parallel(\theta)} = \frac{(1-r)^2[-56-40\langle P_{200}\rangle+(105 cos4\theta-9)\langle P_{400}\rangle]}{[-56(8r^2+4r+3)+40(4r^2-r-3)(1+3cos2\theta)\langle P_{200}\rangle-3(r-1)^2(9+20cos2\theta+35cos4\theta)\langle P_{400}\rangle]} \qquad (4.1)$$

where

$$\langle P_{200}\rangle = \frac{3\langle cos^2\theta\rangle-1}{2} \qquad (4.2)$$

$$\langle P_{400}\rangle = \frac{3-30\langle cos^2\theta\rangle+35\langle cos^4\theta\rangle}{8} \qquad (4.3)$$

and $I_\perp$ and $I_{//}$ are the Raman scattering intensities when the analyzer is polarized perpendicular and parallel to the polarization direction of the incident beam, respectively. θ is the angle between the fiber axis and the polarization direction.

Raman spectra were collected during single filament deformation at a gauge length of 50.8 mm by mounting single filaments onto paper tabs and adhering with cyanoacrylate adhesive. Filaments were strained in 100 μm steps using a stretching rig, with Raman spectra taken at each strain at 5 mW power for 10 seconds in VV mode with the fiber aligned parallel to the polarizer and analyzer directions. Three individual filaments were tested from each fiber sample, and the average of the three spectra was used for data analysis, while individual figures are plotted. TEM characterization was performed on a Tecnai F30 (FEI) at an accelerating voltage of 80 keV. Scanning electron microscopy (SEM) was performed on tensile fractured specimens using a FEI NOVA Nanolab 200 FIB/SEM at 5 kV at a working distance of 5 mm. For SEM observation, fiber samples were sputter coated using a Hummer 6 gold/palladium coater.

4.3 Results and discussion

4.3.1 Effect of CNT quality on the stress transfer efficiency

As the purity, level of perfection, and the aspect ratio of the CNT used in the composite fibers are improved, the interaction between the PAN and the CNT should also improve. Residual impurities on the CNT walls will act as a physical barrier to PAN/CNT interaction, limiting stress transfer. Smaller diameter CNTs should be preferred due to increasing bond strain with decreasing CNT diameter[125]. Imperfections in the CNT will reduce the strength of the CNT as compared to a CNT with a perfect structure, limiting the stress transfer capability of the more imperfect CNT. As expected, increases in CNT aspect ratio in epoxy/CNT samples resulted in

increased stress transfer efficiency, signifying the importance of high aspect ratio CNTs in the matrix[126]. Between the two CNTs used in this study, CNT-A is regarded as the higher quality CNT due to its lower level of residual impurity, higher Raman G/D intensity ratio, higher aspect ratio, and smaller average diameter than CNT-B, as indicated in Table 4.1.

By monitoring the G' Raman band shift in PAN/CNT-A and PAN/CNT-B (Figure 4.3), quantitative observations can be made. PAN/CNT-A exhibits a G' Raman band shift rate (S_r) of -28.4 cm^{-1}/% strain, while PAN/CNT-B exhibits a S_r of -10.5 cm^{-1}/% strain. PAN/CNT-A fiber has a maximum G' band downshift (S_m) of -7.3 cm^{-1}, while S_m in PAN/CNT-B is -3.2 cm^{-1}.

Addition of 1 wt% CNT-B shows a modest 2% increase in compliance corrected modulus over the similarly produced PAN gel-spun fiber (Table 4.2). On the other hand, the addition of 1 wt% CNT-A increases the compliance corrected tensile modulus by 16%. Therefore, the differences in the stress transfer between PAN/CNT-A and PAN/CNT-B fibers can be attributed to the differences in CNT-A and CNT-B, considering the similar level of CNT alignment (f_{CNT}) in both fibers (Table 4.2). Stress transfer differences between PAN/CNT-A and PAN/CNT-B can, in large part, be attributed to the differences in the aspect ratio and impurity content of CNT-A and CNT-B (Table 4.1).
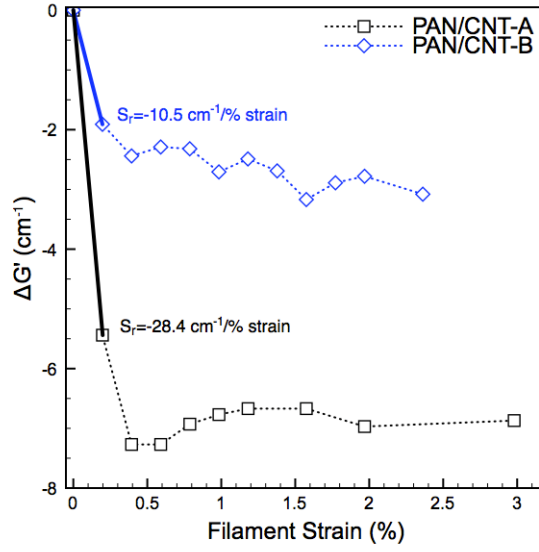
Figure 4.3. ΔG' as a function of filament strain for drawn PAN/CNT-A and drawn PAN/CNT-B fibers. Both fibers were prepared with 1 wt% CNT.

The modulus of the composite fiber can be predicted from Equation 4.4, assuming that there is no morphological change in the structure of PAN between control PAN and PAN/CNT fibers.

$$E_{comp} = (E_{PAN})V_{PAN} + (E_{CNT})_{||}V_{CNT} \tag{4.4}$$

Where, E_{PAN} is the modulus of the PAN fiber, V_{PAN} is the volume fraction of PAN, E_{CNT} is the modulus of the CNT along the fiber axis, and V_{CNT} is the volume fraction of CNT. E_{CNT} along the fiber axis can be calculated using the experimentally determined CNT orientation in the PAN fiber [127, 128] from Equation 4.5

$$\frac{1}{\langle E_{CNT} \rangle} = \frac{1}{E_2} + \left(\frac{1}{G_{12}} - \frac{2v_{12}}{E_1} - \frac{2}{E_2} \right) \langle cos^2\theta \rangle + \left(\frac{1}{E_1} + \frac{1}{E_2} - \frac{1}{G_{12}} + \frac{2v_{12}}{E_1} \right) \langle cos^4\theta \rangle \tag{4.5}$$

where E_1 is the longitudinal modulus, E_2 is the transverse modulus, G_{12} is the in-plane shear modulus, and v_{12} is Poisson's ratio of the CNTs. Using the elastic constants listed in Table 4.3 and the second ($<P_{200}>$) and fourth ($<P_{400}>$) order orientation parameters as determined by Equation 4.1, listed in Table 4.4, E_{CNT} could be determined for each fiber. It can be noted that the elastic constants of CNTs are dependent upon the diameter and number of walls in the CNT, and that the SWNT tensile modulus is dependent only upon its diameter[119]. Here we use the constants listed in Table 4.3, where the moduli of the two CNTs (E_{CNT-A} and E_{CNT-B}) are based on the graphite modulus of 1060 GPa and the densities of the two CNTs (ρ_{CNT-A} and ρ_{CNT-B}) being 1.66 g/cm^3 and 1.60 g/cm^3. Calculations based on Equation 4 results in E_{comp} values for PAN/CNT-A and PAN/CNT-B composite fibers of 21.7 and 21.6 GPa, respectively. In these calculations, E_{PAN} of 21.1 GPa was used from the control PAN fiber in Table 4.2, and V_{PAN} was 99.3 % based on 1 wt % (0.7 vol% CNT). Drawn PAN/CNT-A fiber has a 13% increase in tensile modulus over the predicted tensile modulus using Equations 4.4 and 4.5, whereas drawn PAN/CNT-B fiber does not show an improvement over the predicted tensile modulus with 1 wt% CNT-B loading.

Table 4.3. Elastic constants of CNTs used in Equations 4.4 and 4.5.

Properties		Reference
$E_{1, CNT-A}$ (GPa)	779	
$E_{1, CNT-B}$ (GPa)	750	
E_2 (GPa)	50	129
G_{12} (GPa)	4	130
v_{12}	0.14	131

Table 4.4. CNT orientation (f_{CNT}, Eq. 4.1) and corresponding CNT modulus as calculated by Eq. 4.5. Predicted and measured compliance corrected modulus of PAN and PAN/CNT fibers. E_{comp} is predicted from Equations 4.4 and 4.5.

	$f_{CNT}, <P_{200}>$	$<P_{400}>$	E_{CNT} (GPa) (Eq. 4.5)	E_{comp} (Eq. 4.4, Eq. 4.5)	Compliance Corrected Modulus (GPa)
Drawn PAN	-	-	-	-	21.1
As-Spun PAN	-	-	-	-	5.7
As-Spun PAN/CNT-A	0.712	0.372	32	5.9	6.4
Drawn PAN/CNT-A	0.932	0.810	95	21.7	24.5
Drawn PAN/CNT-B	0.925	0.807	93	21.6	21.5
Drawn PAN/CNT-A(0.1)	0.943	0.822	100	21.2	21.7

Pycnometer measurements show that the densities of the drawn PAN/CNT fibers are moderately higher than that of the drawn PAN fiber (Table 4.2). The density (ρ) of the composite precursor fiber can be predicted using Equation 4.6, assuming the same PAN morphology in the PAN and the PAN/CNT fibers.

$$\rho = \rho_{PAN}(V_{PAN}) + \rho_{CNT}(V_{CNT}) \tag{4.6}$$

Where, the measured density of the control gel-spun PAN (ρ_{PAN}) fiber is 1.1956 g/cc (Table 4.2). Higher density of the PAN/CNT composite fiber is expected as compared to the PAN control fiber, due to the higher density of the CNT. PAN/CNT-A fibers exhibit a density value greater than that predicted by Equation 4.6, whereas PAN/CNT-B fiber exhibits a density lower than the predicted density (Table 4.2).

Differences in predicted and measured modulus and density in the PAN/CNT-A fiber may be due to an interfacial crystallization occurring in the PAN on the surface of CNT-A. Although interfacial crystallization is not directly observed in the PAN/CNT-A fiber, the

improvements in tensile modulus and increased density versus their predicted values indicate that it may be occurring within the fiber. Interfacial crystallization has been reported in PAN/SWNT fibers[25] and in PAN/SWNT solutions[132] where a highly ordered extended chain PAN structure is reported to be developed in the vicinity of CNT. These highly ordered PAN regions are expected to exhibit higher modulus and density than the less ordered PAN away from the CNT. If interfacial crystallization is occurring in the PAN/CNT-A fiber (Figure 4.4a) and not in the PAN/CNT-B fiber (Figure 4.4b), a higher than predicted modulus and density for the PAN/CNT-A fiber would be expected due to the extended chain structure formed in the PAN/CNT-A fiber
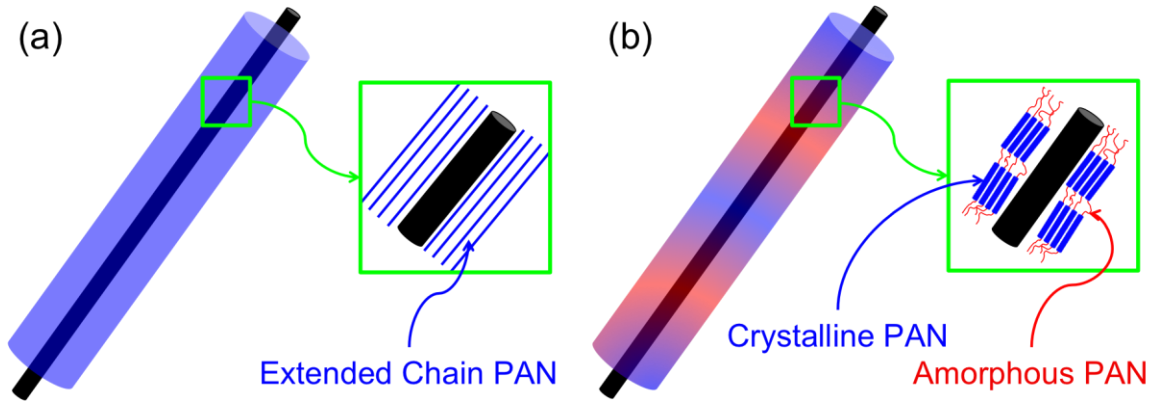
Figure 4.4. Schematics of the crystallization in the vicinity of the CNTs and CNT bundles. (a) Extended chain crystallization due to templating off the CNT and (b) crystal structure of polyacrylonitrile fiber not directly influenced by the CNT.

Addition of CNTs in PAN based nanocomposites has been shown to introduce structural changes within the fiber[25], such as increased crystallinity, increased crystallite orientation (f_{PAN}), reduction in the transverse intermolecular ($d_{(2\theta \sim 17^\circ)}$)-spacing, and a decrease in the meridional 2θ peak of $\sim 40^\circ$. Based upon the structural fiber parameters (Table 4.2) in this study, the addition of CNTs shows a decrease in the $d_{(2\theta \sim 17^\circ)}$-spacing, an increase in f_{PAN}, as well as a decrease in the

meridional peak position ($2\theta \sim 40^\circ$) and increased crystal size (X_c). Reduction of the $d_{(2\theta \sim 17^\circ)}$-spacing has been ascribed to the load sharing of the CNTs and PAN crystals[133] while the increase in f_{PAN} in the PAN/CNT fibers can be attributed to the long length of the CNTs within the fiber which align neighboring PAN crystals during fiber drawing. Decrease in the 2θ-meridional peak position is characteristic of a reduction in PAN helical sequences and increase of planar zigzag sequences[17] and has been shown previously in the PAN/CNT fibers[25, 36, 133]. Increased X_c for the PAN/CNT fibers has previously been reported in the dry-jet wet spun and gel-spun PAN/CNT fibers[34-36].

4.3.2 Effect of CNT dispersion on stress transfer efficiency

Raman spectroscopy has proven to be useful for determining the aggregation state of SWNTs produced by the HiPCO process[134]. In particular, the 267 cm^{-1} normalized peak intensity, attributed to the (10,2) tube, can be monitored for de-bundling and eventual exfoliation of the SWNTs[135]. Changes in resonant behavior are not limited to the (10,2) tube, and has been expanded upon[136] to include a larger data set. Strong RBM peaks are due to the resonant enhancement created by the matching of the electronic transition energy of a specific SWNT chirality with the incident laser energy. The electronic transition energy of the SWNT is altered by SWNT bundling. Therefore, bundling of SWNTs will result in Raman spectra, particularly the RBM, which are significantly different from that of individualized SWNTs. Differences in the bundled and individualized spectra are attributed to the altered electronic transition energies of the SWNTs in the bundled and individualized states. Understanding this allows for the RBM peaks to be monitored as a method for comparing the aggregation state of SWNTs in polymer nano composite samples.
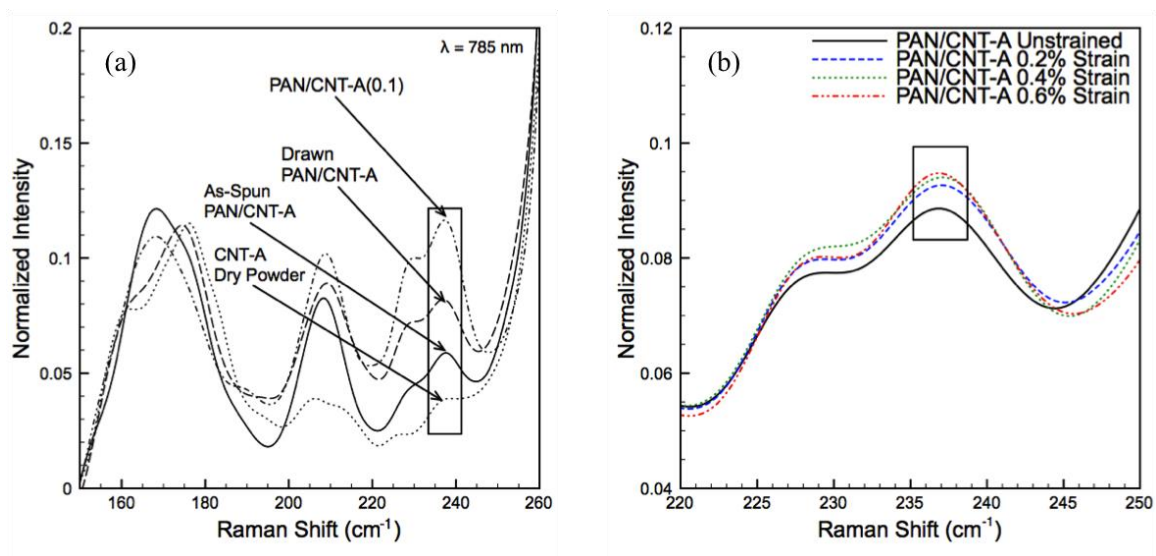
Figure 4.5. (a) Normalized Raman spectra of CNT-A dry powder, as-spun PAN/CNT-A fiber, drawn PAN/CNT-A fiber, and drawn PAN/CNT-A(0.1) fiber. (b) Drawn PAN/CNT-A fiber normalized Raman spectra ($\omega = 220 - 250$ cm^{-1}) as a function of fiber strain.

Previous results indicate that during the processing of PAN/SWNT fibers, SWNTs can de-bundle and exfoliate producing resolved van Hove transitions in the UV-VIS spectra[25]. Using the knowledge that fiber processing can result in SWNT de-bundling, we compare the RBM spectra of dry CNT-A powder, as-spun PAN/CNT-A fiber, and drawn PAN/CNT-A fiber in Figure 4.5a. Considering that the RBM peaks can be attributed to a specific SWNT chirality whose electronic transition energy is altered through CNT bundling, an RBM peak with large intensity differences during fiber processing is selected. For this reason, the 237 cm^{-1} peak is selected to be used to compare the bundling behavior of CNT-A as a function of fiber processing.

The 237 cm^{-1} peak can be attributed to the (12,1) semiconducting tube or the (10,4) metallic tube. Using the equation $\omega_{rbm} = A/d_t + B$[137] where A is 223.5 cm^{-1} and B is 12.5 cm^{-1}, the (12,1) tube has a calculated diameter of 0.995 nm ($\omega_{rbm} = 237.2$ cm^{-1}), while the (10,4) tube has a calculated diameter of 0.992 nm ($\omega_{rbm} = 237.9$ cm^{-1}). The (12,1) tube has a calculated

95

transition maxima of 12516 cm^{-1} (1.552 eV)[138] while the (10,4) tube has a calculated transition maxima of 17504 cm^{-1} (2.172 eV)[139]. Due to the (12,1) tube being in closer resonance to the incident 785 nm laser (1.58 eV), the 237 cm^{-1} peak observed in our spectra can be ascribed to the (12,1) tube. Figure 4.5b shows an increase in the *G*-band normalized intensity for the drawn fiber as it is strained, signifying increased resonance during straining of the PAN/CNT-A fiber and thus straining of the CNTs within the fiber. Based upon work by Yang and Han[140], the electronic structure of the SWNT can be predicted as a function of strain. For the (12,1) tube, E_{22}^s increases from 1.552 eV[138] (unstrained) to 1.588 eV at 0.4% strain, indicating that the (12,1) tube is coming into resonance during fiber strain under excitation from the 785 nm laser. This correlates well with the plot in Figure 4.5b, where the normalized peak intensity of the 237 cm^{-1} peak saturates at ~0.6% strain. It should be noted that the *G'* peak position plateaus at ~0.4% strain in the PAN/CNT-A fiber, indicating that the CNTs, in particular the (12,1) tube might not be experiencing the same strain as the PAN/CNT-A composite fiber, and will be discussed later in further detail. The (12,1) tube has a strong overlap in its excitation profiles in both the bundled and 'individualized' states, allowing for the (12,1) tube to be observed in both the bundled and 'individualized' state[141], it serves as a useful peak for determining the aggregation state of CNT-A by using only one laser energy of 1.58 eV (λ=785 nm). In the bundled state, it was found that the roped/bundled (12,1) tubes had a transition energy maxima of 12115 cm^{-1} (1.501 eV)[136], while the individualized (12,1) tube had a transition energy maxima of 12626 cm^{-1} (1.565 eV)[141]. Due to the transition energy of the 'individualized' (12,1) tube being 15 meV off resonance from the 785 nm (1.58 eV) laser, and the roped/bundled (12,1) tube being 79 meV off resonance from the incident laser, the peak intensity of the individualized (12,1) tube at ω_{rbm} = 237 cm^{-1} will be stronger than that of the bundled (12,1) tube. These results coupled with the

RBM peak intensities provided in Figure 4.5a confirm that PAN/CNT-A(0.1) has better dispersed CNTs as compared to PAN/CNT-A, and can be attributed to the higher sonication power of the horn sonicator despite the higher dispersion concentration and reduced sonication time for PAN/CNT-A(0.1).

Use of improved CNT dispersions during the solution preparation, ultimately results in reduced CNT bundle size and increased surface area for interaction with the PAN matrix. Therefore, the stress transfer between PAN and the CNTs can be considerably enhanced. Increased G' Raman band shift rates have been previously noted with increased sonication times for PVA/SWNT composite films[67]. By improving upon the CNT dispersion that was used in PAN/CNT-A, the S_r of PAN/CNT-A(0.1) is improved to -48.8 cm^{-1}/% strain and the S_m is improved from -7.3 to -12.8 cm^{-1} (Figure 4.6a). Monitoring the G' band peak shift and its simultaneous peak width allows for further insight into the stress transfer from PAN matrix to CNT (Figure 4.6b, Figure 4.6c). As PAN/CNT-A is strained, the lengthening of the carbon-carbon bond in the CNTs is nearly evenly distributed among the CNTs, as well as along the length of the CNT, creating a small increase in the G' band peak width during the extent of straining. The G' band peak width in PAN/CNT-A shows a maximum of a 2% increase in peak width during straining, indicating a nearly uniform global interaction between PAN and CNT as the fiber is strained. In the case of PAN/CNT-A(0.1), the G' peak width shows an increase of 15% at a fiber strain of 0.8%, indicating an uneven straining of the carbon-carbon bonds within the CNTs. Uneven straining of the carbon-carbon bonds could be a result of differences in the local interaction between the PAN matrix and the CNTs, particularly the strength of the interaction. Both the presence of the physical interaction and the strength of the interaction will vary not only from CNT to CNT but also along the length of each CNT. If the entire surface of the CNT does

not have the same interfacial interaction with the PAN matrix prior to straining, large increases in the *G'* band peak width can be expected. In the case of PAN/CNT-A(0.1) the *G'* band peak width exhibits an increasing broadening reaching a maximum at 0.8% fiber strain. At 0.8% fiber strain, the *G'* band peak width reaches a maximum and begins to decrease as the macroscopic PAN/CNT-A(0.1) fiber is further strained. It can be imagined that along the length of an individual CNT, some regions of the CNT can transfer the stress from the PAN matrix better than other areas, indicating differences in local PAN/CNT interaction. As the fiber is strained, the local regions with improved stress transfer from the PAN to the CNT create a large downshift in the *G'* band peak position. Other regions of the CNT which do not have the same stress transfer capabilities are not contributing as strongly to the *G'* band downshift as those regions which have an improved stress transfer capability.
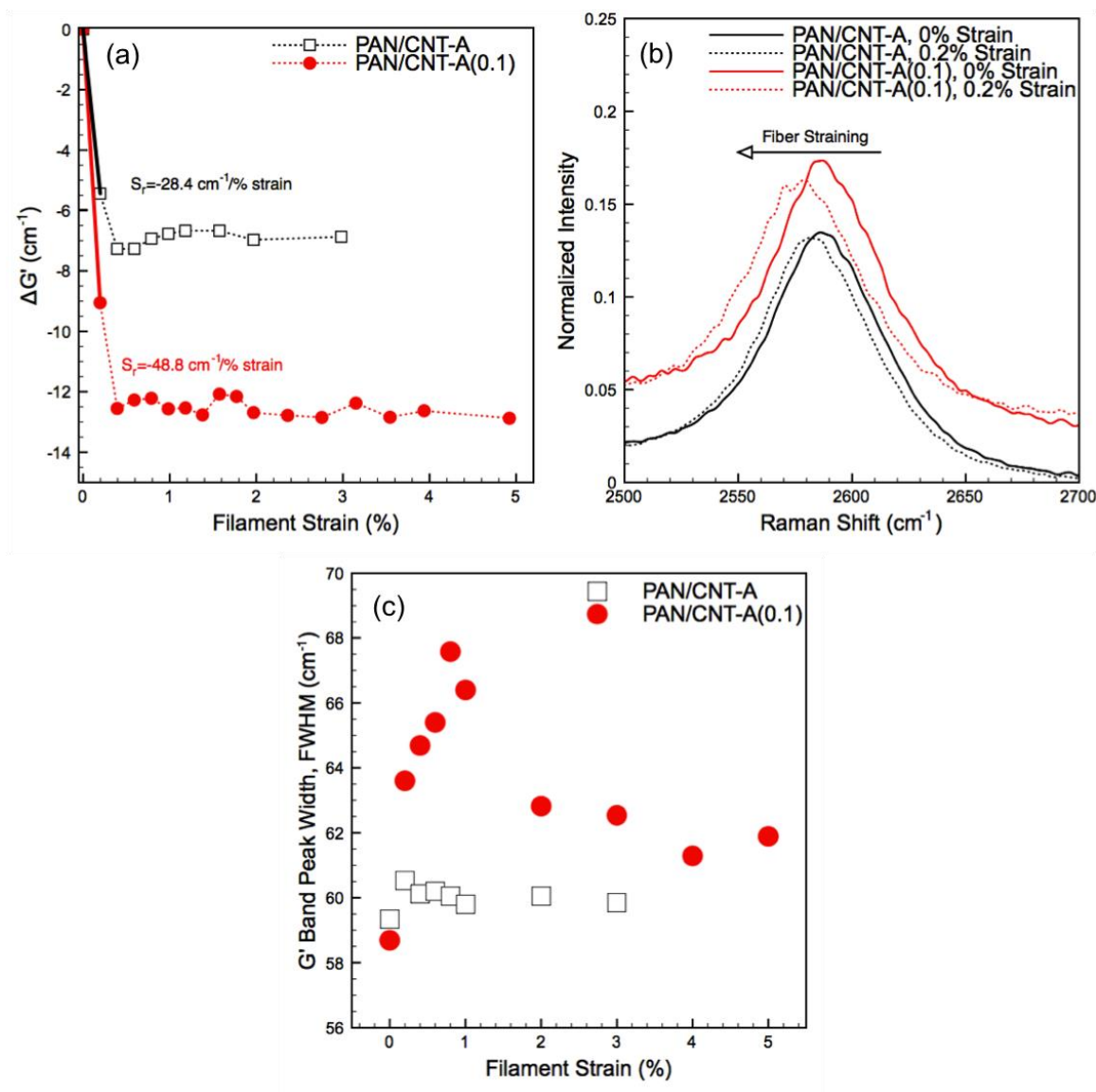
Figure 4.6. (a) Raman $\Delta G'$ as a function of strain for fibers PAN/CNT-A and PAN/CNT-A(0.1). PAN/CNT-A(0.1) exhibits an average G' Raman band shift rate of -48.8 cm^{-1}/% as compared to -28.4 cm^{-1}/% for PAN/CNT-A. G' Raman band shift plateaus above 0.4% strain. (b) G' Raman band spectra before and after 0.2% strain. PAN/CNT-A(0.1) is vertically shifted for clear comparison. (c) G' Raman band peak width as a function of strain.

99

4.3.3 Effect of fiber drawing on stress transfer efficiency

Raman spectroscopy was used to track the shift of the G' Raman band peak position during tensile deformation of both the as-spun and drawn PAN/CNT-A fibers (Figure 4.7) to determine the effect of fiber drawing on the stress transfer efficiency. Three distinct differences manifest themselves when comparing the G' Raman band shift as a function of fiber strain when comparing drawn and as-spun fibers. The first is the S_r of -6.2 cm^{-1}/% strain and -28.4 cm^{-1}/% strain for the as-spun and drawn PAN/CNT-A fibers, respectively. The second is the strain at which the G' Raman band peak shift reaches a plateau. Based upon the sensitivity of our experiment, this strain occurred at approximately 1% for the as-spun PAN/CNT-A fiber, and at approximately 0.4% for the fully drawn PAN/CNT-A fiber. Thirdly, the S_m in the as-spun and drawn PAN/CNT-A fibers is significantly different. Drawn PAN/CNT-A fiber exhibits a S_m of $-$ 7.3 cm^{-1} as compared to the as-spun PAN/CNT-A fiber which exhibits an S_m of -3.1 cm^{-1}. Comparison of the S_r in differently prepared samples is difficult due to the fact that S_r is dependent not only on the CNT orientation, but also on the polymer morphology which in turn will depend on the processing history[67, 111]. Drawn PAN/CNT-A fiber has significantly higher PAN crystallinity, crystallite orientation, crystal size, and CNT orientation as compared to the as-spun PAN/CNT-A fiber, as reported in Table 4.2. For these reasons, a more useful comparison between the as spun and drawn PAN/CNT-A samples is in their S_m rather than the S_r. The larger S_m in the drawn PAN/CNT-A fiber is evidence of an improved PAN/CNT interface in the drawn PAN/CNT-A fiber as compared to the as-spun PAN/CNT-A fiber, and can be attributed to the structural changes that occur during the drawing process. During the drawing process, some CNT de-bundling also takes place[25] thus resulting in increased available CNT surface area for interaction with the PAN matrix.
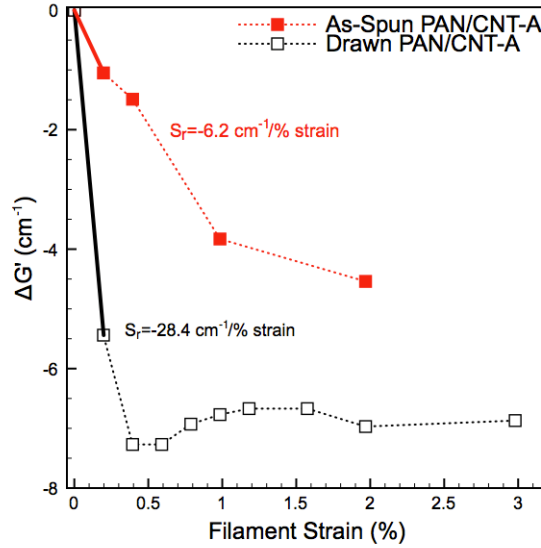
Figure 4.7. ΔG' as a function of strain for as-spun PAN/CNT-A and drawn PAN/CNT-A fibers. Drawn PAN/CNT-A fibers have an increased total G' Raman band shift as compared to the as-Spun PAN/CNT-A fiber, providing evidence that fiber drawing increases the PAN-CNT stress transfer. As-spun PAN/CNT-A fibers continue to show stress transfer up to approximately 1% strain, which is higher than that typically cited in literature of ~0.35-0.4% and is consistent with our drawn fiber samples.

SWNT and polymer orientation has been shown to have an effect on the S_r in PVA/SWNT electrospun fibers and films, where the more aligned electrospun fiber has higher S_r as compared to the undrawn film[67]. By processing gel-spun as-spun and fully drawn PAN/CNT fibers, the effect of CNT orientation (f_{CNT}, $<P_{200}>$) on the stress induced Raman band downshifts can be monitored. By plotting the normalized depolarization ratio ($I_\perp/I_{//}$) as a function of angle, Equation 4.1 can be used to fit the data and determine r, $<P_{200}>$, and $<P_{400}>$ for both the as-spun PAN/CNT-A and fully drawn PAN/CNT-A fibers (Figure 4.8). CNT de-bundling is also observed by monitoring the normalized G-band peak intensity of the 237 cm^{-1} peak in Figure 4.5a. As the dry CNT-A powder is dispersed by sonication and processed into the as-spun

PAN/CNT-A, and drawn PAN/CNT-A fibers, the 237 cm^{-1} peak intensity continues to increase, signifying continued de-bundling as the (12,1) peak comes into resonance with the 785 nm laser, which was discussed above.

Low and high magnification scanning electron micrographs of the tensile fracture surfaces of the as-spun and drawn PAN/CNT-A fibers are shown in Figure 4.9. At high magnification, it is possible to distinguish the CNT-A bundles protruding from the fibrillar structure in the drawn Figure 4.9b and Figure 4.9c) and as spun fiber (Figure 4.9e and Figure 4.9f). Image analysis of the fracture surfaces results in the average bundle diameter of 28.8 ± 5.4 nm and 22.2 ± 3.4 nm in the in the as-spun and the drawn PAN/CNT-A fibers, respectively. These measured bundle diameters include any polymer coating on the surface of the CNTs, as hypothesized previously and shown schematically in Figure 4.4a and Figure 4.4b. This 23% reduction in bundle diameter (from 28.8 to 22.2 nm) can be attributed to CNT de-bundling due to fiber drawing. This de-bundling is in qualitative agreement with the Raman spectroscopy data, which showed enhanced CNT de-bundling upon drawing.
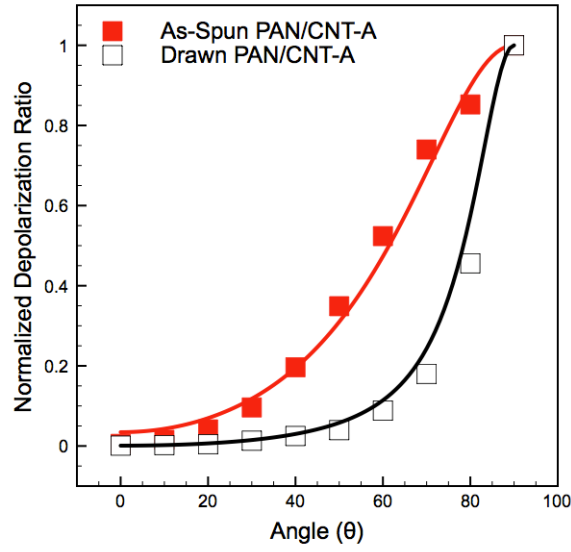
Figure 4.8. Variation of depolarization ratio (R = $I_\perp/I_{//}$) as a function of the angle θ between the polarization direction and the fiber axis in the as-spun and drawn PAN/CNT-A fibers.

4.3.4 Stress transfer in polyacrylonitrile/carbon nanotube fibers

Monitoring the *G'* Raman band shift is useful for determining the strain at which the PAN matrix continues to strain while the CNT is maintained at a constant strain. When the *G'* band peak position plateaus despite additional straining of the macroscopic fiber, it appears as though the PAN-CNT interface is best described as progressive slip where the PAN macromolecules in physical interaction with the CNT surface begin slipping while the tensile load on the CNT remains constant. In the case of drawn PAN/CNT-A, drawn PAN/CNT-B, and drawn PAN/CNT-A(0.1) fibers, the plateau effect occurs at ~0.4% strain. This is further evidence that the presence of the CNTs influence the low strain properties of the nano composite. The interfacial shear strength (τ_i) can be calculated using the modified shear lag equation[142, 143] in a uniaxially aligned fiber composite, provided in Equation 4.7.

$$\tau_i = \frac{nE_f\varepsilon_i}{2}\tanh(ns) \qquad (4.7)$$

103

Where n^2 is defined as $\frac{2G_{13}}{\ln(R/r)E_f}$, E_f is the CNT modulus (Table 4.3), ε_i is the elongation at the PAN-CNT interface. G_{13} is the PAN shear modulus. Based on the shear modulus values for various polymeric fibers, PAN shear modulus is estimated to be about 1.5 GPa[144-146]. s is defined as the ratio (L/r) where L is the length of the CNT and r is the CNT radius, and the ratio R/r is defined by the geometrical spacing of the CNTs, where R is the spacing between neighboring CNTs. A uniform and homogeneous spacing in a square lattice was used to determine the ratio R/r. Due to the fact that $tanh(ns)$ approaches unity as ns approaches a value of 3, $tanh(ns)$ is taken to equal a value of 1 due the computed values of n (~0.1) and the high aspect ratio of the CNTs ($L/d > 1000$) as listed in Table 4.1.
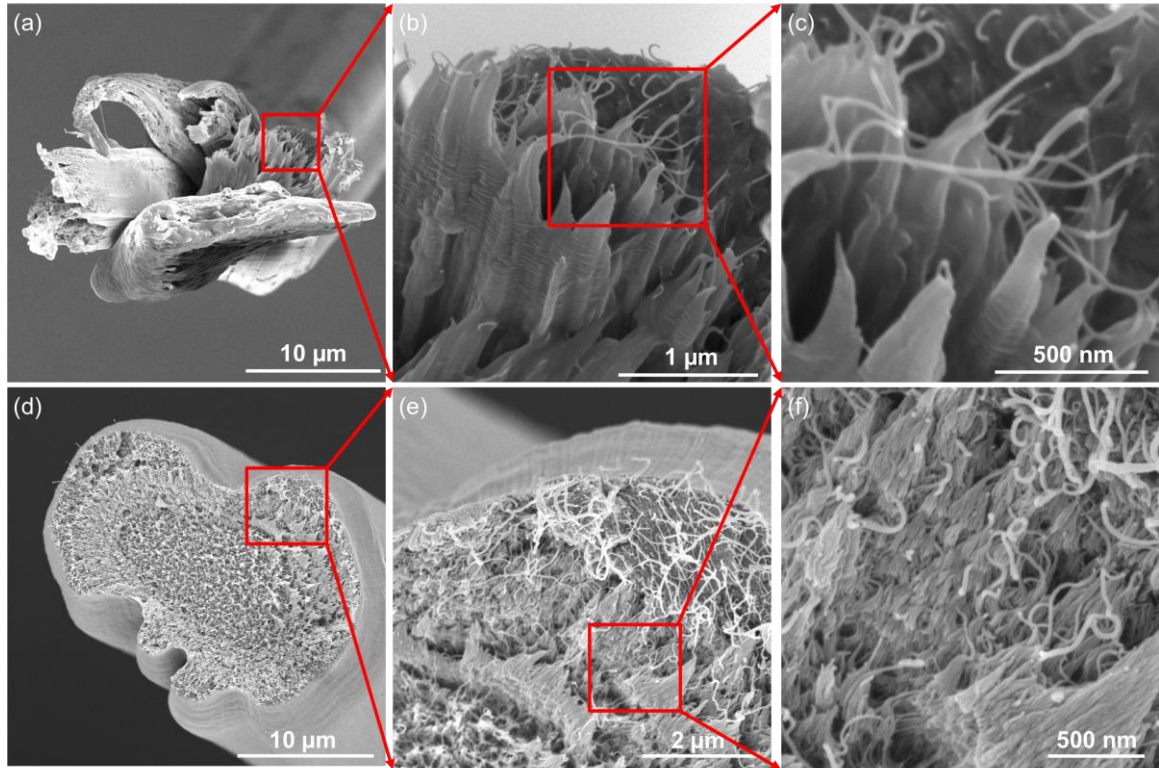
Figure 4.9. SEM images of tensile fractured surfaces of (a) drawn PAN/CNT-A and (b and c) drawn PAN/CNT-A morphology at higher magnification. (d) SEM fracture surface of as-spun PAN/CNT-A fiber and (e and f) its morphology at higher magnification.

In order to overcome this assumption of iso-strain between macroscopic fiber and CNTs, the G' Raman band shift rate of -37.3 cm^{-1}/% strain in individual semiconducting SWNTs[53] is used to determine the strain in the CNT bundles within the composite fibers. Using the S_m of the drawn PAN/CNT-A fiber of -7.3 cm^{-1}, the average strain in the CNTs and at the PAN-CNT interface (ε_i) is determined to be 0.196% through the use of the expression $\varepsilon_i = {S_m}/{-37.3cm^{-1}}$. Using this strain value to calculate the interfacial shear strength in the PAN/CNT-A fiber, τ_i is determined to equal 30.9 MPa. Similarly, the as-spun PAN/CNT-A fiber, which exhibits the G' plateau at a fiber strain of ~1%, exhibits an ε_i of 0.083%, resulting in τ_i = 13.1 MPa. PAN/CNT-B exhibits a S_m of -3.5 cm^{-1}, resulting in an ε_i of 0.094%, and τ_i = 14.6 MPa. Following the same analysis for the PAN/CNT-A(0.1) fiber results in an ε_i of 0.343%, and τ_i = 44.3 MPa.

Interfacial shear strengths determined in the current study are on the lower end of the literature reported values. For polymer/CNT composites, interfacial shear strength values in the range of 2.8 – 500 MPa have been reported in the literature. These literature reported values were determined theoretically using molecular dynamics simulations[39-41] and experimentally using fiber pull out tests[42, 43, 45, 46], Raman spectroscopy[49], and fragmentation tests[48]. CNT fiber pullout tests suggest that the interfacial shear strength between polymer and CNT with polymer repeat units containing aromatic backbone structures (polyetheretherketone (3.5 – 14 MPa)[43] and carbon fiber (32 ± 3 MPa)[47] have lower interfacial shear strengths as compared to those without an aromatic structure in the backbone (polyethylene-butene (~ 15 – 90 MPa)[46] and polymethylmethacrylate (85-372 MPa)[45]). In the case of the polyethylene-butene/CNT composites, the τ_{max} determined by fiber pullout testes was found to be dependent upon the diameter of the CNT, where CNTs with an average diameter of 10-20, 30 – 40, 40-50, and 60-70

nm having τ_{max} of $\sim 90 \pm 40$, $\sim 20 \pm 40$, $\sim 40 \pm 20$, and $\sim 15 \pm 5$ MPa, respectively[46]. Similarly, in PMMA/CNT fiber pullout tests, τ_{max} was found to be dependent upon the outer diameter of the double wall carbon nanotube (DWNT) where the DWNTs with a diameter of 2.0, 3.1, and 4.2 nm had a $\tau_{max} = 372 \pm 65$, 155 ± 27, and 85 ± 14 MPa, respectively[45]. Taking into account that the interfacial interaction between polymer and CNT is dependent upon a multitude of factors including but not limited to the polymer and CNT type used in the formation of the composite, the degree of aggregation of the CNT and its aspect ratio in the exfoliated or bundled state, covalent or non-covalent bonding of the CNT to the matrix, and type and degree of functionalization of the CNT, the direct comparison of interfacial shear strength between different systems has not yet been fully realized. Initial studies on the effect of polymer chain grafting to the CNT surface in poly(ether ketone)/carbon nanotube composites, and its influence on the interfacial interactions are investigated in Appendix A.

4.4 Conclusions

PAN/CNT gel-spun composite fibers were characterized through Raman spectroscopy by monitoring the stress induced G' Raman band shift during tensile deformation. CNT purity, perfection, and aspect ratio was shown to have a significant effect on the G' Raman band shift during strain and on the compliance corrected tensile modulus. Addition of 1 wt% CNT-A led to a 12% and 16% increase in compliance corrected modulus in the as-spun and drawn PAN/CNT-A fibers as compared to the similarly processed as-spun and drawn PAN fibers without CNT. Improved CNT dispersion enhances stress transfer efficiency as monitored by stress induced G' Raman band shift. It is shown that fiber drawing increases the Raman shift rate (S_r), and the maximum Raman G' band shift. The PAN/CNT interface undergoes progressive slip at a higher macroscopic fiber strain in the as-spun fiber as compared to the fully drawn fiber. The

interfacial shear stress increases as the fiber is drawn, despite the reduced macrscopic fiber strain at which the PAN/CNT interface begins to progressively slip, further supporting the notion that stress transfer from the matrix to the CNT is promoted by the fiber drawing.

Chapter 5

HIGH RESOLUTION TRANSMISSION ELECTRON MICROSCOPE STUDY ON POLYACRYLONITRILE /CARBON NANOTUBE BASED CARBON FIBERS AND THE EFFECT OF STRUCTURE DEVELOPMENT ON THE THERMAL AND ELECTRICAL CONDUCTIVITIES

5.1 Introduction

It has been demonstrated that carbon nanotubes (CNTs) act as a nucleating agent for polymer crystallization. This behavior has been observed for many different polymer/CNT composites where the polymers were polyethylene[147], polypropylene[148], nylon[149], poly(ethylene terephthalate)[150], poly(vinyl alcohol)[151], and polyacrylonitrile (PAN)[25, 132]. Coupled with the capability of nucleating behavior, CNTs have also been shown to act as templating agents for polymer orientation. Previous investigations have reported that when processed under shear flow, polymer molecules in the vicinity of CNTs can form a highly ordered interphase region (e.g. oriented crystal structure)[147].

Among various polymers, PAN is of significant interest due to its predominance as a precursor for carbon fiber manufacturing [1, 74]. Carbon fiber is a unique material to the extent that the material properties span a wide range of thermo-physical properties that can be tailored to the desired application, allowing for a vast range of material properties. By increasing the final heat treatment temperature of PAN based carbon fibers, increases in tensile modulus, electrical conductivity, and thermal conductivity have been observed[152, 153]. This is due to the increasing graphitic structure order in the fiber as the carbonization/graphitization temperature is increased, resulting in commercially available PAN based carbon fiber with tensile modulus ranging from 230 to 588 GPa, electrical conductivities of 55-143 kS/m, and thermal conductivities of 5 to 152 W/m/K[74, 154, 155]. However, improvements in tensile modulus, and electrical and thermal

conductivity typically are achieved at the expense of tensile and compressive strength due to the large crystal grain formation of the graphitic structure. Fibers such as high modulus Toray M60J possess a tensile strength of 3.9 GPa, compressive strength of 1.0 GPa[156], tensile modulus of 588 GPa, thermal conductivity of 0.363 cal/cm/s/°C (152 W/m/K), and electrical conductivity of 143 kS/m[154]. In comparison, intermediate modulus Toray T800H possesses a tensile strength of 5.5 GPa, compressive strength of 2.3 GPa[156], tensile modulus of 294 GPa, thermal conductivity of 35 W/m/K, and electrical conductivity of 71 kS/m[157].

Experimental PAN/CNT based carbon fibers have shown promising mechanical properties, with tensile strength of 3.2 - 5.5 GPa (max single filament test: 7.3 GPa) and tensile modulus of 253 - 463 GPa[103-105, 113]. It has been shown that both graphitic and turbostratic graphitic structures can be developed at relatively low carbonization temperatures (800 − 1300 °C)[47, 103, 104, 113, 158], which is about 1000 °C lower than the temperature required for the graphitic structure formation of PAN based carbon fiber[1]. The highly ordered graphitic structure developed within the turbostratic graphitic matrix is expected to improve the transport properties (electrical and thermal conductivities) of the PAN/CNT based carbon fibers as compared to the traditional PAN based carbon fibers.

The thermal conductivity of PAN based carbon fibers is directly related to the concentration of point defects consisting of vacancies, interstitial atoms, and impurities, as well as the crystalline perfection and orientation. As the carbonization or graphitization heat treatment temperature is increased, the concentration of point defects is reduced and the crystalline perfection increases, thereby resulting in an improved thermal conductivity. Increasing the heat treatment temperature of a PAN based carbon fiber from 1500-2100 °C resulted in a thermal conductivity increase of 20.2 to 69.3 W/m/K[153], or over 350%. Other methods of increasing

PAN based carbon fiber thermal conductivity include the growth of CNTs on the surface of commercial carbon fibers, such as PAN based T1000GB (Toray) and pitch based K13D (Mitsubishi). The thermal conductivity of T1000GB increased 47%, from 12.6 to 18.6 W/m/K following CNT grafting onto the carbon fiber surface[159].

It is well understood that the thermal conductivity in carbon fibers occurs through electron and phonon contributions. The electron contribution at room temperature is known to be ~0.40 – 0.66 W/m/K[160, 161], which is ~10% of the reported thermal conductivity of commercial fibers such as IM7 (5.4 W/m/K)[155]. This suggests that the thermal conductivity of PAN based carbon fibers is largely due to phonon contributions. The thermal conductivity of CNTs is also a phonon dominated process which is dependent upon CNT length[162, 163], diameter[164, 165], purity[163], and degree of functionalization[166]. As described by the Debye equation[167], the lattice thermal conductivity is dependent upon the phonon relaxation time, specific heat, and phonon group velocity. Due to the estimated phonon mean free path (100 nm – 1 µm) in SWNTs, the thermal conductivity will be dependent upon the length of the SWNT, where SWNTs with lengths shorter than a few µm will exhibit ballistic behavior[168]. Measurements on individual MWNTs indicate that the thermal conductivity increases as the number of walls decreases, which has been attributed to the interactions of phonons and electrons between the MWNT walls, and that as the diameter (number of walls) increases so do the phonon and electron interactions which reduces the thermal conductivity[165]. Similarly, the thermal conductivity is also diameter dependent for SWNTs due to the lower probability for Umklapp scattering for smaller diameter tubes, as well as evidence that the phonon group velocity increases as the SWNT diameter decreases[169]. Maximum thermal conductivity in MWNTs (~3000 W/m/K) was measured at ~320 K[170], ~200 K higher temperature than that observed in highly ordered pyrolytic graphite (HOPG)[171]. It was

also observed that the thermal conductivities of MWNT mats[172] and aligned SWNT rope films[173] are much lower than those of individual MWNTs[170] and SWNTs[167, 174], indicating that tube-tube contact thermal resistance[175] greatly reduces the thermal conductivity in CNT bundles. The thermal conductivities of polymer/CNT composites are also strongly dependent on the type of the CNT (e.g., SWNT or MWNT), the CNT length[176], CNT purity[177, 178], quality of CNT dispersion[179], and on the type and degree of functionalization of the CNT[176].

Electrical conductivity enhancement in polymer/CNT nanocomposites is well understood from percolation theory[180]. CNT alignment can be detrimental to electrical conductivity enhancement in polymer/CNT composites due to the inability of the CNTs to efficiently form a percolation network [181-185]. With electrical conductivities on the order of $\sim 10^4$ - 10^5 S/m, PAN based carbon fibers provide an electrically conducting matrix that surrounds the highly conducting CNTs such that increases in electrical conductivity are expected at low CNT volume fractions of CNTs despite the high degree of CNT orientation within the anisotropic carbon fiber.

In this investigation, the microstructure development of PAN and PAN/CNT based carbon fibers was investigated by HR-TEM and wide-angle x-ray diffraction (WAXD). The electrical, thermal, and mechanical properties of PAN and PAN/CNT based carbon fibers are correlated with the microstructure. Commercial PAN based carbon fibers, T300 and IM7 are also studied for comparison.

5.2 Experimental

5.2.1 Materials and fiber processing

Poly(acrylonitrile-co-methacrylic acid) (PAN-co-MAA, MAA content=4 wt%) with viscosity average molecular weights of 453,000 g/mol, 513,000 g/mol, and 964,000 g/mol were

obtained from Japan Exlan (Osaka, Japan). Three different types of CNTs (CNT-A, CNT-B, and CNT-C) were obtained from Continental Carbon Nanotechnologies, Inc. (Lot # XOC231U), Unidym, Inc. (Lot # XO122UA), and SouthWest Nanotechnology (SMW200), respectively. Average diameter (2.7, 3.0, and 12.1 nm) and number of walls (3.0, 3.0, and 10.5) were determined by TEM and CNT impurity content (1.1, 3.3, and 2.3 wt%) by TGA for CNT-A, CNT-B, and CNT-C, respectively. For polymer solution and CNT dispersion, *N,N*-dimethylformamide (DMF) was used after distillation.

For control PAN solution, the polymer was dissolved in DMF at 90 $^{\circ}$C for 2 h. Four different PAN/CNT composite solutions (PAN/CNT-A (0.42 wt%), PAN/CNT-A (1 wt%), PAN/CNT-B (0.5 wt%), and PAN/CNT-C (0.5 wt%)) were prepared as described elsewhere[186]. The solid concentration for all solutions was 10.5 g/dL. For PAN/CNT-A and PAN/CNT-C solutions, copolymer with a viscosity average molecular weight of 513,000 g/mol was used, while PAN/CNT-B solution was prepared using a mixture of two copolymers (453,000 and 964,000 g/mol). The weight fraction of high molecular weight PAN-co-MAA (964,000 g/mol) was 15 wt% and that of the low molecular weight PAN-co-MAA (453,000 g/mol) was 85 wt%.

PAN and PAN/CNT precursor fibers were gel spun as a 100 filament tow using laboratory scale multi-filament fiber spinning machine (Hills Inc., Melbourne, FL). The flow rate for fiber spinning was maintained at 0.5 cc/min/hole and the gelation medium was -50 $^{\circ}$C methanol for all GT PAN and GT PAN/CNT fibers, with the exception of the GT PAN/CNT-B fibers, which utilized a room temperature methanol coagulation. The as-spun draw ratio was 3 and the post-spin draw ratio was as high as 13. The post-spin drawing was conducted using a multi-step drawing process and the drawing temperature was as high as 185 $^{\circ}$C. The 100 filament tow precursor fibers were subsequently stabilized and carbonized using continuous carbonization

equipment (Harper International Co, Buffalo, NY). The stabilization and carbonization temperatures were as high as 310 ºC and 1450 ºC, respectively. Sample designation of the final processed gel spun PAN based carbon fiber is GT PAN. It should be noted that the GT PAN carbon fiber presented is distinct from other recent publications[187]. For the composite carbon fibers, GT PAN/CNT-A (0.42 wt%) and GT PAN/CNT-A (1.0 wt%) were processed from two distinct precursor fibers. The GT PAN/CNT-B1 (0.5 wt%) and GT PAN/CNT-B2 (0.5 wt%) carbon fibers were processed from the same precursor fiber. Differences in temperature profiles and applied strain during stabilization and carbonization contributed to the manufacture of two distinct carbon fibers, GT PAN/CNT-B1 (0.5 wt%) and GT PAN/CNT-B2 (0.5 wt%), from the same precursor fiber. GT PAN/CNT-C (0.5 wt%) was processed from multi-wall carbon nanotube (SMW200 MWNT) containing precursor fiber.

5.2.2 Characterization

Single filament tensile testing was performed using a FAVIMAT+ tensile testing instrument with a 25.4 mm gauge length, at a strain rate of 0.1 %/s. Fiber linear density was measured on each tensile specimen using the inline vibroscope on the FAVIMAT+. WAXD was conducted on 200 filament bundles using previously described methods[25]. Scanning electron microscopy (SEM) was performed on a Zeiss Ultra 60 FE-SEM at an accelerating voltage of 2 keV. HR-TEM was performed on a FEI Tecnai F30 at an accelerating voltage of 80 keV. Samples were prepared for observation by HR-TEM on a FEI NOVA Nanolab 200 focused ion beam (FIB)/SEM. Individual fiber samples were mounted perpendicularly to the surface of Copper 3-Post Omniprobe grids (Electron Microscopy Sciences) using Epo-Tek 353ND epoxy (Gatan, Inc.). Samples were then FIB thinned using gallium ions at 30 keV followed by a low energy polish at 5 keV. Thermal and electrical conductivity measurements were performed on

individual carbon fibers using a DC Thermal Bridge Method (DCTBM) described previously[188] and standard four-probe approach, respectively. Three filaments were tested using the DCTBM approach to ensure accuracy and the values were averaged to obtain the thermal and electrical conductivity values. Appendix B provides the thermogravimetric analysis (TGA) data of commercial IM7 carbon fiber and gel spun PAN and PAN/CNT carbon fibers and Appendix C provides the Raman spectra of the commercial IM7 and T300 carbon fibers, as well as a gel spun PAN and PAN/CNT based carbon fiber.

5.3 Results and Discussion

5.3.1 Structure development of the PAN and PAN/CNT based carbon fibers

HR-TEM micrographs of the transverse cross-section of PAN based carbon fibers are shown in Figure 5.1 For comparison, those of commercial carbon fibers (T300 and IM7) are shown in Figure 5.1a and 5.1b, respectively. T300 (Figure 5.1a1 and 5.1a2) shows a random crystallite orientation with smaller crystallites in the lateral direction as compared to the larger and oriented crystallites of IM7 (Figure 5.1b1 and 5.11b2). WAXD analysis results showed that T300 has a lateral crystal size (L_{002}) of 1.4 nm, which is marginally smaller than those of 1.6 nm for IM7 and the GT PAN based carbon fibers (Table 5.1). T300 exhibits a core of ~2.7 μm in diameter, and a surrounding radial sheath ~2.2 μm wide, which can be observed from the FIB thinned section by SEM in Figure 5.1a3, and has been observed using other techniques[189, 190]. Differences in internal structure between the T300 sheath (Figure 5.1a1) and core (Figure 5.1a2) were observed by HR-TEM. Similar FIB thinning of the gel spun GT PAN based carbon fiber in Figure 5.1c3 does not show the same sheath-core structure, but a uniform structure throughout the fiber cross-section. The hole in Figure 5.1c3 is due to preferential thinning of the fiber in that area during sample preparation and is not an internal defect.
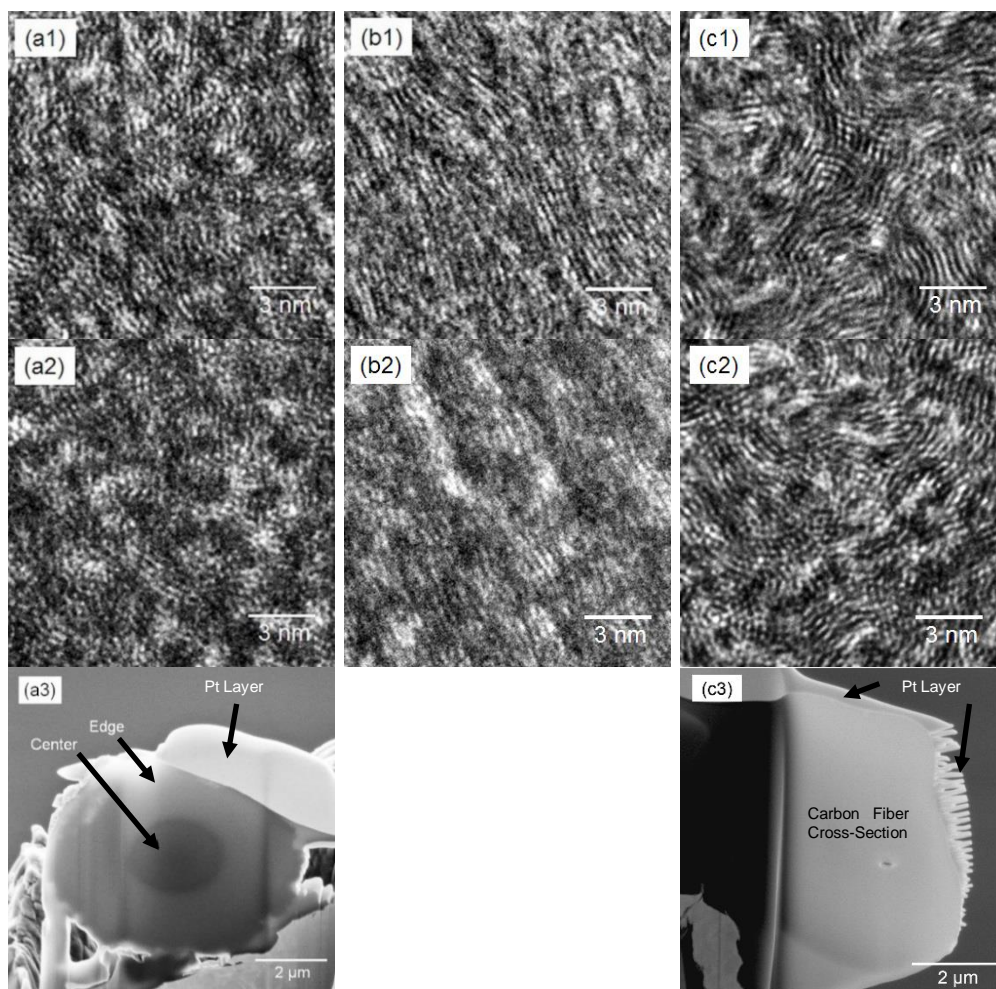
Figure 5.1 HR-TEM transverse cross-section (fiber axis into and out of page) images of (a1 and a2) T300, (b1 and b2) IM7, and (c1 and c2) GT PAN carbon fiber. The images of (a1), (b1), and (c1) are from fiber edge and those of (a2), (b2), and (c2) are from fiber center. SEM image of FIB milled fiber cross-section showing the distinct sheath-core morphology in (a3) T300 and the homogeneous morphology of (c3) GT PAN carbon fiber.

Structural parameters determined by WAXD for the gel spun GT PAN and PAN/CNT based carbon fibers and of the commercial T300 and IM7 carbon fibers are presented in Table 5.1. As noted earlier, the L_{002} and L_{10} crystal sizes of the GT PAN based carbon fiber are slightly larger than that of the T300 carbon fiber. In addition, the gel spun PAN/CNT based carbon fibers also showed similar structural parameters as compared to those of the GT PAN based carbon fiber. However, orientation characterization of the GT PAN and PAN/CNT based carbon fiber

exhibits differences in the azimuthal scans of the *2θ ~25º* peak, which can be fitted to a single curve in the case of the PAN based carbon fiber, and can be de-convoluted into two peaks in the GT PAN/CNT-A and GT PAN/CNT-B based carbon fiber as described elsewhere[104, 113]. De-convoluting the two peaks of the azimuthal scan allows for the area fraction of the two peaks to be determined, which can be used as an estimate of the volume fraction of the two regions corresponding to the turbostratic matrix and the highly ordered graphitic region as shown in Figure 5.2. In addition, the orientation factors of both the turbostratic matrix ($f_{002,matrix}$) and the highly ordered (HO) graphitic region ($f_{002,HO}$) can be determined, and are presented in Table 5.1. It is interesting to note the high level of orientation associated with the highly ordered graphitic region in the GT PAN/CNT-A and GT PAN/CNT-B based carbon fibers, with $f_{002, HO} \geq 0.97$. It is also interesting that PAN/CNT-C (0.5 wt%) exhibits an azimuthal scan similar to that of the control GT PAN carbon fiber. Considering that CNT-C is best described as a MWNT (average number of walls = 10.5), and CNT-A and CNT-B are considered FWNTs (average number of walls = 2.6), it can be surmised that the presence of the HO region in the azimuthal scan is associated only with the templated graphitic region and not from the repeat crystallographic planes of the CNT walls. Therefore, due to the absence of the second peak in the azimuthal scan of GT PAN/CNT-C (0.5 wt%) and its presence in the GT PAN/CNT-A (0.5 wt%) and GT PAN/CNT-B carbon fibers, it can be concluded that the carbon fibers produced with CNT-A and CNT-B exhibit graphitic templating behavior.

Table 5.1 Structural parameters of the GT PAN and PAN/CNT based carbon fibers. Structural parameters of the commercial PAN based carbon fibers are also listed for comparison.

	T300	IM7	GT PAN	GT PAN/CNT-A (0.42 wt%)	GT PAN/CNT-A (1 wt%)	GT PAN/CNT-B1 (0.5 wt%)	GT PAN/CNT-B2 (0.5wt%)	GT PAN/CNT-C (0.5wt%)
$f_{002,matrix}$	0.77	0.83	0.86	0.87	0.86	0.83	0.87	0.86
$f_{002, HO}$	-	-	-	0.98 (1.4)*	0.97 (2.0)*	0.99 (0.7)*	0.99 (0.9)	-
FWHM $_\#$	35.0	30.2	28.1	26.5	29.6	31.5	26.5	26.3
$d_{(002)}$ (nm)	0.349	0.348	0.347	0.346	0.347	0.349	0.346	0.347
$L_{(002)}$ (nm)	1.4	1.6	1.6	1.7	1.6	1.5	1.8	1.7
$L_{(10)}$ (nm)	2.0	2.1	2.5	2.5	2.2	2.0	2.1	2.3

* Values in parenthesis indicate the volume fraction of the HO graphitic region as determined through peak deconvolution of the $2\theta \sim 25°$ azimuthal scan.
[#] FWHM of the $2\theta \sim 25°$ azimuthal peak.
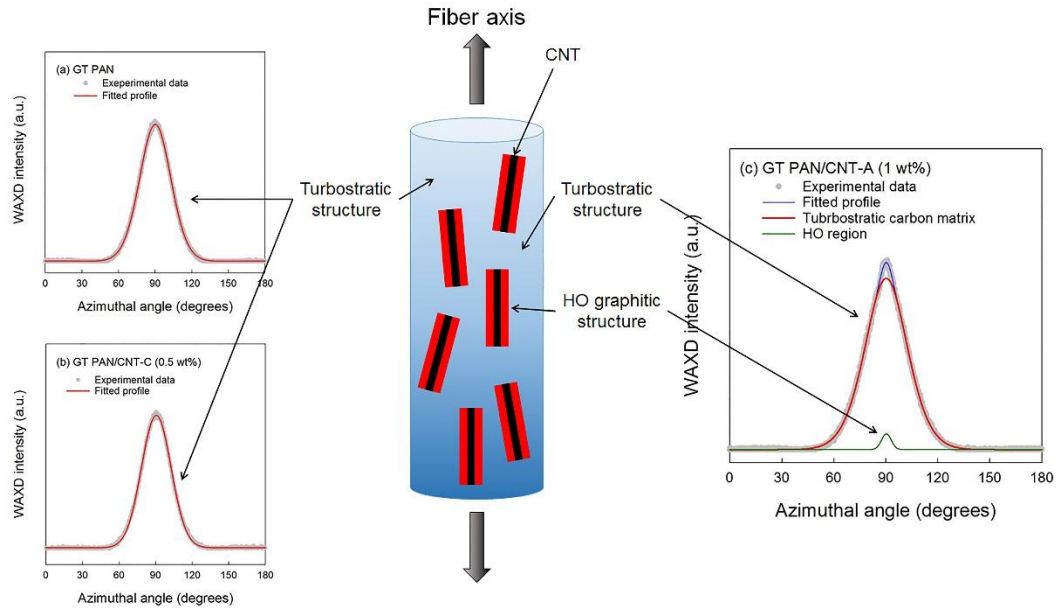
Figure 5.2 Azimuthal scans of the gel spun (a) GT PAN, (b) GT PAN/CNT-C (0.5 wt%) and (c) GT PAN/CNT-A (1.0 wt%) fibers. The azimuthal scans of (a) and (b) can be fitted using a single fitting curve while (c) is fitted with two curves. The additional fitting curve in (c) is attributed to the highly ordered region formed by the CNT and the CNT graphitic template region. Schematic description of the carbon fibers is also shown to illustrate the turbostratic carbon matrix, templated graphitic structure, and CNTs.

In contrast to the turbostratic crystallites observed in the PAN based carbon fibers, a highly ordered graphitic region is observed surrounding the CNTs and CNT bundles in the PAN/CNT based carbon fibers as shown in Figure 5.3. Given that the CNTs used in this study have an average diameter of 2.7 and 3.0 nm for CNT-A and CNT-B, respectively, and both have an average number of walls of 2.6[186], the CNT templated graphitic structure can be directly observed. In the case of GT PAN/CNT-B1 (0.5 wt%) as many as 12-14 graphitic layers are developed beyond the CNT bundle structure as shown in Figure 5.3b1 and 5.3b2, which can be used to depict the formation and growth of the CNT templated graphitic structure. In the right half of Figure 5.3b2, three distinct CNTs can be observed on the side of the CNT bundle. Considering that the number of walls for the individual CNTs is 2.6, it can be estimated that the concentrically template graphitic structure contains ~9-11 graphitic layers. As the templated graphitic structure from the surface of each CNT begins to grow and form increasing concentric layers, its associated templated graphitic structures begin to impinge upon the neighboring CNT's templated graphitic structure. As this occurs, the templated graphitic structure on each individual CNT begins to form a continuous graphitic structure that begins to envelope the CNTs. It can also be noted that, as the CNT bundle increases in size (greater number of CNTs within the bundle), the available surface area for templated growth begins to diminish, and if CNTs are aggregated, graphitic templating is not possible due to the lack of PAN molecules separating the CNTs prior to stabilization and carbonization. This signifies the importance of the individualized and exfoliated CNTs within the precursor fiber so that maximum surface area interaction can occur between the CNT surface and the PAN matrix prior to carbonization and formation of the graphitic CNT templated structure.
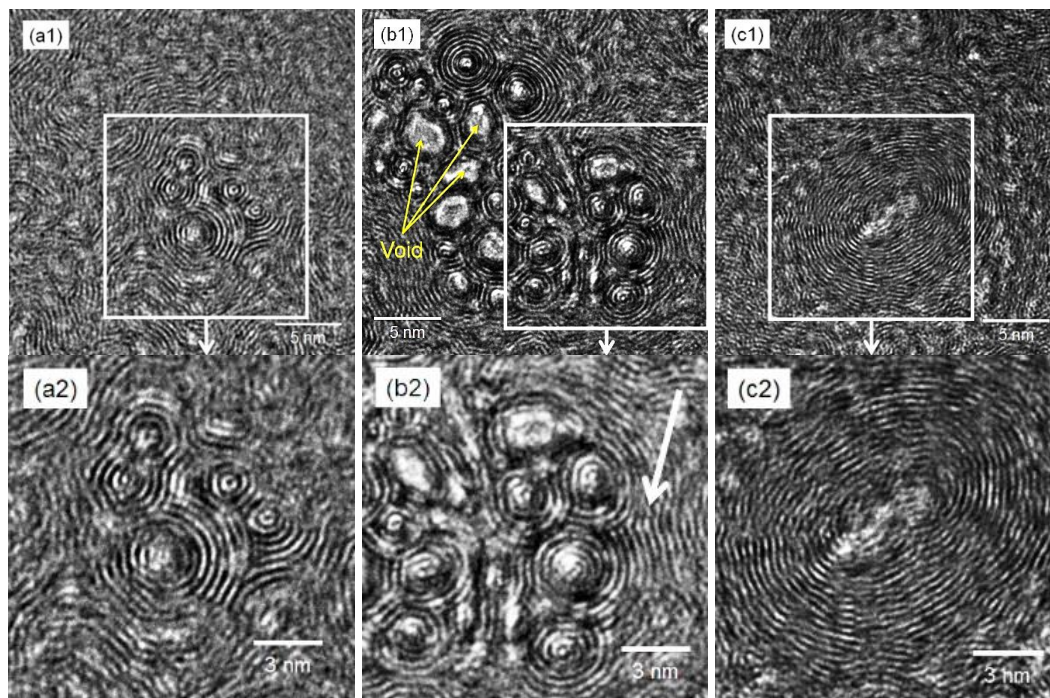
Figure 5.3 HR-TEM transverse cross-sectional images of (a1 and a2) the GT PAN/CNT-A (0.42 wt%), (b1 and b2) the GT PAN/CNT-B1 (0.5 wt%), and (c1 and c2) the GT PAN/CNT-C (0.5 wt%). The arrow in (b2) shows the evidence of graphitic templating and epitaxial growth at the outside most surface of the CNT bundle.

5.3.2 Thermal conductivity of the PAN and PAN/CNT based carbon fibers

The PAN and PAN/CNT based carbon fibers exhibited higher room temperature thermal conductivities than the commercially available T300 and IM7 carbon fibers during single filament testing using the DCTBM as shown in Table 5.2. T300 and IM7 carbon fibers have reported room temperature thermal conductivities of 0.025 cal/s-cm-°C (10.5 W/m/K) and 3.12 Btu/hr-ft-°F (5.4 W/m/K), respectively[155, 191]. Using the DCTBM, room temperature thermal conductivities of 13.6 W/m/K and 16.5 W/m/K were measured for T300 and IM7 carbon fibers (Table 5.2). The DCTBM used has an experimental uncertainty of ±11%[188], while the thermal conductivity measurement methods of T300 and IM7 are not explicitly outlined by the manufacturers. Single filament thermal conductivity experiments of high strength PAN based carbon fiber (Toray T1000GB) using an AC modified calorimetry method measured a thermal

conductivity of 12.6 W/m/K[159]. Compared to the value reported by Toray (32.1 W/m/K)[192], differences in thermal conductivity values exist and are dependent upon the testing procedure.

The GT PAN carbon fiber exhibits a room temperature thermal conductivity of 20.0 W/m/K using the DCTBM, a 47% and 21% increase as compared to T300 and IM7, respectively. The GT PAN/CNT-A (1.0 wt%) carbon fiber exhibits the highest room temperature thermal conductivity measured at 33.5 W/m/K. Considering the similar processing conditions of the PAN and PAN/CNT based carbon fibers, increases in PAN/CNT based carbon fiber over PAN based carbon fiber thermal conductivity can be attributed to the inclusion of the CNTs and their influence on the carbon structure, resulting in the graphitic templated region as observed by the TEM study. Figure 5.4a shows the thermal conductivity of various PAN and PAN/CNT based carbon fibers as a function of temperature. Thermal conductivity increases as a function of temperature for all the fibers, which is expected for the turbostratic structure formed in PAN based carbon fiber[193]. To understand the effect of the CNTs and the templated graphitic structure within the PAN/CNT based carbon fibers, the thermal conductivity enhancement at ~295K is shown in Figure 5.4b. The thermal conductivity enhancement is described by the relationship k/k_m where k is the thermal conductivity of the gel spun PAN/CNT based carbon fiber and k_m is the thermal conductivity of the gel spun PAN based carbon fiber. In all cases, the thermal conductivity is increased with the addition of CNTs.

Table 5.2 Thermal and electrical conductivity of the PAN and PAN/CNT based carbon fibers at ~295K as determined by the DCTBM. Tensile properties as determined by individual filament testing at 25.4 mm gauge length.

	T300	IM7	GT PAN	GT PAN/CNT-A (0.42 wt%)	GT PAN/CNT-A (1 wt%)	GT PAN/CNT-B1 (0.5 wt%)	GT PAN/CNT-B2 (0.5 wt%)	GT PAN/CNT-C (0.5 wt%)
Thermal conductivity (W/m/K) at 295 K	13.6 (10.5) [‡]	16.5 (5.4) [‡]	20.0	23.7	33.5	31.0	Not measured	Not measured
Electrical conductivity (kS/m) at 295 K	54.0 (58.8) [‡]	59.6 (66.7) [‡]	61.3	74.2	70.0	63.6	Not measured	Not measured
Diameter (μm)	6.8 ± 0.2 (7) [‡]	5.2 ± 0.2 (5.2) [‡]	4.9 ± 0.3	5.7 ± 0.3	6.2 ± 0.5	5.2 ± 0.4	4.9 ± 0.2	6.1 ± 0.4
Tensile strength (GPa)*	3.6 ± 0.4 (3.5) [‡]	5.5 ± 0.8 (5.5-5.7) [‡]	4.2 ± 1.0	3.2 ± 0.8	2.0 ± 0.4	3.1 ± 0.8	3.1 ± 0.8	4.0 ± 0.9
Compliance corrected tensile modulus (GPa)**	229 (230) [‡]	281 (276) [‡]	333	342	318	273	359	341

* Tensile properties are measured at 1 inch gauge length.
** Compliance corrected tensile moduli are obtained by testing fibers at various gauge length as described elsewhere[194].
‡ The values in parenthesis are manufacturer reported data.
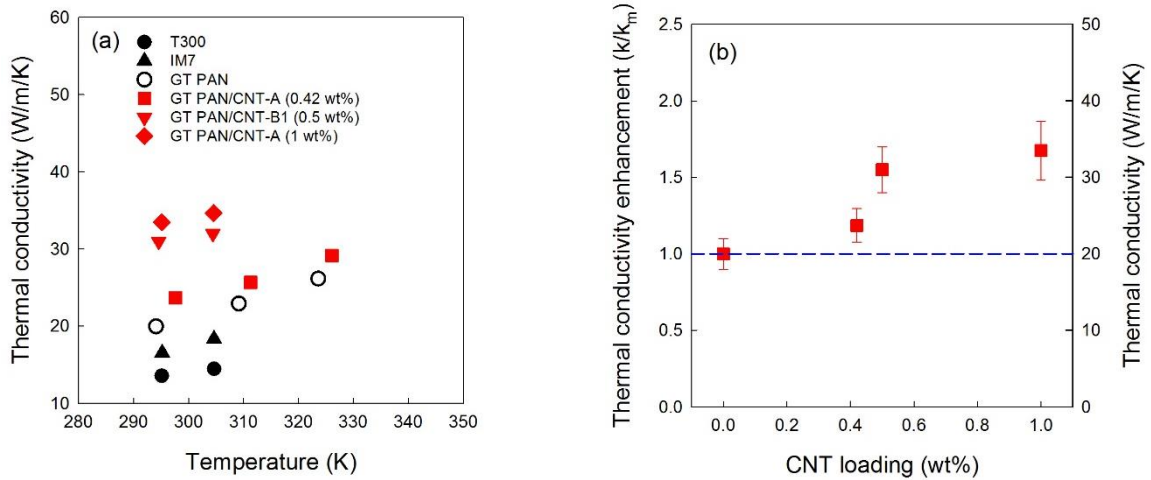
Figure 5.4(a) Thermal conductivities of various carbon fibers as a function of temperature and (b) thermal conductivity enhancement in the PAN/CNT based carbon fibers. The km is the thermal conductivity of the GT PAN based carbon fiber. All thermal conductivity values were measured using DCTBM.

The thermal conductivity of the PAN/CNT based carbon fibers can be affected by both the presence of CNT and the formation of the highly ordered graphitic structure in the vicinity of

CNTs. Due to the high thermal conductivity of CNTs (3000 - 3500 W/m/K) and HOPG (2000 W/m/K) at room temperature as compared to the thermal conductivity of the PAN based carbon fibers (T300 – 13.6 W/m/K, IM7 – 16.5 W/m/K), even a relatively low amount of CNTs which exhibit strong graphitic interphase formation will enhance the thermal conductivity as compared to PAN based carbon fibers without CNTs or a graphitic interphase. Using the curve fitting data of the WAXD azimuthal scans shown in Figure 5.2, the thermal conductivity of the highly ordered graphitic region perpendicular ($K_\perp$) and parallel ($K_\parallel$) to the fiber direction can be determined using Equations 5.1 and 5.2, respectively[171].

$$K_\perp = K_a \left[1 - \left(1 - \frac{K_c}{K_a} \right) \langle cos^2\phi \rangle \right] \tag{5.1}$$

$$K_\parallel = K_a \left[1 - \left(1 - \frac{K_c}{K_a} \right) \langle sin^2\phi cos^2\phi \rangle \right] \tag{5.2}$$

Where K_a is the thermal conductivity along the fiber axis (perpendicular to the graphitic (002) plane), K_c is the thermal conductivity perpendicular to the fiber axis (parallel to the graphitic (002) plane), and ϕ is the angle between the c-axis ((002) direction) and the fiber axis.

Since the highly ordered graphitic region in the vicinity of CNTs is assumed to possess similar structure to pyrolytic graphite[195], here we assumed K_a of 1950 W/m/K and K_c of 5.7 W/m/k. The calculated thermal conductivities ($K_\parallel$) of the templated graphitic regions are listed in Table 5.3. In a similar fashion, the thermal conductivity of the graphitic region can also be predicted from the full width at half maximum (FWHM) intensity of the highly ordered graphitic region from the WAXD azimuthal scan. Using the relationship put forward by Bacon[196], where $I(\phi) \sim cos^m\phi$, where the higher the value of m the greater the orientation of the graphitic structure, and the relationship of Fischbach[197], $\beta \sim 1.18m^{-1/2}$, where β (in radians) is the FWHM of the

azimuthal scan, Equations 5.3 and 5.4 can be used to determine the thermal conductivity of the bulk graphite based upon the crystal orientation. The calculated thermal conductivities ($K_{\parallel}$) of the templated graphitic regions are also listed in Table 5.3.

Table 5.3 FWHM of the highly ordered (HO) region determined by WAXD azimuthal scans and the corresponding volume fraction of the HO region in parenthesis. Bacon's constant m is also used to quantify the orientation of the HO region. The thermal conductivities of the HO region were calculated using Equations 5.2 and 5.4.

	FWHM$_{azimuthal}$ of HO region	Bacon's constant m of HO region	$K_{\parallel}$ (W/m/K) by eq. 5.2	$K_{\parallel}$ (W/m/K) by eq. 5.4
GT PAN/CNT-A (0.42 wt%)	6.3 (1.4%)	82	1939	1927
GT PAN/CNT-B1 (0.5 wt%)	5.6 (0.7%)	145	1946	1937
GT PAN/CNT-A (1 wt%)	7.9 (2.0%)	73	1945	1924

$$K_{\perp} = K_a \left[1 - \left(1 - \frac{K_c}{K_a} \right) \left(\frac{m+1}{m+3} \right) \right] \qquad (5.3)$$

$$K_{\parallel} = K_a \left[1 - \left(1 - \frac{K_c}{K_a} \right) \left(\frac{1}{m+3} \right) \right] \qquad (5.4)$$

The thermal conductivities of PAN/CNT based carbon fibers can be approximated based on the measured thermal conductivity of the PAN based carbon fiber and the volume fraction of the HO regions determined from WAXD analysis. Using the parallel and series models to predict the thermal conductivities of the PAN/CNT based carbon fibers (Equations 5.5 and 5.6, respectively), the upper and lower bounds of the theoretical thermal conductivities of the PAN/CNT carbon fibers (k_c) are calculated and listed in Table 5.4.

$$k_c = k_p V_p + k_m V_m \qquad (5.5)$$

$$k_c = \frac{1}{\left(\left(\frac{V_m}{k_m} \right) + \left(\frac{V_p}{k_p} \right) \right)} \qquad (5.6)$$

where, k_p is the thermal conductivity of the highly graphitic region, V_p is the volume fraction of the highly graphitic region, k_m is the thermal conductivity of the turbostratic carbon fiber, and V_m is the volume fraction of the turbostratic carbon fiber.

It has been reported that the thermal conductivity (k) in polymer/CNT composites typically falls between the series and the parallel thermal conductivity approximations, but typically nearer the series model[198]. In the current study, it was also observed that the calculated thermal conductivities are between these models, suggesting that the measured values are valid. Discrepancies between the experimental data and the two predicting models can be attributed to the models not accounting for thermal resistance at the boundary between the turbostratic matrix and the CNT, turbostratic matrix and the graphitic interphase, CNT and the graphitic interphase, and CNT-CNT overlap and contact resistance. Defects inherent to the fibers are not taken into account in either the series or the parallel model. These defects can create phonon scattering, which is not accounted for using either of the two models. The HR-TEM image in Figure 5.3b1 is an example of the voids that can exist within the CNT bundles of the PAN/CNT based carbon fiber. These voids are not seen in the GT PAN carbon fiber since the CNT and CNT bundles are not present to form these voids, which will be discussed later.

Table 5.4 Predicted thermal conductivity of the PAN/CNT based carbon fibers using the parallel and series models.

	k_c (Series Model) (W/m/K)	k_c (measured) (W/m/K)	k_c (Parallel Model) (W/m/K)
GT PAN/CNT-A (0.42 wt%)	20.3	23.7	46.7
GT PAN/CNT-B1 (0.5 wt%)	20.1	31.0	33.4
GT PAN/CNT-A (1.0 wt%)	20.4	33.5	58.0

5.3.3 Electrical conductivity of the PAN and PAN/CNT based carbon fibers

Generally, the electrical conductivity of PAN based carbon fiber scales with its tensile modulus[74]. As crystallite orientation increases so does tensile modulus. The improved orientation results in greater electron mobility along the fiber axis, resulting in an improved electrical conductivity. Figure 5.5a plots the electrical conductivities of various carbon fibers as a function of their tensile modulus. It appears that the PAN based carbon fibers follow a linear trend and the PAN/CNT based carbon fibers follow their own linear trend, with enhanced electrical conductivities despite similar tensile moduli. Considering that the electrical conductivity in PAN based carbon fibers can be diminished by the presence of defects such as grain boundaries, dislocations, and point defects, which increase local electrical resistivity, the perfection within the fiber plays a critical role in the electron transport.

Figure 5.5b shows the electrical conductivity of various fibers as a function of temperature and Table 5.2 also provides the electrical conductivity at 295 K. It is clear that the addition of CNTs leads to improvements in the electrical conductivity in the PAN/CNT based carbon fiber as compared to the PAN based carbon fiber. The GT PAN/CNT-A (0.42 wt%) carbon fiber exhibits a 21% increase in electrical conductivity as compared to the GT PAN based carbon fiber, and a 24% increase as compared to the IM7 carbon fiber. Both the GT PAN based carbon fiber and the GT PAN/CNT-A (0.42 wt%) carbon fiber have similar orientation of turbostratic matrix (f_{matrix}) and crystal size, yet the electrical conductivity increased by 21% with the addition of 0.42wt% CNT-A. It can also be noted that GT PAN/CNT-A (0.42 wt%) exhibits a 6% increase in electrical conductivity at 295 K as compared to GT PAN/CNT-A(1.0 wt%). The higher electrical conductivity in GT PAN/CNT-A (0.42 wt%) can be attributed to the improved

tensile modulus, higher $f_{(002)}$, and larger $L_{(10)}$ and $L_{(002)}$ crystal size of GT PAN/CNT-A (0.42 wt%) as compared to GT PAN/CNT-A (1.0 wt%).
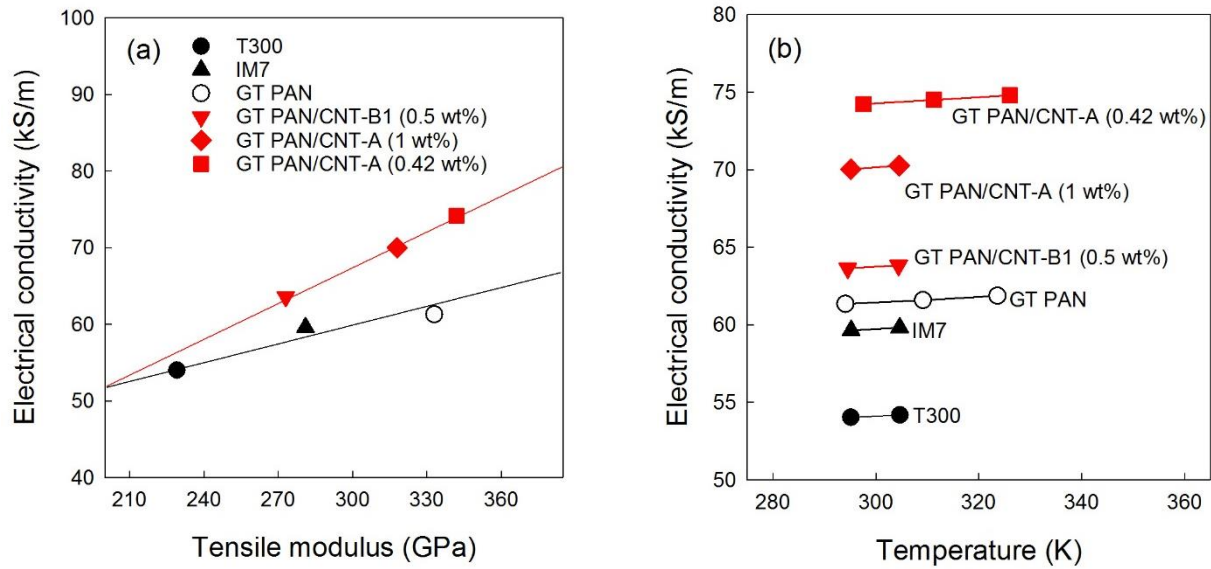
Figure 5.5 Electrical conductivities of various carbon fibers as a function of (a) tensile modulus and (b) temperature. Tensile moduli of various carbon fibers are compliance corrected values.

Considering that the GT PAN/CNT-A (0.42 wt%) carbon fiber has an estimated 1.4 vol% of the HO graphitic region (Table 5.3), the parallel model (Equation 5.7), predicts an electrical conductivity of 74.5 kS/m.

$$\sigma_c = \sigma_p V_p + \sigma_m V_m \tag{5.7}$$

where σ_p, V_p, σ_m, and V_m are the templated graphitic electrical conductivity and volume fraction, matrix electrical conductivity, and matrix volume fraction, respectively.

The volume fraction of the turbostratic matrix is approximately 0.986, as determined from the azimuthal scan and σ_p is which was assumed to be 10^6 S/m and σ_m is 61.3 kS/m as measured for the GT PAN carbon fiber. Use of the parallel model to determine the electrical conductivity coupled with the volume fraction determination WAXD results in a 0.3% error between the measured and predicted electrical conductivity of the GT PAN/CNT-A (0.42 wt%)

carbon fiber. Considering the similar f_{matrix}, $L_{(002)}$, $L_{(10)}$, and tensile modulus of the IM7 and the GT PAN/CNT-B1 (0.5 wt%) fibers, the parallel model can be used to predict the electrical conductivity of the composite fiber within 4% error. Such a calculation results in a predicted electrical conductivity of 66.2 kS/m for the GT PAN/CNT-B (0.5 wt%) carbon fiber where σ_m is 59.6 kS/m for IM7, and V_m is 0.993.

5.3.4 Mechanical properties of the PAN and PAN/CNT based carbon fibers

Single filament tensile testing was conducted based on the testing method established for carbon fibers[96], and the results are listed in Table 5.2. The GT PAN carbon fiber exhibits a 45 and 21% increase in tensile modulus as compared to T300 and IM7. IM7 is 32% stronger than the GT PAN carbon fiber and the GT PAN carbon fiber is 17% stronger than T300, at a 25.4mm gauge length. The lower tensile strength of the GT PAN carbon fiber as compared to IM7 can be attributed to its irregular cross-sectional shape (Figure 5.6c), surface defects, smaller tow size, and lack of surface treatment. For comparison, the cross-sectional SEM images of the T300 and IM7 carbon fibers are also shown in Figure 5.6a and 5.6b, respectively. The T300 carbon fiber shows a non-circular cross-section, the IM7 fiber cross-section exhibits a circular cross-section. Irregular cross-sectional shapes will lead to the uneven oxygen diffusion during stabilization and result in reduced fiber properties[199]. The GT PAN carbon fiber also has an irregular cross-sectional shape as shown in Figure 5.6c, yet does not show the same sheath-core morphology as T300 as observed in Figure 5.1.
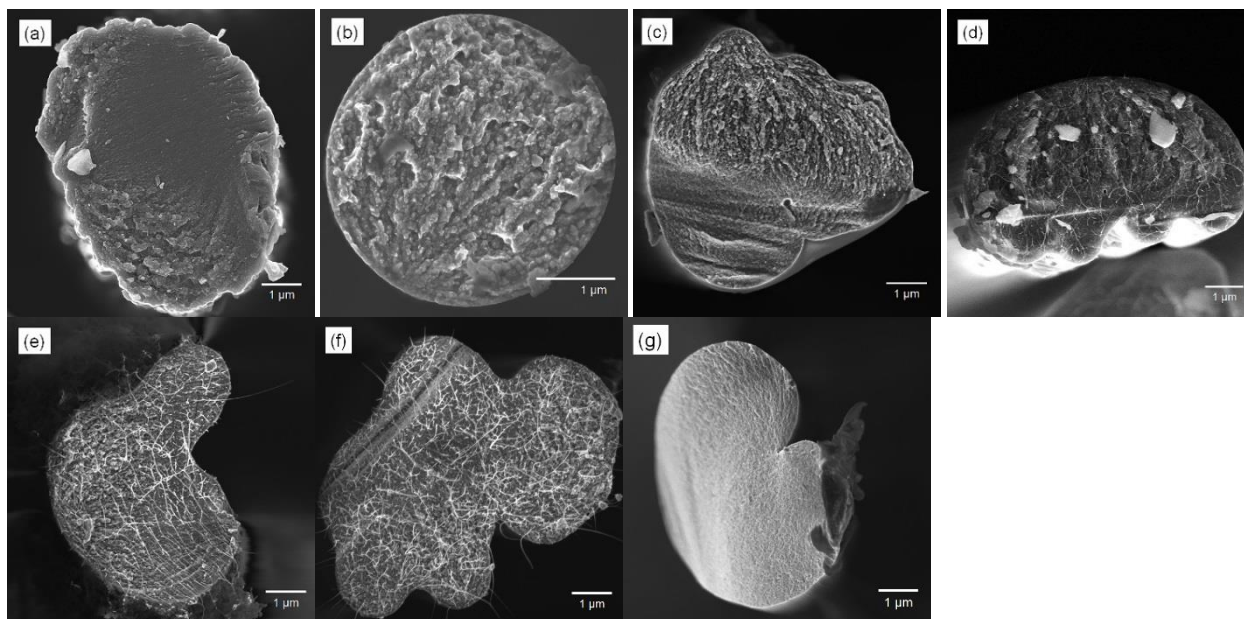
Figure 5.6 SEM cross-sectional images of various carbon fibers: (a) T300, (b) IM7, (c) GT PAN, (d) GT PAN/CNT-A (0.42 wt%), (e) GT PAN/CNT-B1 (0.5 wt%), (f) GT PAN/CNT-A (1.0 wt%), and (g) GT PAN/CNT-C (0.5 wt%).

GT PAN/CNT based carbon fibers also exhibited irregular cross-sectional shapes, and their tensile strengths were lower than those of the T300, IM7, or the GT PAN carbon fibers (Table 5.2). Tensile strength will be dependent upon the presence of defects[73], which needs to be minimized or eliminated, and will be aided through improved CNT dispersion within the PAN/CNT based carbon fiber. Another source of defects is the presence of metallic impurities (present in the as-received CNTs), which have been shown to reduce carbon fiber tensile strength[200]. During carbonization, this can create a void structure in the surrounding carbon material[201]. It was also shown in a controlled study that carbonization in the presence of silicon or iron oxide impurity (~0.1 wt%), the resulting fracture stress reduced by a factor of 3[202]. Therefore, removal of catalytic impurities and purification of CNTs appears to have an important role in the processing and properties of PAN/CNT based carbon fiber. It can also be noted that, based on the HR-TEM study (Figure 5.3b1), the CNT bundle in the composite carbon fiber can

lead to the formation of voids which would not be present in the similarly processed PAN based carbon fiber. Figure 5.7a shows a schematic description of how the bundled nature of the CNTs could introduce voids into the carbonized fiber. These voids are present in the HR-TEM transverse cross section images of the carbon fiber in Figure 5.7b and 5.7c, showing that large voids (4 − 5 nm in transverse direction) are formed. The voids are expected to be created throughout the fiber cross-section due to the non-uniform length of CNTs and bundling of the CNTs. As the CNT bundle takes shape during solution processing and precursor fiber formation due to an imperfect dispersion, regions within the CNT bundle form voids. The voids are the result of either not being accessible by the PAN molecules, or the PAN molecules which can penetrate the once vacant region within the CNT bundle are not able to survive the carbonization process due to an incomplete stabilization reaction by limited oxygen diffusion. In addition, any extraneous metal catalytic impurity within the CNT (about 1 - 3 wt% with respect to the CNT weight in the current study) will be detrimental to the production of high strength carbon fiber. These impurities, along with internal voids and surface defects must be eliminated in order to maximize the potential tensile strength of the PAN/CNT based carbon fiber.
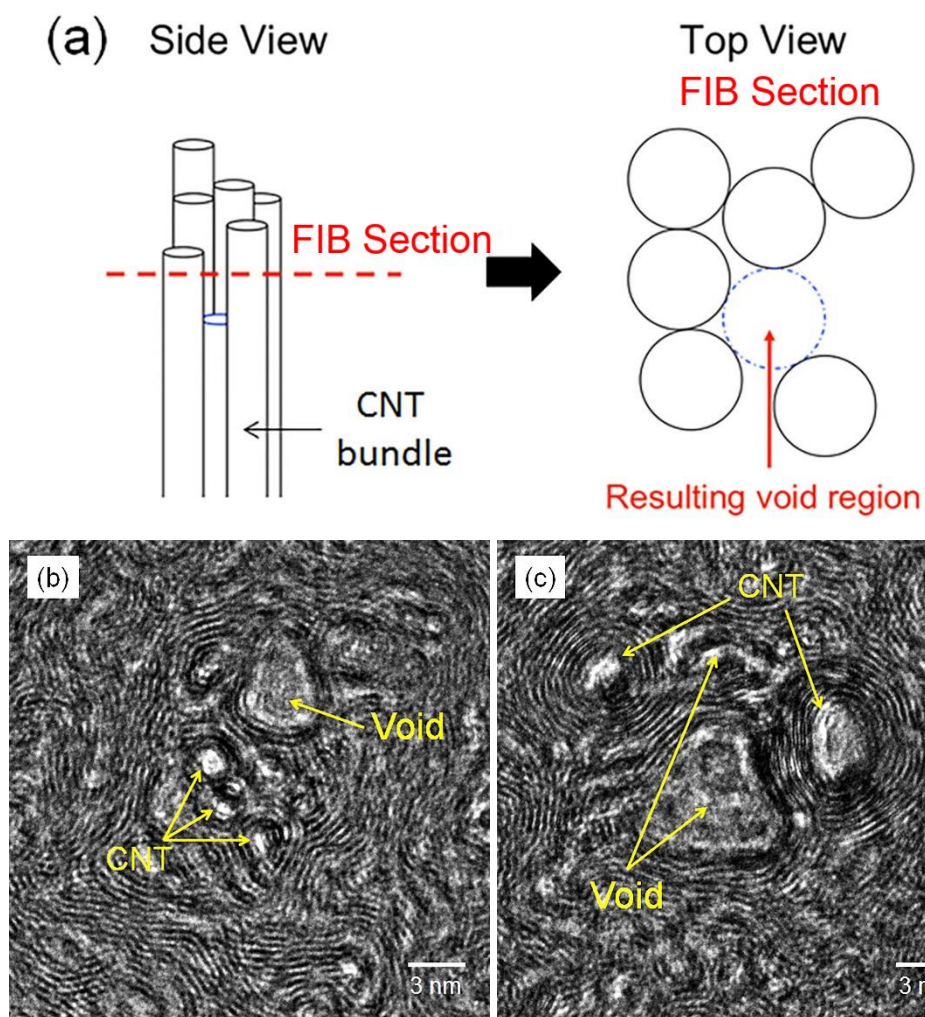
Figure 5.7(a) Schematic description of CNT bundle, showing that the difference in CNT length can result in voids within the fiber cross-section, HR-TEM transverse cross-section images of (b) GT PAN/CNT-A (0.42 wt%) and (c) GT PAN/CNT-A (1.0 wt%), showing the presence of voids.

5.4 Conclusions

Gel spun PAN and PAN/CNT based carbon fibers were produced using a laboratory scale spinning facility and continuous carbonization. HR-TEM study showed that the GT processed PAN and PAN/CNT based carbon fibers had enhanced crystalline perfection as compared to T300 and IM7 fibers. It was also shown that CNTs can provide nucleation sites for graphitic carbon structural development. This led to the improvement in thermal and electrical conductivities. Up to 1.0 wt% CNT addition in the precursor fiber resulted in a 68% increase in

thermal conductivity as compared to the GT PAN carbon fiber, and a 103% and 146% increase over commercially available IM7 and T300 carbon fibers, respectively. Additionally, the GT PAN/CNT based carbon fibers exhibited a 21% increase in electrical conductivity as compared to the GT PAN carbon fiber, and a 24% and 37% increase as compared to IM7 and T300, respectively. However, GT PAN/CNT based carbon fibers showed lower tensile strength than the GT PAN and commercial PAN carbon fibers, which is attributed to the void structure from the CNT bundles and metallic impurities present in the as-received CNTs. Therefore, to obtain high strength and high modulus PAN/CNT based carbon fiber with multi-functionality (high electrical and high thermal conductivities), CNT bundling behavior and metallic impurity content must be minimized.

Chapter 6
CONCLUSIONS AND RECOMMENDATIONS

6.1 Conclusions

PAN precursor fibers and their carbon fibers were prepared from PAN/DMF solutions using a variety of solution preparation conditions. Through the monitoring of the PAN/DMF solution dynamic viscoelastic properties using parallel plate rheology, the relative homogeneity of the solutions as determined from the slope of the Han plot (log G' vs log G'') was correlated to the strength of the corresponding PAN based carbon fibers. In order to manufacture high strength PAN based carbon fiber the number of defects within the fiber must be reduced which begins in the polymer dissolution stage using the fiber production methods described. Complete dissolution of high molecular weight PAN is difficult due to its tendency to form swollen particles within the solvent, which need to be adequately dissolved or filtered prior to precursor fiber spinning. Fiber washing, or the removal of residual solvent on the fiber surface, during fiber drawing play an important role in minimizing the fiber sticking that leads to fibrillation. Carbon fiber tensile strength was improved by 28% when the fiber washing step was incorporated during the drawing process.

Precursor fiber spinning was conducted using multiple fiber spinning conditions to better understand the processing, structure, property relationships in PAN and PAN/CNT precursor fibers. Particular attention was paid to the cross-sectional shape of the fibers as well as on the effect of CNTs on the fiber formation process. Addition of CNTs appeared to have a negative effect on the circularity of the fibers even at 1 wt% CNT loading in the precursor fiber. Cross-sectional shape was shown to be dependent upon the choice of organic solvent (DMF or DMAc), and attributed to the interaction parameters associated with the PAN copolymer, solvent, and

non-solvent. Coagulation bath temperature and composition were also adjusted to investigate their influence on precursor fiber cross-sectional shape when DMF and DMAc were used as a solvent. Finally, the precursor fibers were converted to carbon fiber and the processing, structure, property relationships were investigated for carbon fiber cross-sectional shapes ranging from irregular to circular. Irregular cross-section carbon fibers (manufactured from gel spun PAN based precursor fibers) exhibited tensile strengths as high as 5.8 GPa and tensile modulus values of 375 GPa.

PAN/CNT gel spun fibers were prepared using two types of CNTs to investigate the stress-transfer from the PAN matrix to the reinforcing CNTs through the use of Raman spectroscopy. Interfacial shear strength between the polymer and CNT was found to be dependent upon CNT quality, quality of CNT dispersion, and fiber drawing. Interfacial shear strengths of 13.1 MPa and 30.9 MPa were determined for the as-spun fibers and drawn fibers containing 1 wt% FWNT. Improvements in the CNT dispersion, resulted in PAN/CNT fibers which exhibited interfacial shear strengths as high as 44.3 MPa. As a result of this work, the first experimentally determined interfacial shear strengths in anisotropic polymer/CNT composite fibers were achieved through the monitoring of the *G'* Raman band shifts during the straining of gel spun PAN/CNT composite fibers.

Gel spun PAN and PAN/CNT based carbon fibers were produced using a laboratory scale spinning facility and continuous carbonization in a Class 1000 cleanroom. HR-TEM study showed that the GT processed PAN and PAN/CNT based carbon fibers had enhanced crystalline perfection as compared to T300 and IM7 fibers. It was also shown that CNTs can provide nucleation sites for graphitic carbon structural development. This led to the improvement in thermal and electrical conductivities. Up to 1.0 wt% CNT addition in the precursor fiber resulted

in a 68% increase in thermal conductivity as compared to the GT PAN carbon fiber, and a 103% and 146% increase over commercially available IM7 and T300 carbon fibers, respectively. Additionally, the GT PAN/CNT based carbon fibers exhibited a 21% increase in electrical conductivity as compared to the GT PAN carbon fiber, and a 24% and 37% increase as compared to IM7 and T300, respectively.

6.2 Recommendations

1. Chapter 2 describes the processing conditions used for the dissolution of PAN-co-MAA (M_v = 513,000 g/mol) and the effect of solution homogeneity, as determined from the log G' vs log G'' plot, on the final carbon fiber tensile properties. To date, there is limited work in the literature which investigates this level of homogeneity in polymer nanoparticle/nanotube solutions. Based upon the results presented throughout this dissertation, an effective method of monitoring the bundling of the CNTs prior to final solution processing and fiber spinning must be developed. Correlating the rheological data with bundling behavior (as determined from Raman spectroscopy, Chapter 4) would not only serve the purpose of manufacturing higher quality PAN/CNT solutions for the production of gel spun PAN/CNT based carbon fibers, but also provide a technique that would allow the polymer nanocomposite community to monitor solution homogeneity and quality of CNT dispersion simultaneously using a single technique.

2. Irregular and circular PAN precursor fibers and their carbon fibers were manufactured and reported in Chapter 3. HR-TEM images of the carbon fiber transverse cross-sections were observed, and show a distinct difference in crystallite orientation transverse to the fiber axis. Similar orientation of the turbostratic crystallites was observed in Chapter 5 for the circular IM7 carbon fiber. The effect of this phenomenon should be investigated further. It is possible that the

cross-sectional shape of the fiber is influencing the transverse orientation of the crystallites and there is no evidence to suggest that this orientation improved or reduced mechanical properties.

3. WAXD azimuthal patterns of gel spun PAN/CNT based carbon fibers exhibit a distinct difference. Gel spun PAN/CNT based carbon fibers manufactured with FWNTs exhibit a single azimuthal peak that may be deconvoluted into two separate curves, which represent the turbostratic region and the highly ordered graphitic region. In contrast, gel spun PAN/CNT based carbon fibers manufactured with MWNTs exhibit a single azimuthal peak that is fit to a single curve, and suggests that graphitic templating does not occur in these carbon fibers. Due to the varying diameter and number of walls in the MWNTs, it is not possible to conclude that graphitic templating occurs in the gel spun PAN/CNT based carbon fibers manufactured from MWNT from the HR-TEM imaging. Considering the relative ease of dispersing the MWNTs as compared to the FWNTs, it would be advantageous to utilize the MWNTs in such a way that drives the graphitic templating formation, and can be studied using dilute solution crystallization in PAN/CNT solutions where SWNTs, FWNTs, and MWNTs are used to investigate polymer crystallization on the surface of the CNTs.

4. Gel spun PAN and PAN/CNT based carbon fibers exhibit distinctly different Raman spectra. The presence of a sharp *G*-mode in PAN and PAN/CNT based carbon fibers is an indicator of graphitic structure in the fiber, which is significantly different than that of the turbostratic structure. A strong *G*-mode is observed in the PAN/CNT carbon fibers, and is generally accepted to provide evidence of graphitic templating. However, as observed in Appendix D, a 90° rotation of the fiber significantly reduces the intensity of the *G*-mode. Provided with this observation, it now becomes possible to investigate the stress transfer in PAN/CNT carbon fibers using Raman spectroscopy. Recently, interfacial shear strength values

between the turbostratic matrix and incorporated CNTs have been measured as 32 ± 3 MPa[47], and 110 ± 15 MPa[203]. Utilization of a series of fibers with ranging stabilization conditions should provide the data required to develop the fundamental understanding of the effect of stabilization conditions on the interfacial interaction between the turbostratic matrix and the incorporated CNT.

Appendix A
REINFORCEMENT EFFICIENCY OF PEK/CNT FIBERS

A.1 Introduction

Aromatic polyethers such as poly(ether ketone) (PEK), poly(ether ether ketone) (PEEK), and poly(ether ketone ketone) (PEKK) are important engineering thermoplastics due to their high strength and toughness, high thermal stability, as well as their chemical and wear resistance[204]. Aromatic polyether nanocomposites containing multiwalled carbon nanotubes (MWNTs), few walled carbon nanotubes (FWNTs), single walled carbon nanotubes (SWNTs), and carbon nanofibers (CNFs) have been processed using in situ polymerization and covalent grafting to the carbon nanotubes (g-CNTs)[205-211] and (g-CNFs)[205, 212], as well as processing in the solution or in the melt[213-215]. PEK nanocomposites have also recently been developed containing graphene oxide[216], ZnO[217, 218], Si_3N_4[219], hydroxyapatite (HA)[220, 221], Al_2O_3[222-225], and SiO_2[223, 226]. Incroporation of these nanomaterials/particles has been shown to increase the tensile properties, wear life, microhardness, and antibacterial properties in PEK nanocomposites.

The effect of the nanofiller on the polymer nanocomposite properties depends on the size, shape, surface modification, interfacial adhesion, and quality of dispersion of the nanofiller. Nanofillers such as CNTs with a high aspect ratio can be utilized to improve the polymer nanocomposite mechanical properties despite their tendency to aggregate[227], with functionalization and polymer grafting employed as physical methods to keep the CNTs from aggregating. Interfacial adhesion of the polymer to the nanofiller surface also plays a critical role in the mechanical and physical properties associated with the polymer nanocomposite. The glass transition temperature (T_g) of the nanocomposite is lowered[228, 229], raised[25, 33, 34, 230, 231], or remains the same as compared to the neat polymer, and is

strongly dependent upon the interfacial adhesion of the polymer to the nanofiller. The changing of the T_g is attributed to the interfacial polymer layer, which has different properties than the bulk polymer. The thickness of the interfacial layer has been calculated to be in the range of ~10 nm, despite T_g measurements in thin films suggesting that confinement effects persist up to ~100 nm[232].

Previously, PEK and PEK/g-FWNT fibers were prepared with g-FWNT contents ranging from 1-20 wt% where the molecular weight of the grafted PEK chains to the surface of the FWNT decreased as the FWNT content increased. The fibers were drawn to the maximum extent possible with the draw ratio reducing as the g-FWNT increased, with the exception of the fiber containing 10 wt% g-FWNT (PEK-g-10%FWNT) which could be drawn 60% further than the control PEK fiber. The PEK-g-20%FWNT fiber exhibited a 20 ℃ drop in T_g as compared to the control PEK fiber and was attributed to the low molecular weight of the grafted PEK chains to the surface of the FWNTs. Toughness values of 130 J/g were reported for the undrawn PEK fibers with maximum toughness values of 122 J/g for the drawn PEK-g-5%FWNT fibers[211].

Currently there is limited work focused on the determination of the interfacial shear strength (τ_c) in polymer/CNT composites and its relation to the same polymer matrix but with the use of g-CNTs as opposed to neat CNTs. Frankland et al. used molecular dynamics simulations of a (10, 10) SWNT in the presence of a polyethylene (PE) matrix. τ_c values were determined for the neat (10, 10) tube surrounded by an amorphous (2.7 ± 0.2 MPa) or crystalline (2.8 ± 0.2 MPa) matrix, as well as for the (10,10) SWNT cross-linked to the amorphous (30 ± 3 MPa) or crystalline (110 ± 13 MPa) matrix[39]. Such a system can be related to a neat polymer/CNT system where the polymer

matrix neighboring the CNT is either amorphous or crystalline or as a polymer/g-CNT system where the polymer chains grafted to the CNT are amorphous or crystalline. To date there is no experimental data on this topic and the overall data is limited.

In this appendix, PEK nanocomposite fibers were prepared using dry-jet wet spinning to investigate the effect of nanofiller type on the structure and properties of PEK/CNF, PEK/MWNT, and PEK/FWNT fibers prepared with 5 wt% nanofiller loading. Additional PEK/FWNT fibers were prepared using similar processing techniques to investigate the effect of the FWNT loading percent on the structure and properties of the dry-jet wet spun PEK/FWNT fibers. Finally, the effect of PEK chain grafting to the surface of the FWNT on the load transfer properties is compared to the PEK/FWNT fibers prepared with the neat FWNT.

A.2 Experimental

A.2.1 Materials

Reagents and solvents were obtained from Sigma Aldrich and used as-received. The monomer, 4-phenoxybenzoic acid (4-PBA), was purified by recrystallization from toluene/heptanes. MWNTs were obtained from Cheaptubes (impurity < 5%) and FWNTs (Lot # XO437VA, impurity < 4%) were obtained from Unidym Inc. (Houston, TX).

A.2.2 Fiber Spinning

PEK/PPA solutions were prepared at a concentration of 10 wt% polymer. CNF and MWNT were added to the PEK/PPA solutions until the respective solutions contained 5 wt% CNF or MWNT with respect to the weight of the polymer. Similarly, FWNTs were added to PEK/PPA solutions until the respective solutions contained 5, 10, or 28 wt% FWNTs with respect to the weight of the polymer.

PEK/CNT fibers were prepared through dry jet wet spinning using a Bradford University Research, Ltd (UK) spinning system using a single-hole spinneret (120 μm diameter). The PEK/CNT/PPA solutions were maintained at 150 ℃ before extrusion (0.5 mm/min) and coagulation in a deionized water bath with a spin draw ratio (SDR) of 1. Fibers were kept in deionized water for 4 days to aid in PPA extraction, prior to hot drawing at 200 ℃ with a draw ratio (DR) of 1.76. Two fibers were collected from the PEK/FWNT fiber containing 28 wt% FWNT. The first was collected immediately after fiber spinning and did not undergo any fiber drawing, while the second fiber underwent similar drawing as the other PEK/CNT fibers with a DR of 1.76 at 200 ℃. PEK-g-5%FWNT fiber was also obtained with a DR of 1.8 at 200 ℃ using previously reported methods[211] for comparison with the PEK/FWNT(5%) fiber.

A.2.3 Characterization

Single filament mechanical properties were determined using a FAVIMAT tensile testing instrument at a gauge length of 25.4 mm, and a strain rate of 1%/sec. Fiber linear density was obtained for each filament tested using an inline vibroscope. Conversion from tenacity (cN/tex) to tensile strength (GPa) was performed with an assumed density of 1.30 g/cm^3 for all filaments. Thermogravimetric analysis (TGA) was performed under a nitrogen flow rate at 60 mL/min from 30 ℃ to 700 ℃ at a heating rate of 10 ℃/min. Fiber cross-sections and surfaces were observed using a Zeiss Ultra 60 FE-SEM at an operating voltage of 2 keV after TGA heating up to 700 ℃. Shrinkage behavior was observed using a TA Instrument (Q400) thermal mechanical analyzer (TMA) on 10 filament bundles under an air flow rate of 50 mL/min and a 2 MPa stress at a heating rate of 10 ℃/min from 30 ℃ to 375 ℃. Dynamic mechanical analysis (DMA) was performed

using a RSA III solids analyzer on 50 filament bundles at a gauge length of 25.4 mm using a temperature sweep test from 25 ºC to 300 ºC at a heating rate of 1 ºC/min using frequencies of 0.1, 1, and 10 Hz. Modulated dynamic scanning calorimetry (MDSC) was performed from -50 ºC to 400 ºC at a heating rate of 2 ºC/min with modulation of ±0.43 ºC per 80 seconds prior to cooling at 5 ºC/min to -50 ºC and an isothermal treatment at -50 ºC for 5 min prior to second heating at 2 ºC/min with the same modulation up to 400 ºC. Wide angle x-ray diffraction (WAXD) was performed on 100 filament bundles using a Rigaku Micromax-002 ($\lambda = 0.1542$ nm, operating voltage 45 kV, operating current 0.65 mA). Diffraction patterns were recorded on a Rigaku R-axis IV++ detection system and analyzed by AreaMax (version 1.00) and MDI Jade (version 6). Analysis of the WAXD diffraction patterns provided PEK/CNT fiber structural information including PEK crystallinity, PEK crystal size in the (110) and (200) directions ($L_{(110)}$ and $L_{(200)}$, respectively), and Herman's orientation factor (f_{PEK}) as determined using methods previously described[211, 233]. Raman spectroscopy was performed on single filaments using a Horiba Raman microscope (Xplora, $\lambda = 785$ nm) at a laser power (1% power) of ~500 µW using a 100x objective. Single filament deformation of PEK/CNT fibers was performed using a gauge length of 25.4 mm with 0.125 mm step sizes using a Thorlabs motorized stage (MTS25-Z8). FWNT orientation was obtained from single filament Raman spectroscopy using a 20x objective using parallel (VV mode) and crossed (VH mode) polarizers with the fiber angled at 0º and 90º with the incident Raman laser according to methods previously described[124].

A.3 Results and Discussion

Single filament tensile testing of the PEK/CNT fibers presents distinctly different stress-strain curves for the various fibers as presented in Figure A. 1. The as-spun PEK/FWNT(28%) and drawn PEK/FWNT(28%) fibers exhibit the most drastic deviation from the other PEK/CNT fibers due to their strain to failure values of 6% and 5%, respectively. PEK/MWNT(5%) fiber exhibits the highest tensile strength of the PEK/CNT composite fibers (257 MPa) while the PEK/FWNT(10%) fiber exhibits the highest toughness (108 J/g). Table A. 1 provides the summary of the fiber tensile properties which further illustrates the effect of high FWNT loading on the tensile properties of the PEK/FWNT fibers with the tensile modulus continually increasing as the FWNT content increases and a maximum in tensile strength occurring in the PEK/FWNT(10%) fiber. Comparison of the PEK/CNF(5%), PEK/MWNT(5%), and PEK/FWNT(5%) fibers suggests that the MWNT is the preferred nanofiller for the PEK/CNT fibers in terms of tensile strength and tensile modulus.
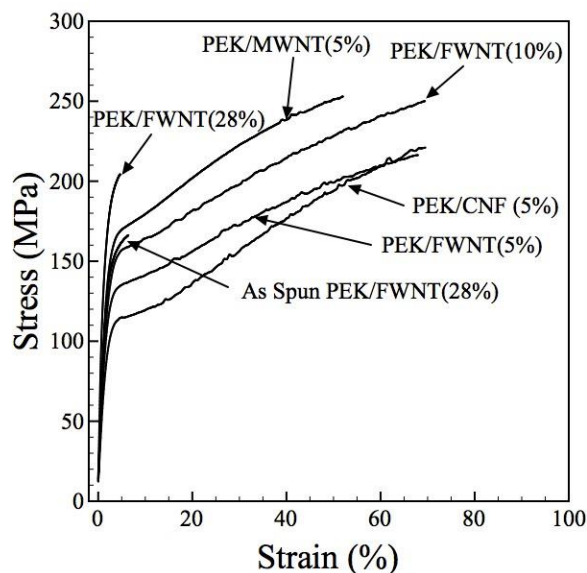
Figure A. 1 Stress-strain curves of the PEK/CNT composite fibers.

Table A. 1 Mechanical properties of PEK/CNT composite fibers.

Fiber	Draw Ratio	Fiber Diameter (µm)	Tensile Strength (MPa)	Tensile Modulus (GPa)	Strain to Failure (%)	Toughness (J/g)
PEK/CNF (5%)	1.76	25.9 ± 0.7	230 ± 8	5.8 ± 0.1	71 ± 6	88
PEK/MWNT (5%)	1.76	24.0 ± 0.2	257 ± 3	8.2 ± 0.1	53 ± 4	84
PEK/FWNT (5%)	1.76	25.8 ± 0.3	212 ± 8	6.7 ± 0.2	68 ± 11	91
PEK/FWNT (10%)	1.76	25.0 ± 0.3	246 ± 8	7.8 ± 0.3	72 ± 10	108
PEK/FWNT (28%)	1.76	25.9 ± 0.6	201 ± 19	14.4 ± 0.5	5 ± 1	6
PEK/FWNT (28%)	1.00	28.7 ± 0.6	150 ± 19	9.9 ± 0.6	6 ± 3	7

Structural parameters of the PEK/CNT fibers are presented in Table A. 2. All fibers exhibited calculated crystallinity values of less than 40% with increasing FWNT content reducing the PEK crystallinity despite the drawn fibers undergoing similar processing conditions. The PEK/CNF(5%), PEK/MWNT(5%), and PEK/FWNT(5%) fibers all show similar levels of crystallinity which suggests that the type of nanofiller present at 5% loading does not effect the overall crystallinity of the PEK/CNT fibers when similar processing conditions are used. However, the PEK/CNF(5%) fibers exhibit the lowest f_{PEK} of the fibers which contain 5% nanofiller, helping to further explain the

143

tensile modulus of 5.8 GPa for the PEK/CNF(5%) fiber as compared to 6.7 and 8.2 GPa for the PEK/FWNT(5%) and PEK/MWNT(5%) fibers, respectively, which exhibit higher f_{PEK} than the PEK/CNF(5%) fiber. It is interesting to note the large increase in f_{PEK} and L_{110} due to fiber drawing at 200 ℃ in the PEK/FWNT(28%) composite fiber. More interesting is the decrease of L_{200} from 5.37 nm to 4.07 nm due to fiber drawing in the PEK/FWNT(28%) fiber.

Table A. 2 Structural parameters as determined by WAXD and f_{CNT} as determined by Raman spectroscopy of the PEK/CNT fibers.

Fiber	Draw Ratio	Crystallinity (%)	f_{PEK}	f_{CNT}	L_{110} (nm)	L_{200} (nm)
PEK/CNF (5%)	1.76	36	0.285		6.56	4.35
PEK/MWNT (5%)	1.76	37	0.335		5.95	3.88
PEK/FWNT (5%)	1.76	37	0.326	0.765	6.75	4.12
PEK/FWNT (10%)	1.76	30	0.274	0.797	5.93	3.63
PEK/FWNT (28%)	1.76	28	0.376	0.598	5.74	4.07
As-spun PEK/FWNT (28%)	1.00	N/A	0.051		2.20	5.37

CNT orientation in the PEK/FWNT fibers was determined through Raman spectroscopy, and the f_{CNT} values are reported in Table A. 2. Figure A. 2 plots the Raman spectra as a function of angular rotation for the PEK/FWNT(5%) fiber during parallel (I_{VV}) laser polarization, exhibiting a decrease in intensity of the Raman G-band as the fiber is rotated. It is of note that the f_{CNT} of the PEK/FWNT(5%) and PEK/FWNT(10%) fibers are comparable, while the f_{CNT} of the PEK/FWNT(28%) fiber is reduced. These results are in direct contrast to those of PEK/g-FWNT fibers where the highest f_{PEK} occurs in the samples with the lowest g-FWNT loading and the highest f_{CNT} occurs in the samples with the highest g-FWNT loading[211]. However, from the f_{PEK} and f_{CNT} data for all samples

presented here, f_{CNT} is higher than f_{PEK}, suggesting that the larger CNTs can influence the PEK crystallite orientation.
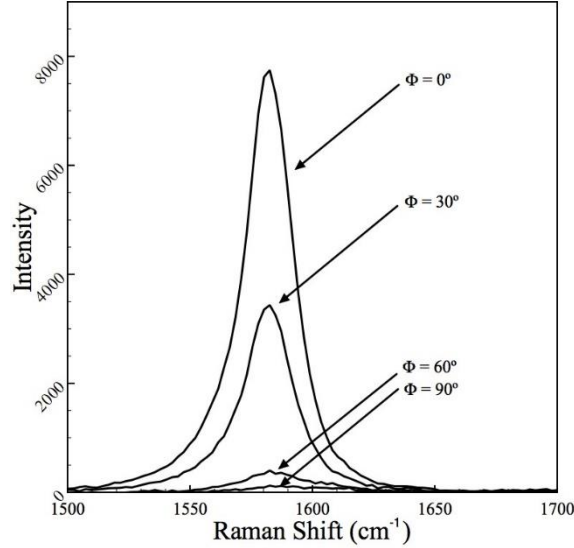
Figure A. 2 *G*-band Raman spectra of the PEK/FWNT(5%) fiber. The angle, Φ, is the angle between the incident Raman polarization direction and the fiber axis.

Figure A. 3a and Figure A. 3b plot the storage modulus (log *E'*) and *tan δ* behavior of the PEK/CNT fibers as a function of temperature at 0.1 Hz, respectively. At low temperature, the storage modulus of the PEK/CNT composite fibers show a comparable trend with the tensile modulus obtained from the single filament tensile testing. All PEK/CNT fibers show a comparable overall trend in their storage modulus as a function of temperature. In comparison, the *tan δ* behavior of the PEK/FWNT fibers are distinct from that of the PEK/CNF(5%) and PEK/MWNT(5%) fibers. From the peak of the *tan δ* behavior, the PEK/CNF(5%) and PEK/MWNT(5%) fibers exhibit a glass transition temperature (T_g) of 177 and 185 ℃, respectively, as tabulated in Table A. 3. The three drawn PEK/FWNT fibers exhibit two distinct *tan δ* peaks as observed by their *tan δ* behavior in Figure A. 3b. In the case of the PEK/FWNT(5%) fiber, the glass

145

transition temperature (T_g) occurs at 188 ºC while the second *tan δ* peak (*tan δ₂*) is observed at 243 ºC. As the FWNT content is increased to 10 and 28%, T_g is increased to 192 and 207 ºC respectively. However, the PEK/FWNT(10%) fiber exhibits the highest *tan δ₂* of the fibers tested, at a temperature of 256 ºC. A second *tan δ* peak was observed in PVAc/silica nanocomposites[234] and was attributed to a second glass transition temperature due to restricted chain mobility of the polymer chains interacting with the silica surface. Using dielectric relaxation spectroscopy and DSC for PDMS/silica nanocomposites two glass transition temperatures were observed with the second glass transition temperature being attributed to the interfacial PDMS interacting with the surface of the silica nanoparticles[235]. The thickness of PDMS/silica interfacial layer was determined to be in the range of 2.1 − 2.4 nm. Similar observations have been made in styrene-butadiene-rubber/silica nanocomposites with a calculated ~2 nm interfacial layer thickness[228] and PVA/silica nanocomposites with a calculated ~10 nm interfacial layer thickness[236]. Other observations attribute the *tan δ₂* peak to the chain diffusion/reptation and not the softening behavior associated with a glass transition[237].
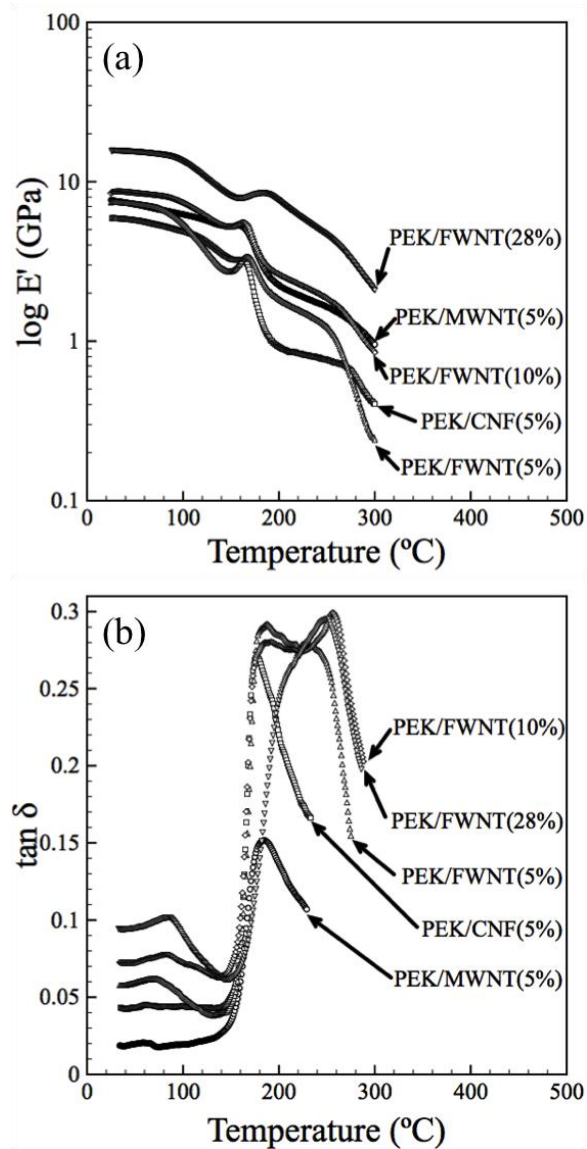
Figure A. 3 Dynamic mechanical properties of the drawn PEK/CNT fibers. (a) Storage modulus and (b) tan δ behavior as a function of temperature.

Table A. 3 Glass transition temperature(s) of the PEK/CNT fibers as determined by DMA tan δ behavior and melting temperature determined from DSC.

Fiber	T_g (°C)	tan δ_2 (°C)	$\Delta T_g^{\#}$ (°C)	T_m (°C)
PEK/CNF (5%)	177			342
PEK/MWNT (5%)	185			348
PEK/FWNT (5%)	188	243	55	344
PEK/FWNT (10%)	192	256	64	345
PEK/FWNT (28%)	207	251	44	

[#] ΔT_g is tan $\delta_2 - T_g$ for the fibers which exhibit two tan δ peaks in their tan δ behavior.

147
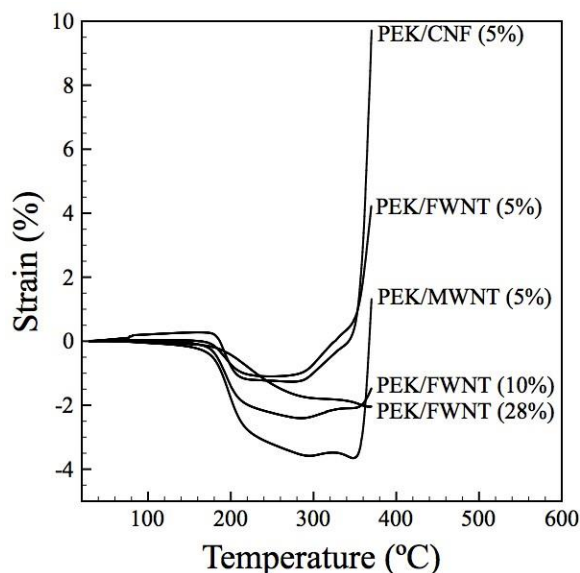
Figure A. 4 Thermal shrinkage behavior of the PEK/CNT fibers in air up to 375 ℃ under a 2 MPa tension at a heating rate of 10 ℃/min.

Figure A. 4 plots the thermal shrinkage behavior of the PEK/CNT fibers under a 2 MPa stress from 30 ℃ to 375 ℃ in the presence of air. All fibers began to show shrinkage near their respective T_g, followed by rapid expansion as the fibers were heated towards their T_m for the PEK/CNT fibers with 5% nanofiller loading. However, the PEK/FWNT(10%) and PEK/FWNT(28%) fibers did not exhibit rapid expansion at temperatures up to 375 ℃, which is surprising due to their T_m being similar to those in the other PEK/CNT fibers. The thermal shrinkage results suggest that the FWNTs are influencing the crystallite regions within the PEK fibers as evidenced by the dimensional stability at temperature ~25 ℃ higher than their T_m as determined from DSC. Coupling the *tan δ* behavior of the PEK/FWNT fibers with the thermal shrinkage behavior it is possible to conclude that the presence of the FWNTs in the PEK fibers is influencing both the amorphous and crystalline regions within the fibers through the *tan $δ_2$* peak in

148

the DMA (Figure A. 3b) and the dimensional stability of the PEK/FWNT(10%) and PEK/FWNT(28%) fibers above T_m in Figure A. 4.

The thermal stability of the PEK/CNT fibers in an inert nitrogen environment is presented in Figure A. 5. The onset of degradation (T_d) occurs between 544 – 583 ºC, while the char yield at 700 ºC is between 57 and 64% for the PEK/CNT fibers. The char yield increases from 58-60-64% as the FWNT content increases from 5-10-28%. Such an observation is contrary to that of PEK/g-FWNT fibers[211], which showed decreasing char yield as the FWNT content was increased. In the case of the PEK/g-FWNT fibers, as the FWNT content was increased, the molecular weight of the PEK grafted to CNT was systematically decreased due to the method in which the reaction proceeds, therefore reducing the char yield as the FWNT content was increased.
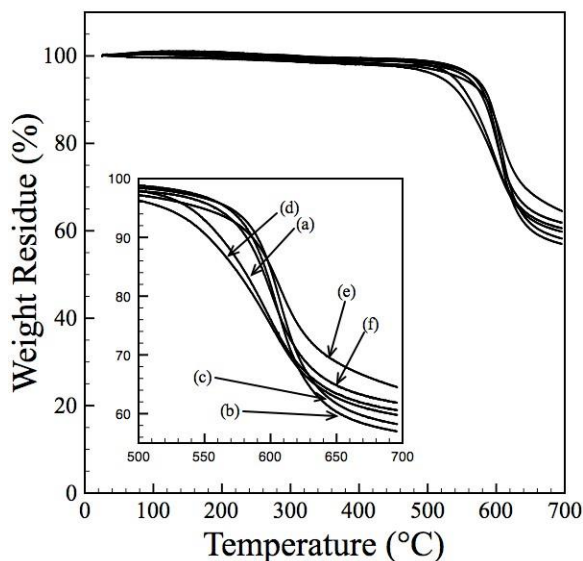
Figure A. 5 Thermogravimetric analysis of the PEK/CNT fibers. (a) PEK/CNF(5%), (b) PEK/MWNT(5%), (c) PEK/FWNT(5%), (d) PEK/FWNT(10%), (e) PEK/FWNT(28%), and (f) as-spun PEK/FWNT(28%).

Figure A. 6 presents the cross-sectional SEM images of the PEK/CNT fibers with 5 wt% loading after the completion of the TGA experiment. As can be seen at low magnification in Figure A. 6a1, the PEK/CNF(5%) fiber shows CNF rich regions highlighted by the arrow where the CNFs are not uniformly dispersed and are more clearly observed in Figure A. 6a2 under high magnification. Similarly, the PEK/MWNT(5%) fibers show MWNT rich regions highlighted by the arrow in Figure A. 6b1 and shown at a higher magnification in Figure A. 6b2. Convsersely, the PEK/FWNT(5%) fiber in Figure A. 6c1 shows a uniform dispersion of FWNTs which are observed to be uniformly dispersed bundles in Figure A. 6c2.

Similar observations can be made from the surface images of the PEK/CNT fibers after TGA heating in N_2 up to 700 ºC. Figure A. 7a1 is the low magnification surface image of the PEK/CNF(5%) fiber and large CNF aggregations can be observed, as shown by the arrow. Higher magnification of this region in Figure A. 7a2 provides further support that this aggregation is indeed from the CNF, which was not well dispersed within the PEK fiber matrix. Surface images of the PEK/MWNT(5%) fiber also exhibit MWNT aggregates in Figure A. 7b1 and under higher magnification in Figure A. 7b2. In contrast to the PEK/CNF(5%) and PEK/MWNT(5%) fibers, the PEK/FWNT(5%) fiber exhibits a surface devoid of FWNT aggregation (Figure A. 7c1 and Figure A. 7c2), suggesting a homogeneous dispersion of the FWNTs throughout the fiber, despite their propensity to form FWNT bundles as evidenced in Figure A. 6c2.
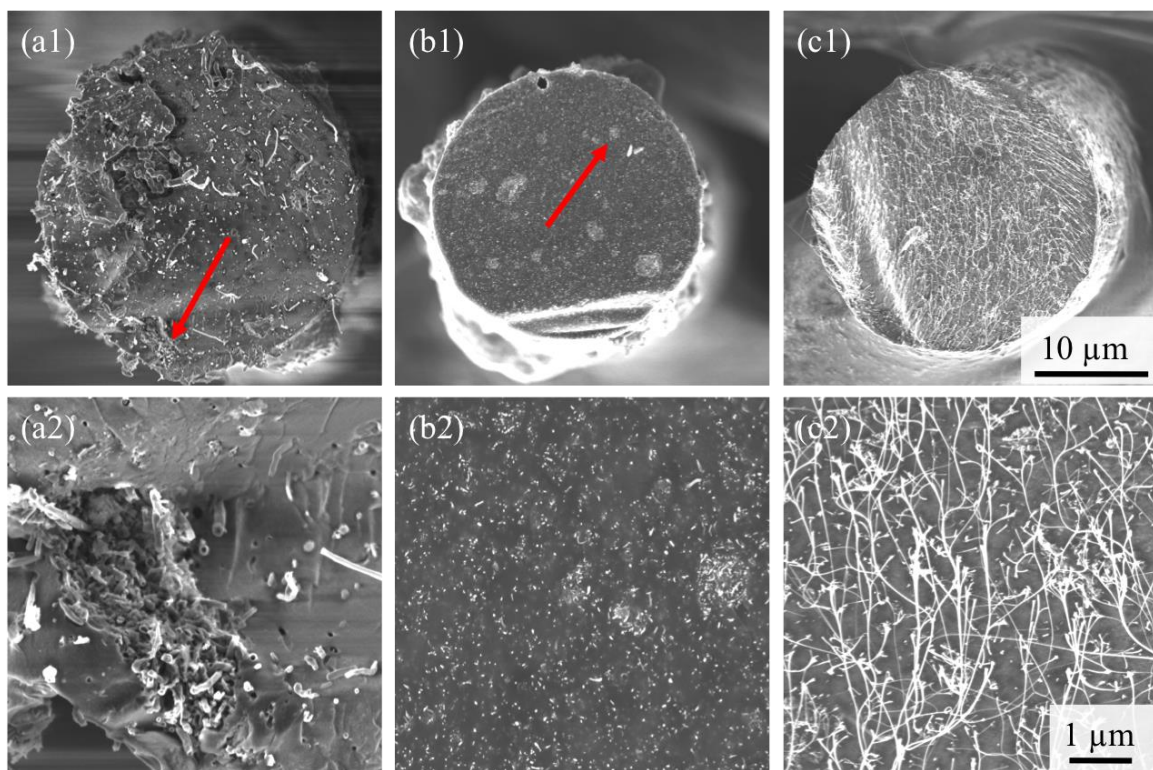
Figure A. 6 Cross-sectional SEM images of (a1, a2) PEK/CNF(5%), (b1, b2) PEK/MWNT(5%), (c1, c2) PEK/FWNT(5%) fibers after completion of TGA in N2 up to 700 ℃.
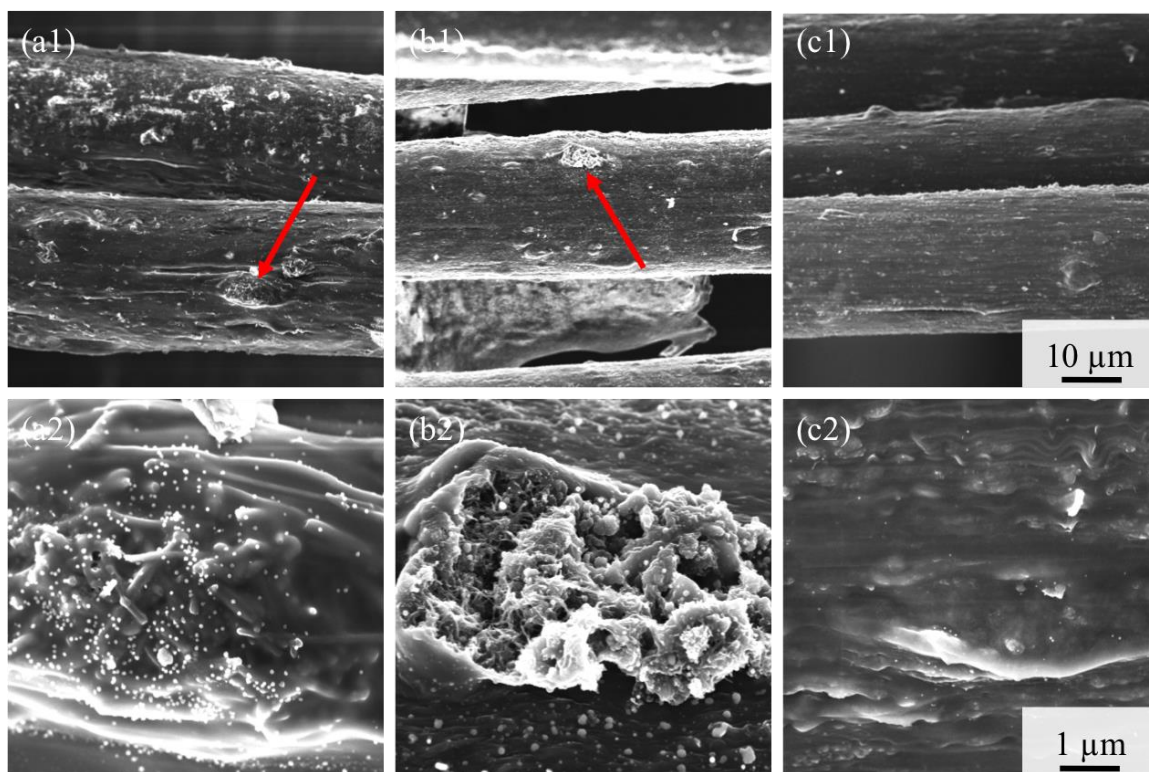
Figure A. 7 Surface SEM images of (a1, a2) PEK/CNF(5%), (b1, b2) PEK/MWNT(5%), (c1, c2) PEK/FWNT(5%) fibers after completion of TGA in N2 up to 700 °C.

Figure A. 8a presents the *G* band Raman shift of the PEK/FWNT(5%) and PEK/MWNT(5%) fibers, while Figure A. 8b presents the *G* band Raman shift of the PEK/FWNT(5%) and PEK/g-FWNT(5%) fibers. The downshift in the *G* band is attributed to the carbon-carbon bond stretching in the CNTs. As the PEK/CNT composite fiber is strained, the CNTs within the fiber will also strain due to the transfer of stress from the PEK matrix to the reinforcing CNT. From Figure A. 8b it is clear that the PEK/g-FWNT(5%) fiber exhibits a steep downshift in the *G* band peak position before reaching a plateau where the *G* band peak position ceases to shift to a lower wavenumber. The same behavior is observed in the PEK/FWNT(5%) fiber, with the exception that the downshift in the *G* peak position is not as significant as in the PEK/g-FWNT(5%) fiber. Similarly, the PEK/MWNT(5%) fiber shows a minimal downshift in the *G* band peak

position as a function of filament strain. Through the averaging of the ΔG shift in the plateau region (S_m) the strain in CNTs (ε_{CNT}) can be calculated using the expression $\varepsilon_{CNT} = S_m/S_{CNT}$, where S_{CNT} is the shift rate of G Raman band peak position as previously determined to be -16.7 cm^{-1} / % strain for individual SWNTs[53]. With the knowledge that the interfacial shear strength (τ_i) is directly related to the strain in the reinforcing element, it can anticipated that the PEK/g-FWNT(5%) fiber exhibits the highest τ_i of the three fibers tested, with the PEK/MWNT(5%) fiber yielding the lowest τ_i. Such observations have been reported when comparing the G' band Raman shift in epoxy/SWNT and epoxy/MWNT composites[63] without correlating the G' band Raman downshift to the τ_i of the two composites. In a molecular dynamics comparison between PE/SWNT composites and PE/SWNT composites containing covalently cross-linked PE chains to the crystalline PE matrix, the minimum shear stress (τ_c) was increased from 2.8 to 110 MPa[39]. The increase in τ_c attributed to the covalent bonding of the SWNT to the crystalline matrix in the PE/SWNT composite takes a similar form as the PEK/g-FWNT discussed here. In the case of the PEK/g-FWNT, PEK chains are covalently bonded to the surface of the FWNT with a calculated grafted chain molecular weight of 8894 g/mol. It is possible that the grafted chains crystallize with the surrounding PEK matrix within the fiber or that the grafted PEK chains are left un-crystallized while still interacting with a surrounding amorphous PEK matrix. In the same study by Frankland et al.[39], τ_c of covalently bonded PE/SWNT composites to an amorphous PE matrix was determined to be 30 MPa, a near 11-fold improvement in τ_c. Assuming the same structural parameters and orientation of the FWNTs used in the PEK/FWNT(5%) and PEK/g-FWNT(5%) fibers a near 6-fold

improvement in τ_i is expected based upon the G band downshift data in Table A. 4 for the two fibers.
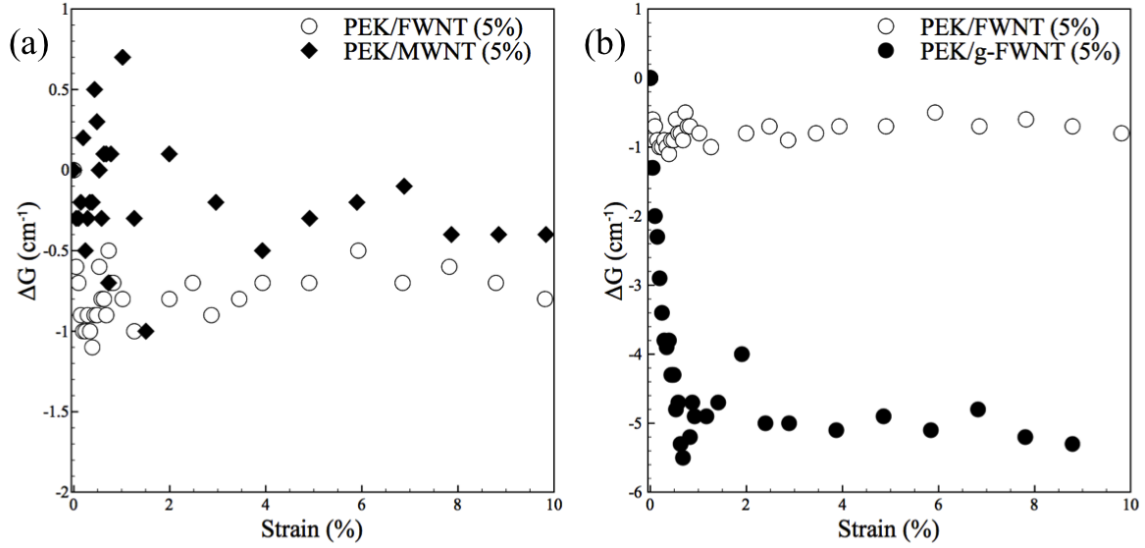
Figure A. 8 ΔG as a function of filament strain for the (a) PEK/FWNT(5%) and PEK/g-FWNT(5%)[211] fibers and (b) PEK/FWNT(5%) and PEK/MWNT(5%) fibers.

Table A. 4 ΔG Raman band shifts and calculate ε_{CNT} for the PEK/CNT fibers

Fiber	$S_m, \Delta G \,(\text{cm}^{-1})$	$\varepsilon_{CNT}(\%)$
PEK/MWNT (5%)	-0.5	.030
PEK/FWNT (5%)	-0.8	.048
PEK/g-FWNT (5%)	-4.6	.275

A.4 Conclusions

PEK/CNT fibers were prepared using dry-jet wet spinning using 5 wt% CNF, MWNT, and FWNTs. PEK/FWNT fibers were also prepared with 10 and 28 wt% FWNT. As-spun and drawn PEK/FWNT(28%) fibers exhibited strikingly different stress-strain behavior as compared to the other PEK/CNT fibers. PEK/FWNT fibers with 5, 10, and 28 wt% loading exhibited two *tan δ* peaks as compared to the PEK/CNF(5%) and PEK/MWNT(5%) fibers, which only showed a single *tan δ* peak. The first *tan δ* was

associated with the T_g of the sample, which increased as the FWNT content increased, while the *tan δ_2* peak appeared up to 64 °C higher than the corresponding T_g. Potential explanations for *tan δ_2* only occurring in the PEK/FWNT fibers is due to the large aggregates observed by SEM in the PEK/CNF(5%) and PEK/MWNT(5%) fibers and not in the PEK/FWNT(5%) fibers. Raman G band shifts were monitored as a function of fiber strain for the PEK/MWNT(5%) and PEK/FWNT(5%) fibers and compared to PEK-g-5%FWNT fibers previously presented in the literature[211]. S_m of the Raman G band is higher in the PEK/FWNT(5%) fiber as compared to the PEK/MWNT(5%) fiber suggesting a better stress transfer in the PEK/FWNT(5%) fibers. Similarly, the PEK-g-5%FWNT fibers exhibited a larger S_m as compared to the PEK/FWNT(5%) fiber suggesting that the grafting of the PEK chain (M_w = 8894 g/mol) to the surface of the FWNT will enhance the τ_c nearly six times if the FWNT orientation and FWNT elastic modulus are the same for the two fibers.

Appendix B
THERMAL STABILITY OF PAN AND PAN/CNT BASED CARBON FIBERS

B.1 Introduction

Carbon fibers are members of a unique class of materials due to their ability to maintain their excellent mechanical properties in the presence of an inert environment or vacuum at elevated temperatures. Despite this remarkable behavior in an inert environment, carbon fibers are susceptible to oxidation at elevated temperatures when exposed to the presence of ambient air or oxygen. It is well understood that the edge sites of the graphitic structure are oxidized more easily than the basal plane and that such a reaction results in weight loss[238] as well as a reduction in fiber mechanical properties[239]. It is generally understood that the oxidation resistance of carbon fiber scales with the tensile modulus of the fiber[240], with turbostratic carbon fibers possessing a lower modulus and reduced oxidation resistance as compared to highly ordered pyrolytic graphite (HOPG)[241, 242]. Ceramic coatings such as SiC and boron based 'composite techniques' have been used to enhance carbon fiber and carbon/carbon (C/C) composite oxidation resistance for over half a decade[243]. However, SiC coatings[244] tend to exhibit cracking during thermal cycling due to differences in thermal expansion coefficients while boron based[245, 246] 'composite techniques' negatively impact the thermal conductivity of the fiber. Considering that thermal stability is enhanced through surface modification or enhanced structural perfection, and the drawbacks associated with surface modification, improved thermal stability achieved through structural perfection enhancement is preferred. Further illustration of the effect of tensile modulus on thermal stability is shown by the oxidation activation energy of the standard modulus PAN based

T-300 carbon fiber and HOPG which have been experimentally determined to be 22.5 kcal/mol[247] (94 kJ/mol) and 47-53 kcal/mol[238] (197-222 kJ/mol).

B.2 Experimental

B.2.1 Precursor fiber spinning and drawing

The custom-designed small-scale spinning/drawing machine (Hills, Inc.) was used to process precursor fibers. The spinning machine consists of solution tank, metering pump (3 cm^3/rev), spinneret (100 holes with 200 μm hole diameter), gelation bath, and take-up winder. The drawing machine includes unwinding station, 4 sets of drawing rollers (2 rollers for 1 set, and the 3rd and 4th sets of rollers can be heated), 2 sets of spin-finish application setup, dryer, and take-up winder. The detailed spinning and drawing conditions for this particular study are listed in Table B. 1. The precursor fiber properties (tensile and structural) are also listed in Table B. 1.

Table B. 1 Processing conditions of precursor fiber spinning and drawing.

		101S1D1	128S2D2	88S1D2	121S1D2
Materials		PAN	PAN	PAN/FWNT	PAN/MWNT
Solution concentration (g/dL)		10	10	10.5	10.5
CNT concentration (wt%)		-	-	1.0	0.5
Temperature (°C)[1]		75 / 75 / 85	75 / 75 / 85	75 / 95 / 85	75 / 95 / 85
Gelation bath / temperature		Methanol / -50 °C	Methanol / -50 °C	Methanol / -50 °C	Methanol / -50 °C
Air gap (mm)		19	19	19	19
Spin draw ratio		3	3	3	3
Gelation time/temperature/medium		2 days / -40 °C / methanol	2 days / -40 °C / methanol	2 days / -40 °C / methanol	2 days / -40 °C / methanol
Post-spin draw ratio[2]		8.2	8.2	8.2	8.2
Effective diameter (μm)		11.6 ± 0.7	11.0 ± 0.8	12.1 ± 0.8	12.2 ± 1.0
Tensile properties[3]	Strength (GPa)	0.9 ± 0.2	1.0 ± 0.1	0.9 ± 0.1	0.8 ± 0.1
	Modulus (GPa)	20.2 ± 0.7	20.2 ± 1.1	19.0 ± 0.8	17.8 ± 0.9
	Elongation at break (%)	9.4 ± 1.5	N/A	10.4 ± 1.4	N/A
WAXD analysis[4]	d-spacing110 (nm)	0.530	0.527	0.526	0.525
	Crystallinity (%)	62	64	64	66
	Crystal size (nm)	17.4	15.7	16.2	14.1
	FWHM ()	5.5	6.7	6.4	5.3

[1]The temperatures listed are those of the solution tank, spin head, and spinneret jacket, respectively.

[2]Post-spin drawing was conducted in three-steps including cold drawing (CDR) and hot drawings (HDR, at two different temperatures). Temperatures for CDR, HDR1, and HDR2 were room temperature, 110 and 185 °C, respectively. Spin-finish oil (Matsumoto Yushi-Seiyaku Co., Ltd., Osaka, Japan) was applied before HDR1 and HDR2. After drawing, precursor tow was dried using hot air dryer at 130 °C.

[3]Tensile properties were measured at 25.4 mm gauge length at a strain rate of 1 %/s.

[4]Bragg equation was used to calculate the d-spacing of (110) peak from the equatorial scan. Crystallinity was calculated by peak fitting method from the integrated scan. Crystal size was calculated based on Scherrer's equation. Full width at half maximum intensity (FWHM) of azimuthal scan at $2\theta \sim 17°$ (110 peak).

B.2.2 Continuous stabilization and carbonization

The precursor fiber tows were converted into carbon fiber using small scale continuous stabilization/carbonization equipment (Harper International), which consists of multiple stabilization ovens with multiple tension control driving units along with low-temperature (LT) and high-temperature (HT) carbonization furnaces. The processing conditions listed in Table B. 2 are the conditions that produced best tensile properties for a given precursor fiber. In addition, the tensile and structural properties of the carbonized fibers are also listed in Table B. 2. For comparison, those of the commercial carbon fiber (IM7) are measured under the same testing condition and listed in Table B. 2.

Table B. 2 Stabilization and carbonization conditions, tensile properties, and structural parameters of the GT-processed carbon fibers. For comparison, tensile properties and structural parameters of the commercial carbon fiber (IM7) are also listed.

		Processing conditions and properties of the GT-processed carbon fibers					IM7	
		101S1D1-T163DHT	128S2D2-T188DHT	128S2D2-T188GHT	88S1D2-T131CHT	121S1D2-T174CHT	Tested at GT	Manufacturer reported
Stabilization	Temperature (°C)	180 – 250	180-250	180-250	180-250	200-275	N/A	
Low temp. carbonization	Temperature (°C)	500-675	500-675	500-675	500-675	500-675		
High temp. carbonization	Temperature (°C)	1450	1450	1450	1450	1450		
Tensile properties	Gauge length (mm)	25.4	25.4	25.4	25.4	25.4	25.4	N/A
	Effective diameter (μm)	5.1 ± 0.3	5.2 ± 0.3	5.0 ± 0.3	5.8 ± 0.3	6.4 ± 0.4	5.2 ± 0.2	5.2
	Strength (GPa)	5.1 ± 1.4	5.8 ± 1.4	5.6 ± 1.3	3.3 ± 0.8	4.0 ± 0.9	5.5 ± 0.8	5.5
	Modulus (GPa)	356	357	362	319	339	281	276
	Elongation at break (%)	1.51 ± 0.38	1.70 ± 0.39	1.64 ± 0.34	1.13 ± 0.26	1.28 ± 0.25	2.08 ± 0.28	1.90
WAXD analysis	d_{002} (nm)	0.347	0.345	0.344	0.350	0.347	0.348	N/A
	L_{002} (nm)	1.77	1.86	1.83	1.87	1.76	1.57	
	L_{10} (nm)	2.18	2.30	2.49	2.33	2.29	1.94	
	$FWHM_{Azimuthal\ scan,\ 2\theta\sim26°}$ (°)	24.7	25.4	25.8	25.3	26.4	30.3	

B.2.3 Characterization

Thermal stability of PAN and PAN/CNT based carbon fibers was performed on a Q500 TGA (TA Instruments) by heating 0.85 ± 0.08 mg of fiber from 30 ℃ to 1000 ℃ at a heating rate of 10 ℃/min using an air flow rate of 25 mL/min. Oxidation activation energy was determined by heating 0.85 ± 0.08 mg of fiber from 30 ℃ to 900 ℃ at 50 ℃/min and holding isothermally for 5 min under a nitrogen flow rate of 25 mL/min. Sample was then cooled to the predetermined isothermal temperature (600 – 800 ℃) and allowed to equilibrate before switching off the nitrogen flow and filling the sample chamber with air at a flow rate of 25 mL/min. Samples were held isothermally until all fiber was degraded. Oxidation rate for each temperature was determined by taking the slope of the weight loss curve from 25% - 75%.

B.3 Results and Discussion

B.3.1 Thermal Stability

Rapid weight loss of PAN based carbon fibers due to oxidation occurs above a critical temperature, which has been shown to increase as the structural perfection improves[242], supporting a relationship between carbon fiber modulus and oxidation resistance[240]. Figure B. 1 plots the thermal stability of the PAN and PAN/CNT based carbon fibers under an air flow rate of 25 mL/min at a heating rate of 10 ℃/min. Gel-spun PAN and PAN/CNT based carbon fibers exhibit an 80-130 ℃ increase in thermal stability as compared to IM7 at 50% weight loss.
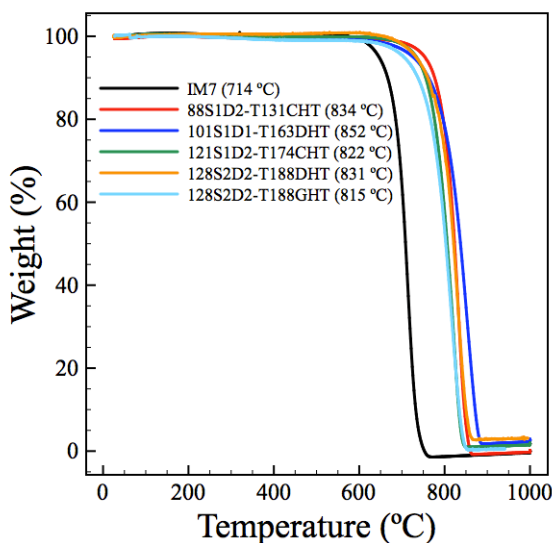
Figure B. 1 Thermogravimetric analysis of weight loss curves for PAN and PAN/CNT based carbon fibers. Temperature listed for each fiber is its onset degradation temperature (T_d).

B.3.2 Oxidation Activation Energy

Figure B. 2 is an Arrhenius plot of the oxidation reaction rate as a function of temperature of the IM7 and gel spun PAN based carbon fiber. Oxidation activation energy was calculated to be 110.7 and 162.4 kJ/mol for the IM7 and gel spun PAN based carbon fiber, respectively. Similar experiments for PAN based T-300 carbon fiber and highly ordered pyrolytic graphite resulted in oxidation activation energies of 22.4 kcal/mol (93.7 kJ/mol)[247] and 47-53 kcal/mol (196.6 – 221.8 kJ/mol)[238], respectively
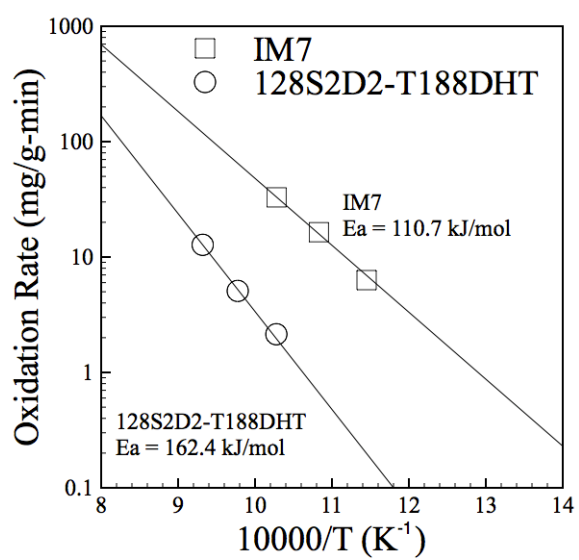
Figure B. 2 Arrhenius plots of IM7 and gel spun PAN based carbon fibers.

Appendix C
RAMAN SPECTROSCOPY OF PAN AND PAN/CNT BASED CARBON FIBERS

C.1 Introduction

Raman spectroscopy has previously been utilized as a technique to confirm the presence of graphitic templating in PAN/CNT based carbon fibers[37, 47, 103, 113]. Raman spectra below were collected using a Horiba Raman microscope with $\lambda = 785$ nm, 50x objective, laser power of ~ 6 mW, in the VV mode. Fiber angles of 0° and 90° to the polarization direction were used to collect spectra for each fiber. Figure D.1a and D.1b provide the Raman spectra of commercial carbon fibers T300 and IM7. Figure D.2a and D.2b provide the Raman spectra of gel spun PAN and PAN/CNT based carbon fibers.
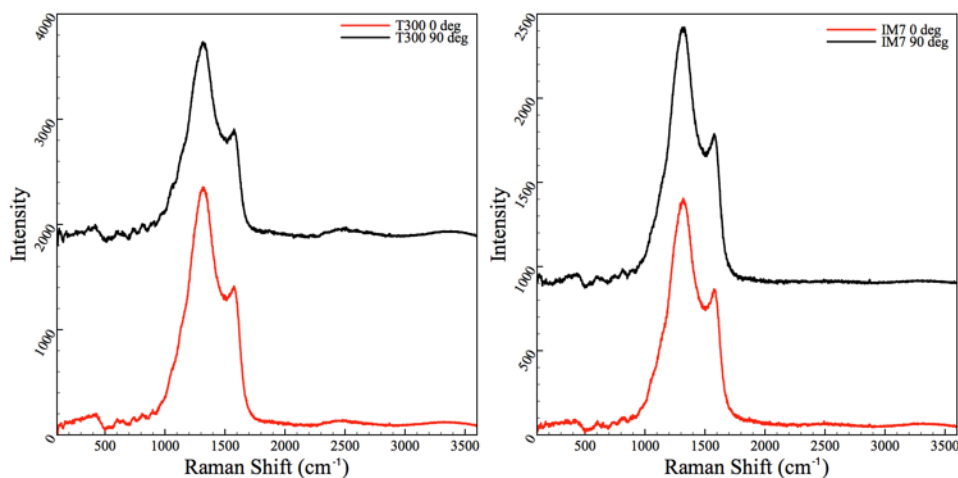
Figure C. 1 Raman spectra of commercial (a) T300 and (b) IM7 carbon fibers.
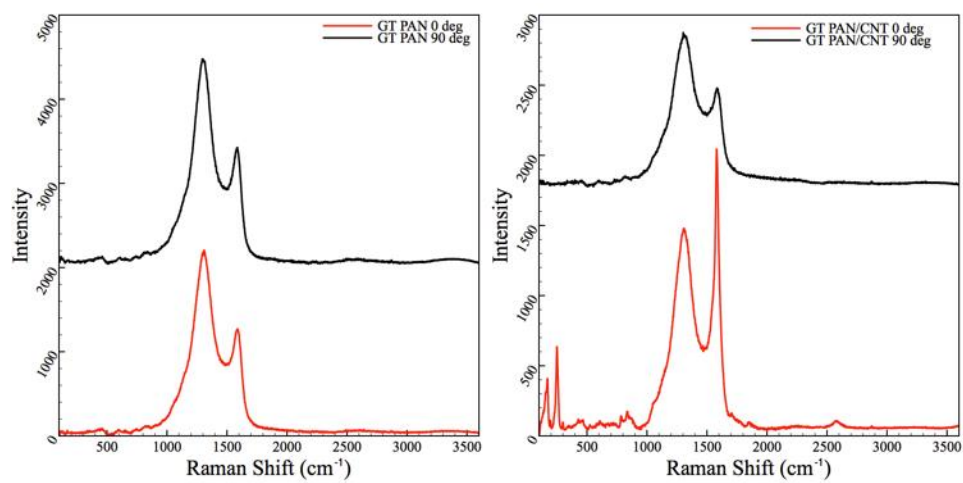
Figure C. 2 Raman spectra of gel spun (a) PAN and (b) PAN/CNT based carbon fibers.

Appendix D
SUPPLEMENTAL TABLES

Table D. 1 GT Sample ID for each polymer solution prepared in Chapter 2.

Sample ID in Chapter 2	GT Sample ID
Control	129R
Sample A	101
Sample B	105
Sample C	109
Sample D	112
Sample E	120
Sample F	140
Sample G	125
Sample H	128
Sample I	133
Sample J	136

Table D. 2 GT Sample ID for each as spun fiber prepared in Chapter 3.

Sample ID in Chapter 3	GT Sample ID
As Spun Sample A	25S2
As Spun Sample B	26S2
As Spun Sample C	36S1
As Spun Sample D	18R2S2
As Spun Sample E	73S3
As Spun Sample F	73S2
As Spun Sample G	35S1
As Spun Sample H	37S1
As Spun Sample I	37S2
As Spun Sample J	64S1
As Spun Sample K	67S1
As Spun Sample L	77S2
As Spun Sample M	122S1

Table D. 3 GT Sample ID for each precursor fiber prepared in Chapter 3.

Sample ID in Chapter 3	GT Sample ID
Precursor A	25S2D2
Precursor B	26S2D4
Precursor C	36S1D2
Precursor D	18R2S2D2D3
Precursor E	73S3D2
Precursor F	73S2D2
Precursor G	35S1D3
Precursor H	37S1D2
Precursor I	37S2D1
Precursor J	64S1D3
Precursor K	67S1D1
Precursor L	77S2D2
Precursor M	122S1D1

Table D. 4 GT Sample ID for each carbon fiber prepared in Chapter 3.

Sample ID in Chapter 3	GT Sample ID
Carbon Fiber A	25S2D2-T30DHT
Carbon Fiber A_1	128S2D2-T188DHT
Carbon Fiber A_2	128S2D2-T188GHT
Carbon Fiber E	73S3D2-T104CHT
Carbon Fiber H	37S1D2-T168CHT
Carbon Fiber I	37S2D1-T180AHT
Carbon Fiber K	67S1D1-T167AHT
Carbon Fiber L	77S2D2-T118CHT
Carbon Fiber M	122S1D1-T178AHT

Table D. 5 GT Sample ID for each as spun and precursor fiber prepared in Chapter 4.

Sample ID in Chapter 4	GT Sample ID
As Spun PAN	25S2
Drawn PAN	25S2D2
As Spun PAN/CNT-A	36S1
Drawn PAN/CNT-A	36S1D2
Drawn PAN/CNT-A(0.1)	26S1D5
Drawn PAN/CNT-B	29S1D2

Table D. 6 GT Sample ID for each carbon fiber prepared in Chapter 5.

Sample ID in Chapter 5	GT Sample ID
GT PAN	25S2D2-T30DHT
GT PAN/CNT-A (0.42 wt%)	32S1D1-T46DHT
GT PAN/CNT-A (1 wt%)	36S1D2-T51BHT
GT PAN/CNT-B1 (0.5 wt%)	18R2S2D2D3-T24HHT
GT PAN/CNT-B2 (0.5 wt%)	18R2S1S2D1-T169BHT
GT PAN/CNT-C (0.5 wt%)	121S1D2-T174CHT

REFERENCES:

1.   Minus, M. L.; Kumar, S., The processing, properties, and structure of carbon fibers. *Journal of Materials* **2005,** *57* (2), 52-58.
2.   Wade, B.; Knorr, R., Polymerization. In *Acrylic Fiber Technology and Applications*, Masson, J. C., Ed. Marcel Dekker, Inc.: New York, 1995; pp 37-67.
3.   Berger, K. C., Polymer handbook. 3rd ed.; Brandrup, J.; Immergut, E. H., Eds. Wiley: New York, 1989; pp 94-133.
4.   Bajaj, P.; Paliwal, D. K.; Gupta, A. K., Acrylonitrile acrylic acids copolymers 1. Synthesis and characterization. *Journal of Applied Polymer Science* **1993,** *49* (5), 823-833.
5.   Peebles, L. H., Branching in polyacrylonitrile. *Journal of the American Chemical Society* **1958,** *80* (21), 5603-5607.
6.   Ulbricht, J., Homogeneous polymerization of acrylonitrile in inorganic and organic solvents. *Journal of Polymer Science Part C-Polymer Symposium* **1968,** (16PC), 3747-&.
7.   Patron, L.; Bastianelli, U., *Applied Polymer Symposia* **1974,** *25*, 105.
8.   Ayrey, G.; Chadda, S. K.; Poller, R. C., The degradation and stabilization of polyacrylonitrile. I. Evidence for β-ketonitrile defect structures as initiators of degradation. *Journal of Polymer Science: Polymer Chemistry Edition* **1982,** *20* (8), 2249-2258.
9.   Bajaj, P., Acrylic Fibers. In *Manufactured Fibre Technology*, Gupta, V. B.; Kothari, V. K., Eds. Chapman & Hall: London, 1997; pp 406-456.
10.   Gupta, D. C.; Agrawal, J. P., Effect of comonomers on thermal-degradation of polyacrylonitrile. *Journal of Applied Polymer Science* **1989,** *38* (2), 265-270.
11.   Brandrup, J.; Immergut, E. H.; Grulke, E. A.; Abe, A.; Bloch, D. R., Polymer Handbook (4th Edition). John Wiley & Sons.
12.   Frushour, B. G.; Knorr, R. S., Acrylic Fibers. In *Handbook of Fiber Science: Vol. IV, Chemistry*, Lewin, M.; Pearce, E. M., Eds. Marcel Dekker: New York, 1985; Vol. IV.
13.   Frushour, B. G., Melting behavior of polyacrylonitrile copolymers. *Polymer Bulletin* **1984,** *11* (4), 375-382.
14.   Lathan, R. G. 2,404,714, 1946.
15.   Yamane, A.; Sawai, D.; Kameda, T.; Kanamoto, T.; Ito, M.; Porter, R. S., Development of high ductility and tensile properties upon two-stage draw of ultrahigh molecular weight poly(acrylonitrile). *Macromolecules* **1997,** *30* (14), 4170-4178.
16.   Sawai, D.; Yamane, A.; Takahashi, H.; Kanamoto, T.; Ito, M.; Porter, R. S., Development of high ductility and tensile properties by a two-stage draw of poly(acrylonitrile): Effect of molecular weight. *Journal of Polymer Science Part B-Polymer Physics* **1998,** *36* (4), 629-640.
17.   Sawai, D.; Yamane, A.; Kameda, T.; Kanamoto, T.; Ito, M.; Yamazaki, H.; Hisatani, K., Uniaxial drawing of isotactic poly(acrylonitrile): Development of oriented structure and tensile properties. *Macromolecules* **1999,** *32* (17), 5622-5630.
18.   Sawai, D.; Fujii, Y.; Kanamoto, T., Development of oriented morphology and tensile properties upon superdawing of solution-spun fibers of ultra-high molecular weight poly(acrylonitrile). *Polymer* **2006,** *47* (12), 4445-4453.
19.   Knudsen, J. P., The Influence of Coagulation Variables on the Structure and Physical Properties of an Acrylic Fiber. *Textile Research Journal* **1963,** *33* (1), 13-20.

20.   Paul, D. R., Diffusion during coagulation step of wet-spinning. *Journal of Applied Polymer Science* **1968,** *12* (3), 383-402.

21.   Paul, D. R., A study of the spinnability in wet-spinning of acrylic fibers. *Journal of Applied Polymer Science* **1968,** *12* (10), 2273-2298.

22.   Paul, D. R., Spin orientation during acrylic fiber formation by wet-spinning. *Journal of Applied Polymer Science* **1969,** *13* (5), 817-&.

23.   Paul, D. R.; McPeters, A. L., Effect of spin orientation on drawing of wet-spun fibers. *Journal of Applied Polymer Science* **1977,** *21* (6), 1699-1713.

24.   Huang, Y.; Young, R. J., Effect of Fiber Microstructure Upon the Modulus of PAN-and Pitch-Based Carbon-Fibers. *Carbon* **1995,** *33* (2), 97-107.

25.   Chae, H. G.; Minus, M. L.; Kumar, S., Oriented and exfoliated single wall carbon nanotubes in polyacrylonitrile. *Polymer* **2006,** *47* (10), 3494-3504.

26.   Mahmod, D. S. A.; Ismail, A. F.; Mustafa, A.; Ng, B. C.; Abdullah, M. S., Effect of the Solvent Type on the Formation and Physical Properties of Polyacrylonitrile Fibers via a Solvent-Free Coagulation Bath. *Journal of Applied Polymer Science* **2011,** *121* (4), 2467-2472.

27.   Baojun, Q.; Ding, P.; Zhenqiou, W., The Mechanism and Characteristics of Dry-Jet Wet-Spinning of Acrylic Fibers. *Advances in Polymer Technology* **1986,** *6* (4), 20.

28.   Dong, X.-G.; Wang, C.-G.; Bai, Y.-J.; Cao, W.-W., Effect of DMSO/H2O coagulation bath on the structure and property of polyacrylonitrile fibers during wet-spinning. *Journal of Applied Polymer Science* **2007,** *105* (3), 1221-1227.

29.   Bajaj, P.; Sreekumar, T. V.; Sen, K., Structure development during dry-jet-wet spinning of acrylonitrile/vinyl acids and acrylonitrile/methyl acrylate copolymers. *Journal of Applied Polymer Science* **2002,** *86* (3), 773-787.

30.   Wang, Y. X.; Wang, C. G.; Yu, M. J., Effects of Different Coagulation Conditions on Polyacrylonitrile Fibers Wet Spun in a System of Dimethylsulphoxide and Water. *Journal of Applied Polymer Science* **2007,** *104*, 3723-3729.

31.   Ji, B.-H.; Wang, C.-G.; Wang, Y.-X., Effect of jet stretch on polyacrylonitrile as-spun fiber formation. *Journal of Applied Polymer Science* **2007,** *103* (5), 3348-3352.

32.   Larson, R. G., *The structure and rheology of complex fluids / Ronald G. Larson*. New York : Oxford University Press, 1999.: 1999.

33.   Sreekumar, T. V.; Liu, T.; Min, B. G.; Guo, H.; Kumar, S.; Hauge, R. H.; Smalley, R. E., Polyacrylonitrile single-walled carbon nanotube composite fibers. *Advanced Materials* **2004,** *16* (1), 58-61.

34.   Chae, H.; Sreekumar, T.; Uchida, T.; Kumar, S., A comparison of reinforcement efficiency of various types of carbon nanotubes in polyacrylonitrile fiber. *Polymer* **2005,** *46* (24), 10925-10935.

35.   Jain, R.; Minus, M. L.; Chae, H. G.; Kumar, S., Processing, Structure, and Properties of PAN/MWNT Composite Fibers. *Macromolecular Materials and Engineering* **2010,** *295* (8), 742-749.

36.   Liu, Y. D.; Chae, H. G.; Kumar, S., Gel-spun carbon nanotubes/polyacrylonitrile composite fibers. Part I: Effect of carbon nanotubes on stabilization. *Carbon* **2011,** *49* (13), 4466-4476.

37.   Prilutsky, S.; Zussman, E.; Cohen, Y., The effect of embedded carbon nanotubes on the morphological evolution during the carbonization of poly(acrylonitrile) nanofibers. *Nanotechnology* **2008,** *19* (16).

38.   Liu, J.; Wang, T.; Uchida, T.; Kumar, S., Carbon nanotube core-polymer shell nanofibers. *Journal of Applied Polymer Science* **2005,** *96* (5), 1992-1995.

39.   Frankland, S. J. V.; Caglar, A.; Brenner, D. W.; Griebel, M., Molecular simulation of the influence of chemical cross-links on the shear strength of carbon nanotube-polymer interfaces. *Journal of Physical Chemistry B* **2002,** *106* (12), 3046-3048.

40.   Liao, K.; Li, S., Interfacial characteristics of a carbon nanotube-polystyrene composite system. *Applied Physics Letters* **2001,** *79* (25), 4225-4227.

41.   Gou, J. H.; Minaie, B.; Wang, B.; Liang, Z. Y.; Zhang, C., Computational and experimental study of interfacial bonding of single-walled nanotube reinforced composites. *Computational Materials Science* **2004,** *31* (3-4), 225-236.

42.   Barber, A. H.; Cohen, S. R.; Wagner, H. D., Measurement of carbon nanotube-polymer interfacial strength. *Applied Physics Letters* **2003,** *82* (23), 4140-4142.

43.   Tsuda, T.; Ogasawara, T.; Deng, F.; Takeda, N., Direct measurements of interfacial shear strength of multi-walled carbon nanotube/PEEK composite using a nano-pullout method. *Composites Science and Technology* **2011,** *71* (10), 1295-1300.

44.   Ozkan, T.; Chen, Q.; Chasiotis, I., Interfacial strength and fracture energy of individual carbon nanofibers in epoxy matrix as a function of surface conditions. *Composites Science and Technology* **2012,** *72* (9), 965-975.

45.   Chen, X.; Zheng, M.; Park, C.; Ke, C., Direct Measurements of the Mechanical Strength of Carbon Nanotube–Poly(methyl methacrylate) Interfaces. *Small* **2013**, n/a-n/a.

46.   Barber, A. H.; Cohen, S. R.; Kenig, S.; Wagner, H. D., Interfacial fracture energy measurements for multi-walled carbon nanotubes pulled from a polymer matrix. *Composites Science and Technology* **2004,** *64* (15), 2283-2289.

47.   Papkov, D.; Beese, A. M.; Goponenko, A.; Zou, Y.; Naraghi, M.; Espinosa, H. D.; Saha, B.; Schatz, G. C.; Moravsky, A.; Loutfy, R.; Nguyen, S. T.; Dzenis, Y., Extraordinary Improvement of the Graphitic Structure of Continuous Carbon Nanofibers Templated with Double Wall Carbon Nanotubes. *ACS Nano* **2013,** *7* (1), 126-142.

48.   Wagner, H. D.; Lourie, O.; Feldman, Y.; Tenne, R., Stress-induced fragmentation of multiwall carbon nanotubes in a polymer matrix. *Applied Physics Letters* **1998,** *72* (2), 188-190.

49.   Roy, D.; Bhattacharyya, S.; Rachamim, A.; Plati, A.; Saboungi, M. L., Measurement of interfacial shear strength in single wall carbon nanotubes reinforced composite using Raman spectroscopy. *Journal of Applied Physics* **2010,** *107* (4).

50.   Robinson, I. M.; Zakikhani, M.; Day, R. J.; Young, R. J.; Galiotis, C., Strain dependence of the Raman frequencies for different types of carbon fibers. *Journal of Materials Science Letters* **1987,** *6* (10), 1212-1214.

51.   Galiotis, C.; Robinson, I. M.; Young, R. J.; Smith, B. J. E.; Batchelder, D. N., Strain dependence of the Raman frequencies of a Kevlar-49 fiber. *Polymer Communications* **1985,** *26* (12), 354-355.

52.   Cronin, S. B.; Swan, A. K.; Unlu, M. S.; Goldberg, B. B.; Dresselhaus, M. S.; Tinkham, M., Measuring the uniaxial strain of individual single-wall carbon nanotubes: Resonance Raman spectra of atomic-force-microscope modified single-wall nanotubes. *Physical Review Letters* **2004,** *93* (16).

53.   Cronin, S. B.; Swan, A. K.; Unlu, M. S.; Goldberg, B. B.; Dresselhaus, M. S.; Tinkham, M., Resonant Raman spectroscopy of individual metallic and semiconducting single-wall carbon nanotubes under uniaxial strain. *Physical Review B* **2005,** *72* (3).

54.   Chang, C. C.; Hsu, I. K.; Aykol, M.; Hung, W. H.; Chen, C. C.; Cronin, S. B., A New Lower Limit for the Ultimate Breaking Strain of Carbon Nanotubes. *ACS Nano* **2010,** *4* (9), 5095-5100.

55.   Kumar, R.; Cronin, S. B., Raman scattering of carbon nanotube bundles under axial strain and strain-induced debundling. *Physical Review B* **2007,** *75* (15).

56.   Huong, P. V.; Cavagnat, R.; Ajayan, P. M.; Stephan, O., Temperature-Dependent Vibrational-Spectra of Carbon Nanotubes. *Physical Review B* **1995,** *51* (15), 10048-10051.

57.   Vigolo, B.; Penicaud, A.; Coulon, C.; Sauder, C.; Pailler, R.; Journet, C.; Bernier, P.; Poulin, P., Macroscopic fibers and ribbons of oriented carbon nanotubes. *Science* **2000,** *290* (5495), 1331-1334.

58.   Behabtu, N.; Green, M. J.; Pasquali, M., Carbon nanotube-based neat fibers. *Nano Today* **2008,** *3* (5-6), 24-34.

59.   Sun, G.; Zheng, L.; Zhou, J.; Zhang, Y.; Zhan, Z.; Pang, J. H. L., Load-transfer efficiency and mechanical reliability of carbon nanotube fibers under low strain rates. *International Journal of Plasticity* **2013,** *40* (0), 56-64.

60.   Lourie, O.; Wagner, H. D., Evaluation of Young's modulus of carbon nanotubes by micro-Raman spectroscopy. *Journal of Materials Research* **1998,** *13* (9), 2418-2422.

61.   Schadler, L. S.; Giannaris, S. C.; Ajayan, P. M., Load transfer in carbon nanotube epoxy composites. *Applied Physics Letters* **1998,** *73* (26), 3842-3844.

62.   Ajayan, P. M.; Schadler, L. S.; Giannaris, C.; Rubio, A., Single-walled carbon nanotube-polymer composites: Strength and weakness. *Advanced Materials* **2000,** *12* (10), 750-+.

63.   Cooper, C. A.; Young, R. J.; Halsall, M., Investigation into the deformation of carbon nanotubes and their composites through the use of Raman spectroscopy. *Composites Part a-Applied Science and Manufacturing* **2001,** *32* (3-4), 401-411.

64.   Wong, K. K. H.; Zinke-Allmang, M.; Hutter, J. L.; Hrapovic, S.; Luong, J. H. T.; Wan, W., The effect of carbon nanotube aspect ratio and loading on the elastic modulus of electrospun poly(vinyl alcohol)-carbon nanotube hybrid fibers. *Carbon* **2009,** *47* (11), 2571-2578.

65.   Wood, J. R.; Zhao, Q.; Wagner, H. D., Orientation of carbon nanotubes in polymers and its detection by Raman spectroscopy. *Composites Part a-Applied Science and Manufacturing* **2001,** *32* (3-4), 391-399.

66.   Frogley, M. D.; Zhao, Q.; Wagner, H. D., Polarized resonance Raman spectroscopy of single-wall carbon nanotubes within a polymer under strain. *Physical Review B* **2002,** *65* (11).

67.   Deng, L. B.; Eichhorn, S. J.; Kao, C. C.; Young, R. J., The Effective Young's Modulus of Carbon Nanotubes in Composites. *ACS Applied Materials & Interfaces* **2011,** *3* (2), 433-440.

68.   Liu, L. Q.; Ma, W. J.; Zhang, Z., Macroscopic Carbon Nanotube Assemblies: Preparation, Properties, and Potential Applications. *Small* **2011,** *7* (11), 1504-1520.

69.   Qian, D.; Liu, W. K.; Ruoff, R. S., Load transfer mechanism in carbon nanotube ropes. *Composites Science and Technology* **2003,** *63* (11), 1561-1569.

70.   Yakobson, B. I.; Samsonidze, G.; Samsonidze, G. G., Atomistic theory of mechanical relaxation in fullerene nanotubes. *Carbon* **2000,** *38* (11-12), 1675-1680.

71.   Vilatela, J. J.; Elliott, J. A.; Windle, A. H., A Model for the Strength of Yarn-like Carbon Nanotube Fibers. *ACS Nano* **2011,** *5* (3), 1921-1927.

72.   Motta, M.; Li, Y. L.; Kinloch, I.; Windle, A., Mechanical properties of continuously spun fibers of carbon nanotubes. *Nano Letters* **2005,** *5* (8), 1529-1533.

73.   Chae, H. G.; Kumar, S., Materials science - Making strong fibers. *Science* **2008,** *319* (5865), 908-909.

74.   Liu, Y.; Kumar, S., Recent Progress in Fabrication, Structure, and Properties of Carbon Fibers. *Polymer Reviews* **2012,** *52* (3-4), 234-258.

75.   Dainton, F. S.; Eaton, R. S., The polymerization of acrylonitrile in aqueous solution. Part 3. The ferric ion-photosensitized reaction at 15, 25, 30, and 50 °C. *Journal of Polymer Science* **1959,** *39* (135), 313-320.

76.   Heyn, A. N. J., Electron microscope observations on microgel and linear macromolecules for polyacrylonitrile. *Journal of Polymer Science* **1959,** *41* (138), 23-32.

77.   Lyoo, W. S.; Kim, B. C.; Ha, W. S., Rheological and rheo-optical properties of high molecular weight syndiotactic and atactic polyvinylalcohol solutions. *Polymer Engineering and Science* **1997,** *37* (7), 1259-1265.

78.   Lee, E. J.; Kim, N. H.; Dan, K. S.; Kim, B. C., Rheological properties of solutions of general-purpose poly(vinyl alcohol) in dimethyl sulfoxide. *Journal of Polymer Science Part B-Polymer Physics* **2004,** *42* (8), 1451-1456.

79.   Chae, H. G.; Kim, B. C.; Im, S. S.; Han, Y. K., Effect of molecular weight and branch structure on the crystallization and rheological properties of poly(butylene adipate). *Polymer Engineering and Science* **2001,** *41* (7), 1133-1139.

80.   Yoon, P. J.; Han, C. D., Effect of thermal history on the rheological behavior of thermoplastic polyurethanes. *Macromolecules* **2000,** *33* (6), 2171-2183.

81.   Chuang, H. K.; Han, C. D., Rheological behavior of polymer blends. *Journal of Applied Polymer Science* **1984,** *29* (6), 2205-2229.

82.   Han, C. D.; Chuang, H. K., Blends of nylon-6 with an ethylene based multifunction polyer. 1. Rheology-structure relationships. *Journal of Applied Polymer Science* **1985,** *30* (6), 2431-2455.

83.   Han, C. D.; Chuang, H. K., Criterea for rheological compatability of polymer blends. *Journal of Applied Polymer Science* **1985,** *30* (11), 4431-4454.

84.   Hong, S. M.; Kim, B. C.; Hwang, S. S.; Kim, K. U., Rheological and physical properties of polyacrylate/LCP blend systems. *Polymer Engineering and Science* **1993,** *33* (10), 630-639.

85.   Han, C. D.; Kim, J., Rheological technique for determining the order-disorder transition of block copolymers. *Journal of Polymer Science Part B-Polymer Physics* **1987,** *25* (8), 1741-1764.

86.   Han, C. D.; Kim, J. W.; Kim, J. K., Determination of the order-disorder transition temperature of block copolymers. *Macromolecules* **1989,** *22* (1), 383-394.

87.   Lee, K. M.; Han, C. D., Linear dynamic viscoelastic properties of functionalized block copolymer/organoclay nanocomposites. *Macromolecules* **2003,** *36* (3), 804-815.

88.   Wu, D. F.; Zhou, C. X.; Hong, Z.; Mao, D. L.; Bian, Z., Study on rheological behaviour of poly(butylene terephthalate)/montmorillonite nanocomposites. *European Polymer Journal* **2005,** *41* (9), 2199-2207.

89.   Chae, D. W.; Lee, K. H.; Kim, Y. C., Rheological properties of ferrite nanocomposites based on nylon-66. *Journal of Polymer Science Part B-Polymer Physics* **2006,** *44* (2), 371-377.

90.   Zhou, K.; Gu, S. Y.; Zhang, Y. H.; Ren, J., Effect of dispersion on rheological and mechanical properties of polypropylene/carbon nanotubes nanocomposites. *Polymer Engineering and Science* **2012,** *52* (7), 1485-1494.

91.   Choi, Y. J.; Hwang, S. H.; Hong, Y. S.; Kim, J. Y.; Ok, C. Y.; Huh, W.; Lee, S. W., Preparation and characterization of PS/multi-walled carbon nanotube nanocomposites. *Polymer Bulletin* **2005,** *53* (5-6), 393-400.

92.   Wu, D.; Wu, L.; Sun, Y.; Zhang, M., Rheological properties and crystallization behavior of multi-walled carbon Nanotube/Poly(epsilon-caprolactone) composites. *Journal of Polymer Science Part B-Polymer Physics* **2007,** *45* (23), 3137-3147.

93.   Kim, S. S.; Han, C. D., Effect of molecular weight on the rheological behavior of thermotropic liquid crystalline polymer. *Macromolecules* **1993,** *26* (24), 6633-6642.

94.   Han, C. D.; Jhon, M. S., Correlation of the 1st normal stress difference with shear stress and of the storage modulus with loss modulus for homopolymers. *Journal of Applied Polymer Science* **1986,** *32* (3), 3809-3840.

95.   Han, C. D.; Kim, J. K., On the use of the time-temperature superposition in multicomponent multiphase polymer systems. *Polymer* **1993,** *34* (12), 2533-2539.

96.   Lyons, K. M.; Newcomb, B. A.; McDonald, K. J.; Chae, H. G.; Kumar, S., Development of single filament testing procedure for polyacrylonitrile precursor and polyacrylonitrile-based carbon fibers. *Journal of Composite Materials* **2014,** *0* (0), 1-10.

97.   Dealy, J. M.; Wissbrun, K. F., *Melt Rheology and its Role in Plastics Processing*. Springer: New York, 1990.

98.   Smith, P.; Lemstra, P. J.; Kalb, B.; Pennings, A. J., Ultrahigh-strength polyethylene filaments by solution spinning and hot drawing. *Polymer Bulletin* **1979,** *1* (11), 733-736.

99.   Cha, W. I.; Hyon, S. H.; Ikada, Y., Gel spinning of poly(vinyl alcohol) from dimethyl sulfoxide/water mixture. *Journal of Polymer Science Part B-Polymer Physics* **1994,** *32* (2), 297-304.

100.   Ruan, S. L.; Gao, P.; Yu, T. X., Ultra-strong gel-spun UHMWPE fibers reinforced using multiwalled carbon nanotubes. *Polymer* **2006,** *47* (5), 1604-1611.

101.   Minus, M. L.; Chae, H. G.; Kumar, S., Interfacial Crystallization in Gel-Spun Poly(vinyl alcohol)/Single-Wall Carbon Nanotube Composite Fibers. *Macromolecular Chemistry and Physics* **2009,** *210* (21), 1799-1808.

102.   Newcomb, B. A.; Chae, H. G.; Gulgunje, P.; Gupta, K.; Liu, Y. D.; Tsentalovich, D. E.; Pasquali, M.; Kumar, S., Stress transfer in polyacrylonitrile/carbon nanotube composite fibers. *Polymer* **2014,** *55* (11), 2734-2743.

103.   Chae, H. G.; Minus, M. L.; Rasheed, A.; Kumar, S., Stabilization and carbonization of gel spun polyacrylonitrile/single wall carbon nanotube composite fibers. *Polymer* **2007,** *48* (13), 3781-3789.

104.   Liu, Y. D.; Chae, H. G.; Kumar, S., Gel-spun carbon nanotubes/polyacrylonitrile composite fibers. Part III: Effect of stabilization conditions on carbon fiber properties. *Carbon* **2011,** *49* (13), 4487-4496.

105.   Sahin, K.; Fasanella, N. A.; Chasiotis, I.; Lyons, K. M.; Newcomb, B. A.; Kamath, M. G.; Chae, H. G.; Kumar, S., High strength micron size carbon fibers from polyacrylonitrile-carbon nanotube precursors. *Carbon* **2014,** *77*, 442-453.

106.   Bahrami, S. H.; Bajaj, P.; Sen, K., Effect of Coagulation Conditions on Properties of Poly(acrylonitrile-carboxylic acid) Fibers. *Journal of Polymer Science* **2003,** *89*, 12.

107.   Frushour, B. G., Acrylic Polymer Characterization in Solid State and Solution. In *Acrylic Fiber Technology and Applications*, Masson, J. C., Ed. Marcel Dekker, Inc.: New York, 1995; pp 197-257.

108.   Zeng, X. M.; Zhang, G.; Zhang, Y. W.; Zhao, J. X.; Pan, D., Diffusion mechanism of as-spun polyacrylonitrile fiber in a dimethyl sulfoxide-water coagulation bath. *Journal of Macromolecular Science Part a-Pure and Applied Chemistry* **2006,** *43* (11), 1711-1720.

109.   Lyons, K. M.; Newcomb, B. A.; McDonald, K. J.; Chae, H. G.; Kumar, S., Development of single filament testing procedure for polyacrylonitrile precursor and polyacrylonitrile-based carbon fibers. *Journal of Composite Materials* **2014**.

110.   Zhang, X. F.; Liu, T.; Sreekumar, T. V.; Kumar, S.; Moore, V. C.; Hauge, R. H.; Smalley, R. E., Poly(vinyl alcohol)/SWNT composite film. *Nano Letters* **2003,** *3* (9), 1285-1288.

111.   Deng, L. B.; Young, R. J.; van der Zwaag, S.; Picken, S., Characterization of the adhesion of single-walled carbon nanotubes in poly (p-phenylene terephthalamide) composite fibres. *Polymer* **2010,** *51* (9), 2033-2039.

112.   Chang, T. E.; Jensen, L. R.; Kisliuk, A.; Pipes, R. B.; Pyrz, R.; Sokolov, A. P., Microscopic mechanism of reinforcement in single-wall carbon nanotube/polypropylene nanocomposite. *Polymer* **2005,** *46* (2), 439-444.

113.   Chae, H. G.; Choi, Y. H.; Minus, M. L.; Kumar, S., Carbon nanotube reinforced small diameter polyacrylonitrile based carbon fiber. *Composites Science and Technology* **2009,** *69* (3-4), 406-413.

114.   Chiang, I. W.; Brinson, B. E.; Smalley, R. E.; Margrave, J. L.; Hauge, R. H., Purification and characterization of single-wall carbon nanotubes. *Journal of Physical Chemistry B* **2001,** *105* (6), 1157-1161.

115.   Vadillo, D. C.; Tuladhar, T. R.; Mulji, A. C.; Jung, S.; Hoath, S. D.; Mackley, M. R., Evaluation of the inkjet fluid's performance using the "Cambridge Trimaster" filament stretch and break-up device. *Journal of Rheology* **2010,** *54* (2), 261-282.

116.   Shaqfeh, E. S. G.; Fredrickson, G. H., The Hydrodynamic Stress in a Suspension of Rods. *Physics of Fluids a-Fluid Dynamics* **1990,** *2* (1), 7-24.

117.   Tsentalovich, D. E.; Lee, J. A.; Behabtu, N.; Ma, A. W. K.; Choi, A.; Luo, Y.; Young, C. C.; Pasquali, M., Measuring Carbon Nanotube Aspect Ratio with Capillary Thinning Extenstional Rheology (in preparation).

118.   Jain, R. Carbon Nanotube Reinforced Polyacrylonitrile and Poly(ether ketone) Fibers. PhD Dissertation, Georgia Institute of Technology, Atlanta, 2009.

119.   Basu-Dutt, S.; Minus, M. L.; Jain, R.; Nepal, D.; Kumar, S., Chemistry of Carbon Nanotubes for Everyone. *Journal of Chemical Education* **2012,** *89* (2), 221-229.

120.   Choi, Y. H. Polyacrylonitrile / carbon nanotube composite fibers: effect of various processing parameters on fiber structure and properties. PhD Dissertation, Georgia Institute of Technology, Atlanta, 2010.

121.   Yan, X.; Dong, H.; Liu, Y.; Newcomb, B. A.; Kumar, S.; Xiao, Z.; Liu, T., CNT bundle sizes of PAN/CNT composite solutions (To be published).

122.   Jones, W. J.; Thomas, D. K.; Thomas, D. W.; Williams, G., On the determination of order parameters for homogeneous and twisted nematic liquid crystals from Raman spectroscopy. *Journal of Molecular Structure* **2004,** *708* (1-3), 145-163.

123.   Long, D. A., *Raman Spectroscopy*. McGraw-Hill: New York, 1977.

124.   Liu, T.; Kumar, S., Quantitative characterization of SWNT orientation by polarized Raman spectroscopy. *Chemical Physics Letters* **2003,** *378* (3-4), 257-262.

125.   Niyogi, S.; Hamon, M. A.; Hu, H.; Zhao, B.; Bhowmik, P.; Sen, R.; Itkis, M. E.; Haddon, R. C., Chemistry of single-walled carbon nanotubes. *Accounts of Chemical Research* **2002,** *35* (12), 1105-1113.

126.   Xiao, K. Q.; Zhang, L. C., The stress transfer efficiency of a single-walled carbon nanotube in epoxy matrix. *Journal of Materials Science* **2004,** *39* (14), 4481-4486.

127. Ward, I. M.; Hadley, D. W., *An Introduction to the Mechanical Properties of Solid Polymers*. John Wiley & Sons: New York.

128. Liu, T.; Kumar, S., Effect of orientation on the modulus of SWNT films and fibers. *Nano Letters* **2003,** *3* (5), 647-650.

129. Yakobson, B. I.; Avouris, P., Mechanical Properties of Carbon Nanotubes. In *Carbon Nanotubes*, Dresselhaus, M.; Dresselhaus, G.; Avouris, P., Eds. Springer Berlin Heidelberg: 2001; Vol. 80, pp 287-327.

130. Salvetat, J. P.; Briggs, G. A. D.; Bonard, J. M.; Bacsa, R. R.; Kulik, A. J.; Stockli, T.; Burnham, N. A.; Forro, L., Elastic and shear moduli of single-walled carbon nanotube ropes. *Physical Review Letters* **1999,** *82* (5), 944-947.

131. Shen, L. X.; Li, J., Transversely isotropic elastic properties of multiwalled carbon nanotubes. *Physical Review B* **2005,** *71* (3).

132. Zhang, Y.; Song, K.; Meng, J.; Minus, M. L., Tailoring Polyacrylonitrile Interfacial Morphological Structure by Crystallization in the Presence of Single-Wall Carbon Nanotubes. *ACS Applied Materials & Interfaces* **2013,** *5* (3), 807-814.

133. Wang, W. J.; Murthy, N. S.; Chae, H. G.; Kumar, S., Structural changes during deformation in carbon nanotube-reinforced polyacrylonitrile fibers. *Polymer* **2008,** *49* (8), 2133-2145.

134. Heller, D. A.; Barone, P. W.; Swanson, J. P.; Mayrhofer, R. M.; Strano, M. S., Using Raman spectroscopy to elucidate the aggregation state of single-walled carbon nanotubes. *Journal of Physical Chemistry B* **2004,** *108* (22), 6905-6909.

135. Liu, T.; Xiao, Z. W.; Wang, B., The exfoliation of SWCNT bundles examined by simultaneous Raman scattering and photoluminescence spectroscopy. *Carbon* **2009,** *47* (15), 3529-3537.

136. O'Connell, M. J.; Sivaram, S.; Doorn, S. K., Near-infrared resonance Raman excitation profile studies of single-walled carbon nanotube intertube interactions: A direct comparison of bundled and individually dispersed HiPco nanotubes. *Physical Review B* **2004,** *69* (23).

137. Bachilo, S. M.; Strano, M. S.; Kittrell, C.; Hauge, R. H.; Smalley, R. E.; Weisman, R. B., Structure-assigned optical spectra of single-walled carbon nanotubes. *Science* **2002,** *298* (5602), 2361-2366.

138. Weisman, R. B.; Bachilo, S. M., Dependence of optical transition energies on structure for single-walled carbon nanotubes in aqueous suspension: An empirical Kataura plot. *Nano Letters* **2003,** *3* (9), 1235-1238.

139. Strano, M. S.; Doorn, S. K.; Haroz, E. H.; Kittrell, C.; Hauge, R. H.; Smalley, R. E., Assignment of (n, m) Raman and optical features of metallic single-walled carbon nanotubes. *Nano Letters* **2003,** *3* (8), 1091-1096.

140. Yang, L.; Han, J., Electronic structure of deformed carbon nanotubes. *Physical Review Letters* **2000,** *85* (1), 154-157.

141. Doorn, S. K.; Heller, D. A.; Barone, P. W.; Usrey, M. L.; Strano, M. S., Resonant Raman excitation profiles of individually dispersed single walled carbon nanotubes in solution. *Applied Physics a-Materials Science & Processing* **2004,** *78* (8), 1147-1155.

142. Cox, H. L., The Elasticity and Strength of Paper and other Fibrous Materials. *British Journal of Applied Physics* **1952,** *3* (MAR), 72-79.

143. Piggott, M. R., Debonding and friction at fiber polymer interfaces. 1: Criteria for failure and sliding. *Composites Science and Technology* **1987,** *30* (4), 295-306.

144.   Mehta, V. R.; Kumar, S., Temperature dependent torsional properties of high performance fibers and their relevance to compressive strength. *Journal of Materials Science* **1994,** *29* (14), 3658-3664.

145.   Hine, P. J.; Ward, I. M., Measuring the elastic properties of high-modulus fibres. *Journal of Materials Science* **1996,** *31* (2), 371-379.

146.   Warner, S. B., *Fiber science*. Englewood Cliffs, NJ : Prentice Hall, c1995.: 1995.

147.   Minus, M. L.; Chae, H. G.; Kumar, S., Polyethylene Crystallization Nucleated by Carbon Nanotubes under Shear. *ACS Applied Materials & Interfaces* **2012,** *4* (1), 326-330.

148.   Bhattacharyya, A. R.; Sreekumar, T. V.; Liu, T.; Kumar, S.; Ericson, L. M.; Hauge, R. H.; Smalley, R. E., Crystallization and orientation studies in polypropylene/single wall carbon nanotube composite. *Polymer* **2003,** *44* (8), 2373-2377.

149.   Li, C. Y.; Li, L. Y.; Cai, W. W.; Kodjie, S. L.; Tenneti, K. K., Nanohybrid Shish-kebabs: Periodically functionalized carbon nanotubes. *Advanced Materials* **2005,** *17* (9), 1198-1202.

150.   Anand, K. A.; Agarwal, U. S.; Joseph, R., Carbon nanotubes induced crystallization of poly(ethylene terephthalate). *Polymer* **2006,** *47* (11), 3976-3980.

151.   Minus, M. L.; Chae, H. G.; Kumar, S., Single wall carbon nanotube templated oriented crystallization of poly(vinyl alcohol). *Polymer* **2006,** *47* (11), 3705-3710.

152.   Edie, D. D., The effect of processing on the structure and properties of carbon fibers. *Carbon* **1998,** *36* (4), 345-362.

153.   Qiu, L.; Zheng, X. H.; Zhu, J.; Su, G. P.; Tang, D. W., The effect of grain size on the lattice thermal conductivity of an individual polyacrylonitrile-based carbon fiber. *Carbon* **2013,** *51* (0), 265-273.

154.   Torayca M60J Data Sheet. http://www.toraycfa.com/pdfs/M60JDataSheet.pdf (accessed October 1, 2014).

155.   Hexcel HexTow IM7 Carbon Fiber Product Data. http://www.hexcel.com/resources/datasheets/carbon-fiber-data-sheets/im7.pdf (accessed October 1, 2014).

156.   Oya, N.; Johnson, D. J., Longitudinal compressive behaviour and microstructure of PAN-based carbon fibres. *Carbon* **2001,** *39* (5), 635-645.

157.   Torayca Torayca T800H Data Sheet. http://www.toraycfa.com/pdfs/T800HDataSheet.pdf (accessed October 1, 2014).

158.   Prilutsky, S.; Zussman, E.; Cohen, Y., Carbonization of Electrospun Poly(acrylonitrile) Nanofibers Containing Multiwalled Carbon Nanotubes Observed by Transmission Electron Microscope with In Situ Heating. *Journal of Polymer Science Part B-Polymer Physics* **2010,** *48* (20), 2121-2128.

159.   Naito, K.; Yang, J.-M.; Xu, Y.; Kagawa, Y., Enhancing the thermal conductivity of polyacrylonitrile- and pitch-based carbon fibers by grafting carbon nanotubes on them. *Carbon* **2010,** *48* (6), 1849-1857.

160.   Nysten, B.; Issi, J. P.; Barton, R.; Boyington, D. R.; Lavin, J. G., Determination of lattice defects in carbon fibers by means of thermal-conductivity measurements. *Physical Review B* **1991,** *44* (5), 2142-2148.

161.   Zhang, X.; Fujiwara, S.; Fujii, M., Measurements of thermal conductivity and electrical conductivity of a single carbon fiber. *International Journal of Thermophysics* **2000,** *21* (4), 965-980.

162.   Maruyama, S., A molecular dynamics simulation of heat conduction in finite length SWNTs. *Physica B-Condensed Matter* **2002,** *323* (1-4), 193-195.

163. Zhang, G.; Li, B. W., Thermal conductivity of nanotubes revisited: Effects of chirality, isotope impurity, tube length, and temperature. *Journal of Chemical Physics* **2005,** *123* (11).

164. Cao, J. X.; Yan, X. H.; Xiao, Y.; Ding, J. W., Thermal conductivity of zigzag single-walled carbon nanotubes: Role of the umklapp process. *Physical Review B* **2004,** *69* (7), 073407.

165. Fujii, M.; Zhang, X.; Xie, H. Q.; Ago, H.; Takahashi, K.; Ikuta, T.; Abe, H.; Shimizu, T., Measuring the thermal conductivity of a single carbon nanotube. *Physical Review Letters* **2005,** *95* (6), 065502.

166. Shenogin, S.; Bodapati, A.; Xue, L.; Ozisik, R.; Keblinski, P., Effect of chemical functionalization on thermal transport of carbon nanotube composites. *Applied Physics Letters* **2004,** *85* (12), 2229-2231.

167. Yu, C. H.; Shi, L.; Yao, Z.; Li, D. Y.; Majumdar, A., Thermal conductance and thermopower of an individual single-wall carbon nanotube. *Nano Letters* **2005,** *5* (9), 1842-1846.

168. Mingo, N.; Broido, D. A., Carbon nanotube ballistic thermal conductance and its limits. *Physical Review Letters* **2005,** *95* (9), 096105.

169. Cao, J. X.; Yan, X. H.; Xiao, Y.; Tang, Y.; Ding, J. W., Exact study of lattice dynamics of single-walled carbon nanotubes. *Physical Review B* **2003,** *67* (4), 045413.

170. Kim, P.; Shi, L.; Majumdar, A.; McEuen, P. L., Thermal transport measurements of individual multiwalled nanotubes. *Physical Review Letters* **2001,** *87* (21), 215502.

171. Kelly, B. T., *Physics of graphite*. London ; Englewood, N.J. : Applied Science, c1981.: 1981.

172. Yi, W.; Lu, L.; Zhang, D. L.; Pan, Z. W.; Xie, S. S., Linear specific heat of carbon nanotubes. *Physical Review B* **1999,** *59* (14), R9015-R9018.

173. Hone, J.; Llaguno, M. C.; Nemes, N. M.; Johnson, A. T.; Fischer, J. E.; Walters, D. A.; Casavant, M. J.; Schmidt, J.; Smalley, R. E., Electrical and thermal transport properties of magnetically aligned single wall carbon nanotube films. *Applied Physics Letters* **2000,** *77* (5), 666-668.

174. Pop, E.; Mann, D.; Wang, Q.; Goodson, K. E.; Dai, H. J., Thermal conductance of an individual single-wall carbon nanotube above room temperature. *Nano Letters* **2006,** *6* (1), 96-100.

175. Zhong, H.; Lukes, J. R., Interfacial thermal resistance between carbon nanotubes: Molecular dynamics simulations and analytical thermal modeling. *Physical Review B* **2006,** *74* (12), 125403.

176. Gulotty, R.; Castellino, M.; Jagdale, P.; Tagliaferro, A.; Balandin, A. A., Effects of Functionalization on Thermal Properties of Single-Wall and Multi-Wall Carbon Nanotube-Polymer Nanocomposites. *ACS Nano* **2013,** *7* (6), 5114-5121.

177. Yu, A.; Itkis, M. E.; Bekyarova, E.; Haddon, R. C., Effect of single-walled carbon nanotube purity on the thermal conductivity of carbon nanotube-based composites. *Applied Physics Letters* **2006,** *89* (13), 133102.

178. Hong, W.-T.; Tai, N.-H., Investigations on the thermal conductivity of composites reinforced with carbon nanotubes. *Diamond and Related Materials* **2008,** *17* (7-10), 1577-1581.

179. Song, Y. S.; Youn, J. R., Influence of dispersion states of carbon nanotubes on physical properties of epoxy nanocomposites. *Carbon* **2005,** *43* (7), 1378-1385.

180. Stauffer, D.; Aharony, A., *Introduction to percolation theory*. London ; Washington, DC : Taylor & Francis, 1992. 2nd ed.: 1992.

181. Du, F. M.; Fischer, J. E.; Winey, K. I., Effect of nanotube alignment on percolation conductivity in carbon nanotube/polymer composites. *Physical Review B* **2005,** *72* (12), 121404.

182.   Straat, M.; Toll, S.; Boldizar, A.; Rigdahl, M.; Hagstrom, B., Melt Spinning of Conducting Polymeric Composites Containing Carbonaceous Fillers. *Journal of Applied Polymer Science* **2011,** *119* (6), 3264-3272.

183.   Potschke, P.; Brunig, H.; Janke, A.; Fischer, D.; Jehnichen, D., Orientation of multiwalled carbon nanotubes in composites with polycarbonate by melt spinning. *Polymer* **2005,** *46* (23), 10355-10363.

184.   Haggenmueller, R.; Gommans, H. H.; Rinzler, A. G.; Fischer, J. E.; Winey, K. I., Aligned single-wall carbon nanotubes in composites by melt processing methods. *Chemical Physics Letters* **2000,** *330* (3-4), 219-225.

185.   Chien, A.-T.; Gulgunje, P. V.; Chae, H. G.; Joshi, A. S.; Moon, J.; Feng, B.; Peterson, G. P.; Kumar, S., Functional polymer-polymer/carbon nanotube bi-component fibers. *Polymer* **2013,** *54* (22), 6210-6217.

186.   Newcomb, B. A.; Chae, H. G.; Gulgunje, P. V.; Gupta, K.; Liu, Y.; Tsentalovich, D. E.; Pasquali, M.; Kumar, S., Stress transfer in polyacrylonitrile/carbon nanotube composite fibers. *Polymer* **2014,** *55* (11), 2734-2743.

187.   Chae, H. G.; Newcomb, B. A.; Gulgunje, P. V.; Liu, Y. D.; Gupta, K. K.; Kamath, M. G.; Lyons, K. M.; Ghoshal, S.; Pramanik, C.; Giannuzzi, L. A.; Sahin, K.; Chasiotis, I.; Kumar, S., Towards High Strength and High Modulus Carbon Fibers. *Submitted*.

188.   Moon, J.; Weaver, K.; Feng, B.; Chae, H. G.; Kumar, S.; Baek, J.-B.; Peterson, G. P., Thermal conductivity measurement of individual poly(ether ketone)/carbon nanotube fibers using a steady-state dc thermal bridge method. *Review of Scientific Instruments* **2012,** *83* (1), 016103.

189.   Zhou, G. S.; Liu, Y. Q.; He, L. L.; Guo, Q. G.; Ye, H. Q., Microstructure difference between core and skin of T700 carbon fibers in heat-treated carbon/carbon composites. *Carbon* **2011,** *49* (9), 2883-2892.

190.   Liu, X. F.; Zhu, C. Z.; Guo, J.; Liu, Q. L.; Dong, H. X.; Gu, Y. Z.; Liu, R. G.; Zhao, N.; Zhang, Z. G.; Xu, J., Nanoscale dynamic mechanical imaging of the skin-core difference: From PAN precursors to carbon fibers. *Materials Letters* **2014,** *128*, 417-420.

191.   Torayca T300 Data Sheet. http://www.toraycfa.com/pdfs/T300DataSheet.pdf (accessed October 1, 2014).

192.   Torayca T1000G Data Sheet. http://www.toraycfa.com/pdfs/T1000GDataSheet.pdf (accessed December 1, 2014).

193.   Heremans, J.; Rahim, I.; Dresselhaus, M. S., Thermal conductivity and Raman spectra of carbon fibers. *Physical Review B* **1985,** *32* (10), 6742-6747.

194.   Lyons, K.; Newcomb, B.; McDonald, K.; Chae, H.; Kumar, S., Development of single filament testing procedure for polyacrylonitrile precursor and polyacrylonitrile-based carbon fibers. *Journal of Composite Materials* **2014**.

195.   Ho, C. Y.; Powell, R. W.; Liley, P. E., Thermal Conductivity of the Elements. *Journal of Physical and Chemical Reference Data* **1972,** *1* (2), 279-421.

196.   Bacon, G. E., A method for determining the degree of orientation of graphite. *Journal of Applied Chemistry* **1956,** *6* (11), 477-481.

197.   Fischbach, D. B., Preferred Orientation Parameters for Pyrolytic Carbons. *Journal of Applied Physics* **1966,** *37* (5), 2202-2203.

198.   Han, Z.; Fina, A., Thermal conductivity of carbon nanotubes and their polymer nanocomposites: A review. *Progress in Polymer Science* **2011,** *36* (7), 914-944.

199. Warner, S. B.; Peebles, L. H.; Uhlmann, D. R., Oxidative stabilization of acrylic fibers. Part 1. Oxygen uptake and general model. *Journal of Materials Science* **1979,** *14* (3), 556-564.

200. Moreton, R.; Watt, W., Tensile strengths of carbon fibers. *Nature* **1974,** *247* (5440), 360-361.

201. Sharp, J. V.; Burney, S. G. Proceedings of the International Conference on Carbon Fibers, Their Composites, and Applications, London, The Plastics Institute: London, 1971; p 10.

202. Reynolds, W. N.; Moreton, R., Some factors affecting the strengths of carbon fibers. *Philosophical Transactions of the Royal Society a-Mathematical Physical and Engineering Sciences* **1980,** *294* (1411), 451-461.

203. Sahin, K.; Fasanella, N. A.; Chasiotis, I.; Lyons, K. M.; Newcomb, B. A.; Kamath, M. G.; Chae, H. G.; Kumar, S., High strength micron size carbon fibers from polyacrylonitrile-carbon nanotube precursors. *Carbon* **2014,** *77* (0), 442-453.

204. Odian, G., *Principles of Polymerization*. 4 ed.; John Wiley & Sons, Inc.: Hoboken, New Jersey, 2004.

205. Oh, S. J.; Lee, H. J.; Keum, D. K.; Lee, S. W.; Wang, D. H.; Park, S. Y.; Tan, L. S.; Baek, J. B., Multiwalled carbon nanotubes and nanofibers grafted with polyetherketones in mild and viscous polymeric acid. *Polymer* **2006,** *47* (4), 1132-1140.

206. Choi, J. Y.; Oh, S. J.; Lee, H. J.; Wang, D. H.; Tan, L. S.; Baek, J. B., In-situ grafting of hyperbranched poly(ether ketone)s onto multiwalled carbon nanotubes via the A(3)+B-2 approach. *Macromolecules* **2007,** *40* (13), 4474-4480.

207. Jeon, I. Y.; Tan, L. S.; Baek, J. B., Nanocomposites derived from in situ grafting of linear and hyperbranched poly(ether-ketone)s containing flexible oxyethylene spacers onto the surface of multiwalled carbon nanotubes. *Journal of Polymer Science Part a-Polymer Chemistry* **2008,** *46* (11), 3471-3481.

208. Du, Y.; Hu, N. T.; Zhou, H. W.; Li, P.; Zhang, P.; Zhao, X. G.; Dang, G. D.; Chen, C. H., Dispersion of multi-walled carbon nanotubes in poly(aryl ether ketone) obtained by in situ polymerization. *Polymer International* **2009,** *58* (7), 832-837.

209. Diez-Pascual, A. M.; Martinez, G.; Gonzalez-Dominguez, J. M.; Anson, A.; Martinez, M. T.; Gomez, M. A., Grafting of a hydroxylated poly(ether ether ketone) to the surface of single-walled carbon nanotubes. *Journal of Materials Chemistry* **2010,** *20* (38), 8285-8296.

210. Diez-Pascual, A. M.; Martinez, G.; Martinez, M. T.; Gomez, M. A., Novel nanocomposites reinforced with hydroxylated poly(ether ether ketone)-grafted carbon nanotubes. *Journal of Materials Chemistry* **2010,** *20* (38), 8247-8256.

211. Jain, R.; Choi, Y. H.; Liu, Y.; Minus, M. L.; Chae, H. G.; Kumar, S.; Baek, J. B., Processing, structure and properties of poly(ether ketone) grafted few wall carbon nanotube composite fibers. *Polymer* **2010,** *51* (17), 3940-3947.

212. Baek, J. B.; Lyons, C. B.; Tan, L. S., Grafting of vapor-grown carbon nanofibers via in-situ polycondensation of 3-phenoxybenzoic acid in poly(phosphoric acid). *Macromolecules* **2004,** *37* (22), 8278-8285.

213. Diez-Pascual, A. M.; Naffakh, M.; Gomez, M. A.; Marco, C.; Ellis, G.; Martinez, M. T.; Anson, A.; Gonzalez-Dominguez, J. M.; Martinez-Rubi, Y.; Simard, B., Development and characterization of PEEK/carbon nanotube composites. *Carbon* **2009,** *47* (13), 3079-3090.

214. Diez-Pascual, A. M.; Ashrafi, B.; Naffakh, M.; Gonzalez-Dominguez, J. M.; Johnston, A.; Simard, B.; Martinez, M. T.; Gomez-Fatou, M. A., Influence of carbon nanotubes on the thermal, electrical and mechanical properties of poly(ether ether ketone)/glass fiber laminates. *Carbon* **2011,** *49* (8), 2817-2833.

215.   Ogasawara, T.; Tsuda, T.; Takeda, N., Stress-strain behavior of multi-walled carbon nanotube/PEEK composites. *Composites Science and Technology* **2011,** *71* (2), 73-78.

216.   Song, H. J.; Li, N.; Yang, J.; Min, C. Y.; Zhang, Z. Z., Preparation and tribological behaviors of poly (ether ether ketone) nanocomposite films containing graphene oxide nanosheets. *Journal of Nanoparticle Research* **2013,** *15* (2).

217.   Diez-Pascual, A. M.; Xu, C. P.; Luque, R., Development and characterization of novel poly(ether ether ketone)/ZnO bionanocomposites. *Journal of Materials Chemistry B* **2014,** *2* (20), 3065-3078.

218.   Diez-Pascual, A. M.; Diez-Vicente, A. L., Development of Nanocomposites Reinforced with Carboxylated Poly(ether ether ketone) Grafted to Zinc Oxide with Superior Antibacterial Properties. *Acs Applied Materials & Interfaces* **2014,** *6* (5), 3729-3741.

219.   Balaji, V.; Tiwari, A. N.; Goyal, R. K., Fabrication and Properties of High Performance PEEK/Si3N4 Nanocomposites. *Journal of Applied Polymer Science* **2011,** *119* (1), 311-318.

220.   Wang, L.; Weng, L. Q.; Wang, L. L.; Song, S. H., Hydrothermal synthesis of hydroxyapatite nanoparticles with various counterions as templates. *Journal of the Ceramic Society of Japan* **2010,** *118* (1384), 1195-1198.

221.   Wang, L.; Weng, L. Q.; Song, S. H.; Zhang, Z. Y.; Tian, S. L.; Ma, R., Characterization of polyetheretherketone-hydroxyapatite nanocomposite materials. *Materials Science and Engineering a-Structural Materials Properties Microstructure and Processing* **2011,** *528* (10-11), 3689-3696.

222.   Kuo, M. C.; Huang, J. C.; Chen, M., Non-isothermal crystallization kinetic behavior of alumina nanoparticle filled poly(ether ether ketone). *Materials Chemistry and Physics* **2006,** *99* (2-3), 258-268.

223.   Kuo, M. C.; Tsai, C. M.; Huang, J. C.; Chen, M., PEEK composites reinforced by nano-sized SiO2 and Al2O3 particulates. *Materials Chemistry and Physics* **2005,** *90* (1), 185-195.

224.   Goyal, R. K.; Tiwari, A. N.; Mulik, U. P.; Negi, Y. S., Novel high performance Al2O3/poly(ether ether ketone) nanocomposites for electronics applications. *Composites Science and Technology* **2007,** *67* (9), 1802-1812.

225.   Goyal, R. K.; Tiwari, A. N.; Mulik, U. P.; Negi, Y. S., Study on Microhardness, Dynamic Mechanical, and Tribological Properties of PEEK/Al2O3 Composites. *Journal of Applied Polymer Science* **2008,** *110* (6), 3379-3387.

226.   Lai, Y. H.; Kuo, M. C.; Huang, J. C.; Chen, M., On the PEEK composites reinforced by surface-modified nano-silica. *Materials Science and Engineering a-Structural Materials Properties Microstructure and Processing* **2007,** *458* (1-2), 158-169.

227.   Girifalco, L. A.; Hodak, M.; Lee, R. S., Carbon nanotubes, buckyballs, ropes, and a universal graphitic potential. *Physical Review B* **2000,** *62* (19), 13104-13110.

228.   Arrighi, V.; McEwen, I. J.; Qian, H.; Prieto, M. B. S., The glass transition and interfacial layer in styrene-butadiene rubber containing silica nanofiller. *Polymer* **2003,** *44* (20), 6259-6266.

229.   Ash, B. J.; Siegel, R. W.; Schadler, L. S., Glass-transition temperature behavior of alumina/PMMA nanocomposites. *Journal of Polymer Science Part B-Polymer Physics* **2004,** *42* (23), 4371-4383.

230.   Zeng, J. J.; Saltysiak, B.; Johnson, W. S.; Schiraldi, D. A.; Kumar, S., Processing and properties of poly(methyl methacrylate)/carbon nanofiber composites. *Composites Part B-Engineering* **2004,** *35* (3), 245-249.

231.   Zhang, X. F.; Liu, T.; Sreekumar, T. V.; Kumar, S.; Hu, X. D.; Smith, K., Gel spinning of PVA/SWNT composite fiber. *Polymer* **2004,** *45* (26), 8801-8807.

232. Overney, R. M.; Buenviaje, C.; Luginbuhl, R.; Dinelli, F., Glass and structural transitions measured at polymer surfaces on the nanoscale. *Journal of Thermal Analysis and Calorimetry* **2000,** *59* (1-2), 205-225.

233. Wilchinsky, Z. W., Measurement of orientation in polypropylene film. *Journal of Applied Physics* **1960,** *31* (11), 1969-1972.

234. Tsagaropoulos, G.; Eisenberg, A., Direct observation of two glass transitions in silica-filled polymers-implications for the morphology of random ionomers. *Macromolecules* **1995,** *28* (1), 396-398.

235. Fragiadakis, D.; Pissis, P.; Bokobza, L., Glass transition and molecular dynamics in poly (dimethylsiloxane)/silica nanocomposites. *Polymer* **2005,** *46* (16), 6001-6008.

236. Chen, L.; Zheng, K.; Tian, X. Y.; Hu, K.; Wang, R. X.; Liu, C.; Li, Y.; Cui, P., Double Glass Transitions and Interfacial Immobilized Layer in in-Situ-Synthesized Poly(vinyl alcohol)/Silica Nanocomposites. *Macromolecules* **2010,** *43* (2), 1076-1082.

237. Robertson, C. G.; Rackaitis, M., Further Consideration of Viscoelastic Two Glass Transition Behavior of Nanoparticle-Filled Polymers. *Macromolecules* **2011,** *44* (5), 1177-1181.

238. Rodrigue.F; Thrower, P. A.; Walker, P. L., Kinetic studies of oxidation of highly oriented pyrolytic graphites. *Carbon* **1974,** *12* (1), 63-70.

239. Piquero, T.; Vincent, H.; Vincent, C.; Bouix, J., Influence of carbide coatings on the oxidation behavior of carbon-fibers. *Carbon* **1995,** *33* (4), 455-467.

240. Dresselhaus, M. S.; Dresselhaus, G.; Sugihara, K.; Spain, I. L.; Goldberg, H. A., *Graphite fibers and filaments*. Berlin ; New York : Springer-Verlag, c1988.: 1988.

241. McKee, D. W.; Mimeault, V. J., *Chemistry and Physics of Carbon*. Marcel Dekker, Inc.: New York, 1975; Vol. 8.

242. Smith, G. W., Oxidation resistance of pyrolytically grown carbon fibers. *Carbon* **1984,** *22* (6), 477-479.

243. Goldstein, E. M.; Carter, E. W.; Kluz, S., The improvement of oxidation resistance of graphite by composite technique. *Carbon* **1966,** *4* (2), 273-&.

244. Fitzer, E.; Kehr, D., Carbon, carbide and silicide coatings. *Thin Solid Films* **1976,** *39* (DEC), 55-67.

245. Woodley, R. E., Oxidation of boronated graphite. *Carbon* **1968,** *6* (5), 617-&.

246. Allardic.Dj; Walker, P. L., Effect of substitutional boron on kinetics of carbon-oxygen reaction. *Carbon* **1970,** *8* (3), 375-&.

247. Ismail, I. M. K., On the reactivity, structure, and porosity of carbon fibers and fabrics. *Carbon* **1991,** *29* (6), 777-792.